Excited State Dynamics of Metalloporphyrins Utilized in Organic Photovoltaic Devices

A DISSERTATION

SUBMITTED TO THE FACULTY OF THE GRADUATE SCHOOL

OF THE UNIVERSITY OF MINNESOTA

BY

Jonathan Arthur Hinke

IN PARTIAL FULFILLMENT OF THE REQUIREMENTS

FOR THE DEGREE OF

Doctor of Philosophy

David A. Blank

August, 2013

Acknowledgements

The time I have spent here at the University of Minnesota has been an enjoyable yet testing and worthwhile learning experience, the result of which is the presented thesis. This work is a collaborative work involving myself and several others. First, I would like to thank my advisor David Blank. His plethora of ideas and openness to discussions assisted in my learning experience day in and day out. The constant communication was always motivating and led to great results. I would not be where I am today without his assistance.

I would also like to thank members of the Holmes research group. Matt S. Menke and Wade Luhman prepared flawless films used for our spectroscopy which was instrumental in collecting clean data. Wade Luhman and Professor Russell Holmes assisted greatly in discussions on the experiments involving PtOEP, specifically the triplet fusion observed in neat films of PtOEP. Their resources and time spent through discussions on exciton dynamics were extremely beneficial to our project.

The past and current members of the Blank group have played a large role in my

research progress. Adam Huss and Matt Ammend took me under their wing as a first year student and taught me much of what I know about spectroscopy. We have also had many great postdoctoral researchers that assisted me and my projects, including Mayrose Salvidor, Andy Healy, Benj Fitzpatrick, and Toni Sanchez-Diaz. I would also like to thank other Blank group members, Tom Pundsack, Emily Pelton, Eric Nordland, and Philip Goff for their contributions and useful discussions. Everybody's time and effort is truly appreciated.

Finally, I would like to thank all my friends and family for their constant support throughout these past few years. You have always been there to give my mind an occasional breather yet keeping me focused on what is important. I would also like to thank my fiancée Erica. You have always been by my side and my best friend for the past five years. I love you very much.

Dedication

To my parents, James and Margaret, my sister Elizabeth, my brother Brandon, and my fiancée Erica.

Abstract

Energy consumption in the world is currently dominated by fossil fuels (85%) which include coal, gas, and oil while photovoltaics constitute a small portion ($< 0.1\%$). The photovoltaic market is primarily comprised of silicon based photovoltaics which are currently unable to compete with fossil fuels in cost per kilowatt hour. However, emerging organic photovoltaics (OPVs) have shown potential to be surpass silicon based photovoltaics and be cost competitive with fossil fuels. One of the limitations in OPVs is the short diffusion length (10 nm) relative to the absorbing layer thickness (100-200 nm).

Porphyrins, of which chlorophylls are derivatives, remain at the forefront of OPV investigation due to their success in natural photosynthesis and potential in photovoltaic devices. Furthermore, platinum octaethyl porphyrin (PtOEP) has been estimated to have a diffusion length between 18-30 nm and long triplet lifetime ($\approx$100 μs). This long diffusion length indicates that platinum porphyrins are able to efficiently funnel excitons to the interface, showing promise as suitable donor materials. Other porphyrins, such as nickel, palladium, tin, and indium show similar properties including strong absorption, enhanced excited state lifetimes, and charge separated states.

This thesis investigates the excited state properties of porphyrin materials. Ultrafast pump probe spectroscopy allows for investigation of excited state dynamics including intramolecular energy transfer observed in nickel porphyrins. Femtosecond dynamics of

palladium and platinum porphyrins are explored as well as triplet fusion in PtOEP neat films, providing a unique way to study energy transfer and amorphous films. Finally, pump probe studies aim to explain photoluminescent quenching behavior in tin and indium porphyrins through observation of charge separated states. Investigation of these porphyrins is crucial to improving device efficiency through fundamental understanding of the excited state dynamics in films and neat films.

Contents

List of Tables

List of Figures

Chapter 1

Introduction

1.1 Motivation

The worldwide demand for energy continues to grow. The 2011 energy use was 16.8 TW and is expected to rise to 25.6 TW, a 50% increase, in 2035.[6] The cost of oil is expected to double in that span, meanwhile concerns about how greenhouse gases impact global temperature and weather patterns yearn for a clean, renewable energy source.[7;8;9;10;11] The sun supplies approximately 120,000 TW to the earth per year and only a small fraction needs to be harnessed to supply the worlds demands.[7] It is estimated that approximately 100 TW of energy are harnessed through the photosynthetic process in plants[12] and replicating that process would be enough for current and future energy demand. If an area the size of Kansas was covered in 10% efficient photovoltaics, that would be enough to supply the U.S. energy requirements. In order to complete this

task, photovoltaics need to be efficient and able to be produced on a large scale while maintaining cost effectiveness.

Research into photovoltaics dates back to Alexandre-Edmond Becquerel's work on illuminating AgCl electrodes in 1839[13]. The first modern solar cells, however, were introduced in 1946 with the discovery of the p-n junction[14] and were further improved upon in 1954 by utilizing a silicon based p-n junction to increase efficiencies to over 5%[15]. Single crystal silicon cells continued to increase to 13% in 1977 at Mobil Solar to 25% in 1995 at the University of New South Wales.[2;16] Reserach in the early 1990's resulted in device component and architecture changes to increase total efficiency. Efficiencies of single junction gallium arsenide (GaAs) have reached 25.8% while multijunction cells have achieved the maximum photovoltaic efficiency to date with 43.5%.[2] Silicon based solar cells have recently dominated the market due to their moderate efficiencies and manufacturing costs.[15] Currently, production is in process for highly efficient and cost effective copper, gallium, indium, and selenide inorganic based photovoltaics. However significant increases in costs for gallium as well as a limited supply limit the ability for mass-production commercial applications to compete with energy demand.[8;17;18]

Thin film technologies involving cadmium telluride (CdTe) and copper indium gallium diselenide (CIGS) have achieved over 10% efficiencies in current cells as represented in Figure 1.1.[2] Several concerns still remain about the long term feasability of these devices. First, indium is becoming more scarce due to current applications in televisions which will drive the long term prices of these devices higher.[19] Secondly, the toxicity of

cadmium is a concern. Because of these issues, safe, efficient, and cost effective devices based on abundant resources represent optimum properties for future photovoltaics.

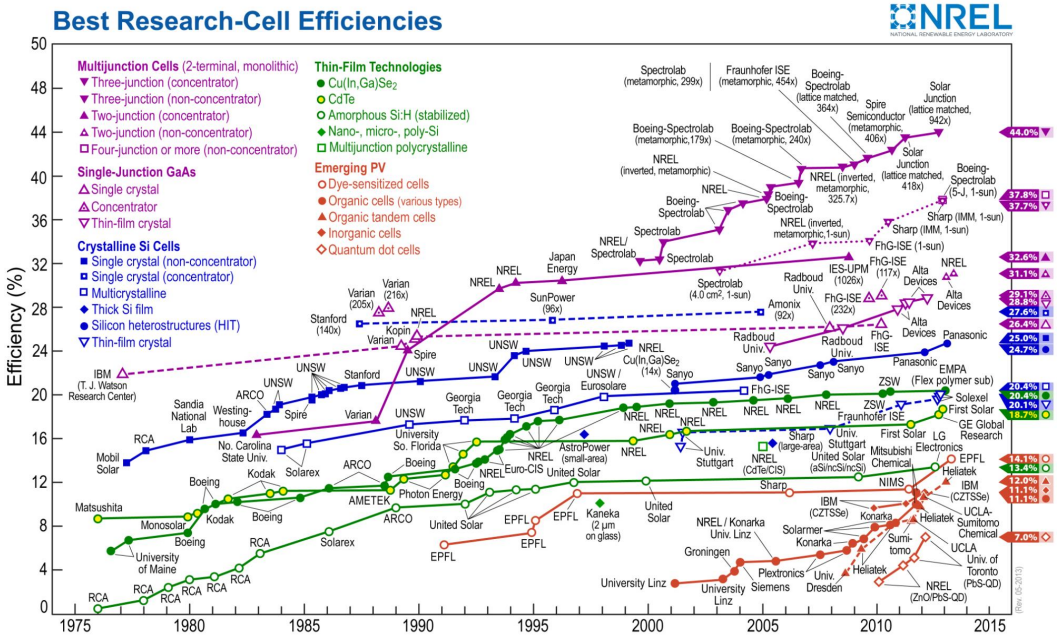

Figure 1.1: Current progress of first, second, and third generation photovoltaics as of 2013. Figure reprocued from reference[2].

1.1.1 Organic Photovoltaic Progress

Organic photovoltaics (OPV) show promise as low cost alternatives to current solar cells due to abundant materials and efficient fabrication techniques.[20] Development of the

first organic photovoltaics originated in 1975 with a 0.001% efficiency using a metal-chlorophyll-a layered device.[21] Organic photovoltaic efficiency was later improved in 1985 using a copper phthalocyanine (CuPc) layer and a perylene tetracarboxylic derivative sandwiched between a transparent indium tin oxide (ITO) and opaque silver electrode, resulting in a 1% power conversion efficiency under illumination.[22] Utilization of new devices structures and new materials, including a double heterostructure CuPc/C_{60} device, improved efficiencies to 3.6%.[23]

Current efficiencies, however, are just reaching the 10% threshold.[2] One of the advantages of OPV's is the ease of production and potential lower chemical cost. By increasing efficiencies of these photovoltaics, the ability to create affordable, clean, low cost cells may be available.

1.1.2 Thesis Overview

The main focus of this thesis work is focused on understanding the excited state dynamics of materials used in current OPVs. Exciton diffusion plays a crucial role in the photoconversion process in OPV's and remains a limiting factor to achieving higher efficiencies. Time resolved dynamics of exciton behavior in solutions and thin films is important in improving exciton diffusion lengths and increasing OPV efficiencies. Current investigative techniques to monitor exciton dynamics are limited to time-integrated results or time dependent behavior of only photoluminescent excited states. Ultrafast

pump-probe spectroscopy is not limited to photoluminescent materials and can monitor the time-dependent dynamics of excited states. The first step will focus on the intramolecular dynamics of these photovoltaic materials including intersystem crossing andd intramolecular electron and energy transfer. Secondly, this work investigates the intermolecular excitonic interactions that limit current devices and allows unique insight into the energy transfer mechanisms in OPVs.

1.2 Physics and Operation of Photovoltaic Devices

1.2.1 Introduction

This chapter introduces the progress in inorganic and organic photovoltaic efficiencies and a few hurdles that must be overcome to supply the future energy demand. It focuses on the fundamentals of photovoltaic design and the physics of device operation with a description of converting solar energy to electrical energy in photovoltaics. It begins with discussion on conversion of sunlight to molecular energy through absorption of photons into bound excited states or free charge carriers. Second, the physics of excited state transport, including energy transfer mechanisms, are presented. Finally, there will be discussion on specific areas to improve photovoltaic efficiency and direct the focus of this thesis work.

1.2.2 Excited State Processes

Efficiency of a photovoltaic device is dependent on the fundamental excited state processes which are responsible for harnessing and transferring energy. The first step in the photovoltaic process is conversion of solar energy into electronic energy through molecular absorption of a photon. Let us consider a light of wavelength λ and frequency ν. We can describe the energy of a photon with energy E_{ph}, as shown in Equation 1.1,

where h is Planck's constant (6.626 x 10^{-34} J $\cdot$ s)

$$E_{ph} = h\nu = \frac{hc}{\lambda} \tag{1.1}$$

Absorption is dependent on the photons' energy and the energetic gap between the ground and excited states of the molecule as well as any selection rules between those two states. If the energy of the photon equals the difference in energy of the two energy states, it may cause an electronic transition and create an excited state as shown in Figure 1.2. The ground and excited singlet states are denoted S_0 and S_1 while the triplet excited state is T_1. For singlets, electrons in the ground and excited states have opposing spins with a multiplicity of one while triplets have the same spin with the ground state and a multiplicity of three. Transitions in which the spin multiplicity does not change (Singlet $\rightarrow$ Singlet, Triplet $\rightarrow$ Triplet) are more favorable than those that require a spin flip (Singlet $\rightarrow$ Triplet, Triplet $\rightarrow$ Singlet). Excited state processes that retain spin state will have a higher rate of transfer and thus shorter lifetime than those that change spin multiplicities.

Applying the Born-Oppenheimer approximation, the nuclear degrees of freedom are considered to be in a fixed position relative to electronic excitation. Thus, the excitation process is considered to be instantaneous relative to the nuclear motions of the molecule as depicted through vertical lines in Figure 1.2.[24] The probability of transition then depends on the overlap of the wavefunction of the two states. Since the vibrational levels have different wavefunctions, the probability of transition will not be equal between the

states and accounts for the absorption spectra in Figure 1.3.

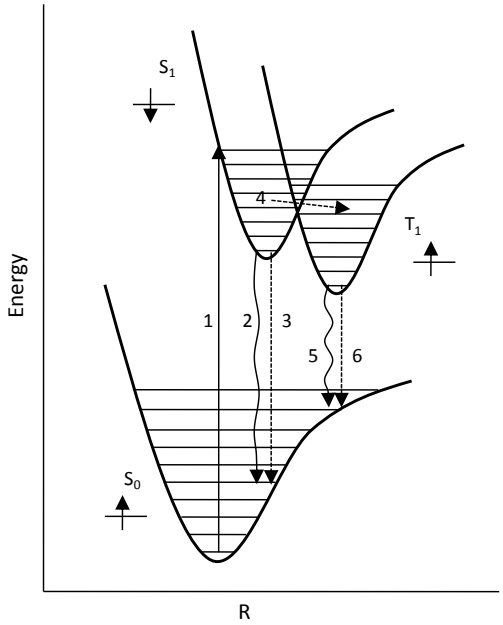

Figure 1.2: Illustration of the excited electronic and vibrational states of a molecule. After absorption from S_0 to S_1 (1), the energy vibrationally relaxes in the excited state and may deactivate through nonradiative internal conversion (2) or radiative $S_1 \rightarrow S_0$ fluorescence (3). Electron spins are also presented near the corresponding energy state.[1]

Decay of S_1 is possible through several processes as presented in Figure 1.2. Promotion to S_1 results in rapid thermalization of the excess vibrational energy, termed vibrational relaxation. After thermalization, electrons are considered to be populating the lowest vibrational state of that excited state. The electron may relax to a lower

excited state through internal conversion (3) which retains the spin multiplicity. Internal conversion may also occur when excited to a higher excited state, S_2, where it can non-radiatively relax down to S_1 ($S_2 \rightarrow S_1$) or the ground state ($S_2 \rightarrow S_0$).

The electron may relax to the ground state through a $S_1 \rightarrow S_0$ radiative transition called fluorescence (2). Kasha's rule states that fluorescence occurs only from the lowest excited state down to the ground state.[25] The electron may relax from the excited state to higher vibrational states of the ground state as shown in Figure 1.3. Energy spacing between the vibrational states gives the vibronic structure in the absorption and emission spectra in Figure 1.3.

The electron may also reach a lower excited state through intersystem crossing (4). Intersystem crossing is a non-radiative process that requires a flip of the electronic spin state and is a slower process when compared to internal conversion and fluorescence. The rate of intersystem crossing is enhanced by overlap of the vibrational levels of the singlet and triplet states. Intersystem crossing can also be increased through the presence of heavy atoms which enhances the spin-orbit coupling between the spin and orbital angular momentum of the electron.[26]

After population of the triplet state, the electron can undergo similar processes when compared to the singlet state. Vibrational relaxation to the lowest vibrational level in the triplet excited state occurs very rapidly. While back-intersystem crossing from $T_1 \rightarrow S_1$ is possible in some systems, radiative and non-radiative transitions from $T_1 \rightarrow S_0$ are primarily responsible for deactivation of T_1 repopulation of the ground

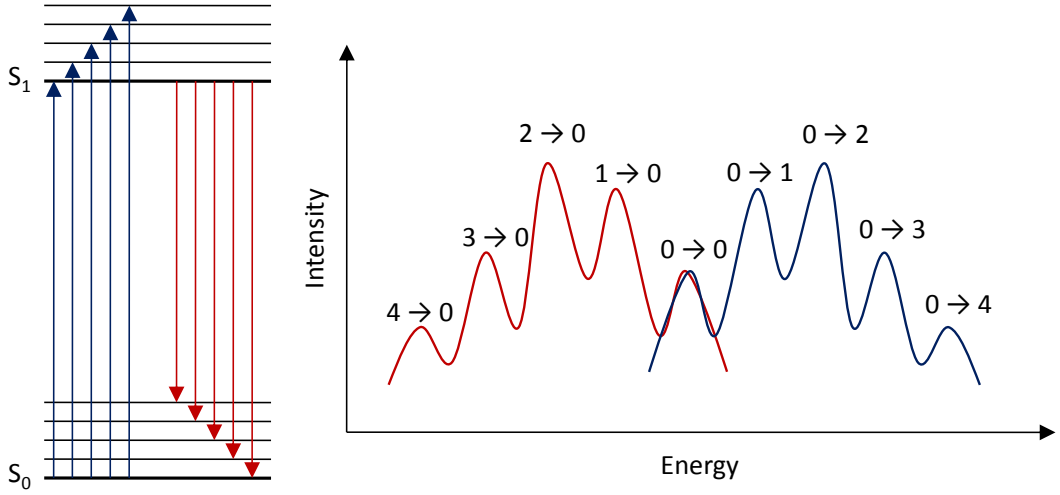

Figure 1.3: Absorption (blue) and emission (red) bands of a molecule following the Franck-Condon progression. Energy between the absorption and emission bands corresponds to spacing between the vibrational levels. [1]

state. Non-radiative decay through $T_1 \rightarrow S_0$ intersystem crossing is a slower process as it necessitates a change of the electron spin. Phosphorescence, a radiative $T_1 \rightarrow S_0$ transition, also requires a spin flip, which is a slower process as shown in Table 1.2.2.

Process	Transition	Time scale (s)
Fluorescence	$S_1 \rightarrow S_0$	10^{-9}
Internal Conversion	$S_1 \rightarrow S_0$	10^{-7} - 10^{-12}
Intersystem Crossing	$S_1 \rightarrow T_1$	10^{-6} - 10^{-12}
Phosphorescence	$T_1 \rightarrow S_0$	10^{-7} - 10^{-5}
Intersystem Crossing	$T_1 \rightarrow S_0$	10^{-8} - 10^{-3}

Table 1.1: Excited state processes and their respective transitions and time scales.[1]

1.2.3 The Porphyrin Four Orbital Model

Absorption bands of porphyrins and metalloporphyrins in the visible and ultraviolet (UV) region has been thoroughly documented in the literature. Most notable are the Q,B,N,L, and M bands which correspond to absorption from the singlet ground state, S_0, to singlet excited states S_1, S_2, S_3, S_4, and S_5. The Q and B bands remain the most studied of the (π,π*) transitions and were first observed in 1944.[27] These bands showed large differences in the absorption spectra when comparing the free-base porphyrins (H_2P) and metalloporphyrins. An example of the metalloporphyrin absorption spectrum, using zinc octaethyl porphyrin (ZnOEP), is shown in Figure 1.4.

Transition to the modern view of the description and prediction of porphyrin absorption spectra with a physical model arguably began with molecular orbital calculations on porphine and tetrahydroporphine.[28] Their method used a linear combination of atomic orbitals (LCAO) to accurately describe the wavelength of the absorption bands but it

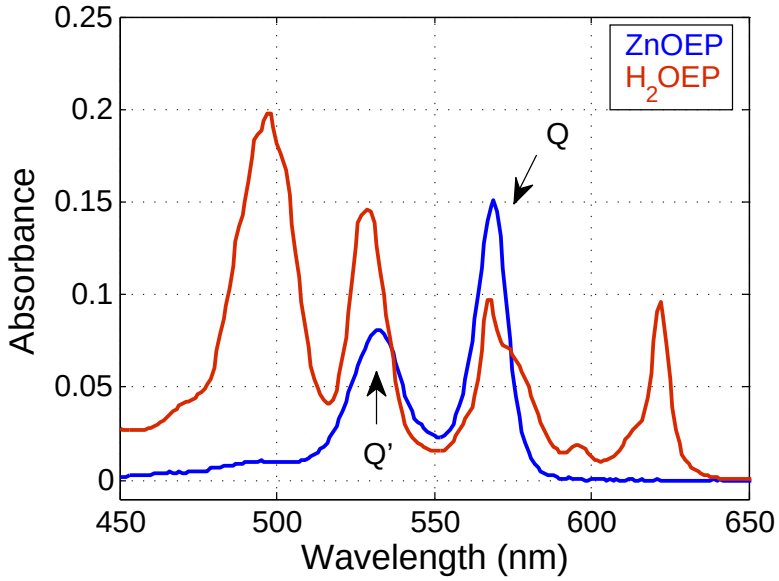

Figure 1.4: Absorption spectra of zinc octaethyl porphyrin (ZnOEP) and free base porphyrin (H_2OEP) illustrating the splitting of the Q bands due to non-degeneracy of the D_{16h} symmetry in H_2OEP.

was unable to predict the intensities of those absorptions. The root of the problem was an incorrect assignment of the absorption bands to different distinct transitions. Application of a free electron model resolved the absorption band intensities without perturbing the energy gap and thus the expected transition wavelengths.[29;30]

The most widely accepted model for porphyrin absorption was developed by Martin Gouterman in 1963.[31] The four orbital model incorporates four HOMO and LUMO functions from the LCAO calculations and allows for varational wave functions through a configuration interaction (CI) with an extended Hückel treatment. He considered the case of metalloporphyrins which have a point group D_{4h}. The representations for the HOMOs are singly degenerate $|a_{1u}>$ and $|a_{2u}>$ while the LUMOs are doubly degenerate $|e_{g,x}>$ and $|e_{g,y}>$. Initially, the Q and B bands were assigned as independent transitions $|a_{1u}> \rightarrow |e_g>$, and $|a_{2u}> \rightarrow |e_g>$. However, the computational results predict that since the transition dipoles are similar the oscillator strengths would be equal, which is contrary to experimental results. Transitions from $|a_{1u}> \rightarrow |e_g>$ and $|a_{1u}> \rightarrow |e_g>$ both give rise to singlet ^1E_u states and a configuration interaction leads to a linear combination of B and Q transitions in Figure 1.5.[32] Because both transitions ($|a_{1u}> \rightarrow |e_g>$, $|a_{2u}> \rightarrow |e_g>$) have the same symmetry, their wave function overlap results in a mixing of states.[3]

$$|B_x^0> = \frac{1}{\sqrt{2}}[(a_{2u}> \rightarrow e_{g,x}>) - (a_{1u}> \rightarrow e_{g,y}>)]$$

$$|B_y^0> = \frac{1}{\sqrt{2}}[(a_{2u}> \rightarrow e_{g,y}>) + (a_{1u}> \rightarrow e_{g,x}>)]$$

$$|Q_x^0> = \frac{1}{\sqrt{2}}[(a_{2u}> \rightarrow e_{g,x}>) + (a_{1u}> \rightarrow e_{g,y}>)]$$

$$|Q_y^0> = \frac{1}{\sqrt{2}}[(a_{2u}> \rightarrow e_{g,y}>) - (a_{1u}> \rightarrow e_{g,x}>)]$$

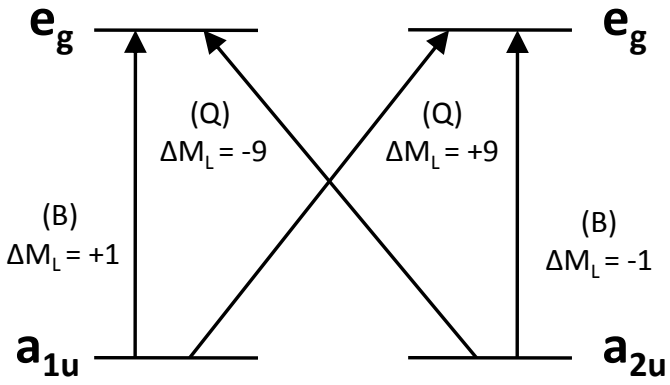

Figure 1.5: Diagram representing the molecular orbital transitions in porphyrin systems that form the B and Q bands. M_L represents the change in angular momentum for the described transition.[3]

Removal of the central metal atom into the free base porphyrin (H_2P) removes the x and y degeneracy and changes the point group assignment from D_{4h} to D_{16h}. The $|e_g>$ atomic orbitals also lose degeneracy and ground state absorption to the $|e_g>$ states leads to two separate singlet states ($^1E_{1u}$, $^1E_{7u}$) instead of degenerate ^1E_u states. This perturbation causes a splitting of the Q and B bands in the absorption spectra and can

now be described as:

$$
\begin{aligned}
|B_x^0> &= \frac{1}{\sqrt{2}}[(a_{2u}> \rightarrow e_{g,x}>) - (a_{1u}> \rightarrow e_{g,y}>)] \\
|B_y^0> &= cos(\eta(|a_{2u}> \rightarrow |e_{g,y}>)) + sin(\eta(|a_{1u}> \rightarrow |e_{g,x}>)) \\
|Q_x^0> &= \frac{1}{\sqrt{2}}[(a_{2u}> \rightarrow e_{g,x}>) + (a_{1u}> \rightarrow e_{g,y}>)] \\
|Q_y^0> &= sin\eta(|a_{2u}> \rightarrow |e_{g,y}>) - cos\eta(|a_{1u}> \rightarrow |e_{g,x}>)
\end{aligned}
$$

The four orbital model extends beyond porphyrins and is applicable for similar structures such as phthalocyanines, corroles, chlorophylls, and hemes.[33] Many studies have rigorously expanded on the four orbital model using iterative extended Hückel (IEH) theory to explain larger porphyrin systems including irregular metalloporphyrins.[34;35;36] While radiationless decay has proved to be difficult to explain with the four orbital model, it has had much success with the electronic structure of porphyrins.[33]

1.2.4 Energy Transfer Mechanisms

Förster Energy Transfer

Förster resonance energy transfer (FRET) is an energy transfer process in which the energy of one excited molecule is transferred to another.[37;38;39] Similar to energy transfer through reabsorption in which a photon is emitted by the donor and absorbed by the acceptor, the probability of transfer is dependent on the spectral overlap of the emission

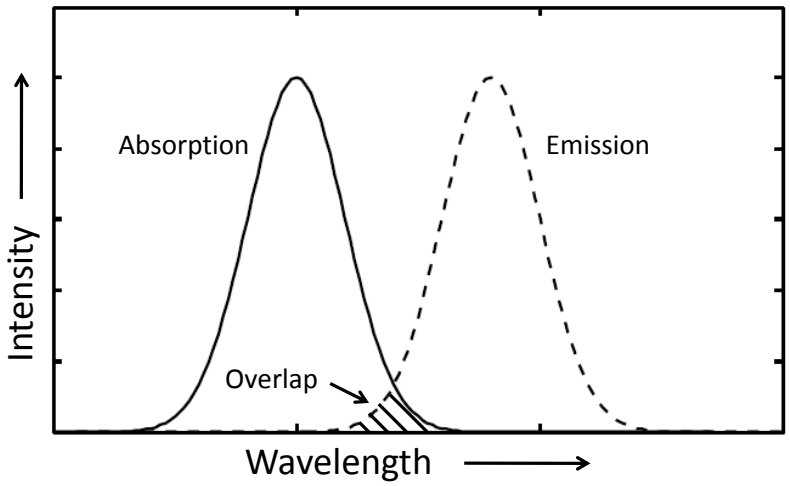

Figure 1.6: Absorption and emission of an arbitrary donor (solid) and acceptor (dash) molecule with the spectral overlap in the shaded region.

spectrum of the donor and absorption spectrum of the acceptor as illustrated in Figure 1.6 as well as the distance between chromophores. Unlike reabsorption, there is no emission and absorption of a photon. The excited donor molecule oscillation is resonant with the electronic energy gap of the acceptor as shown in Figure 1.7. The dipole-dipole coupling event induces the promotion of the electron on the acceptor molecule. Due to the resonance, there is no physical exchange of electrons as the excited electron in the donor relaxes to the ground state of the donor and the electron in the ground state of the acceptor is promoted to the excited state of the acceptor. The dipole coupling

process k_F can be described as shown in Equation 1.2

$$k_F = \frac{1}{\tau}\left(\frac{R_0}{r}\right)^6 \tag{1.2}$$

where τ is the excited state lifetime, r is the distance between molecules and R_0 is the Förster radius. The Förster radius is the distance at which the rate of energy transfer is equal to the rate of fluorescence. We can describe R_0 as shown in Equation 1.3.

$$R_0^6 = \frac{9000\,\phi_0\,ln(10)\,\kappa^2 J}{128\,\pi^6\,n^4\,N} \tag{1.3}$$

ϕ_0 is the fluorescence quantum yield of the donor molecule, n is the index of refraction, N is Avagadro's number and κ is the dipole orientation factor. $\kappa^2 = 2/3$ in isotropic distributions where dipoles are free to rotate for a statistical average. In constrained configurations such as solid films, it has been shown $\kappa = 0.845\sqrt{2/3}$ but depends on the morphology of the film.[40] κ can also been seen as a description of the density of states and Förster energy transfer is dependent on the resonance and coupling of the states. J, the spectral overlap integral, is shown in Equation 1.4.

$$J = \int \phi_D(\lambda)\phi_A(\lambda)\lambda^4 d\lambda \tag{1.4}$$

ϕ_D represents the normalized emission spectrum of the donor, ϕ_A is the normalized emisson spectrum, and λ is the wavelength. Förster transfer is typically thought to be a long distance transfer (1-10 nm) and is often considered to be the dominant transfer mechanism between chromophores with the same states.

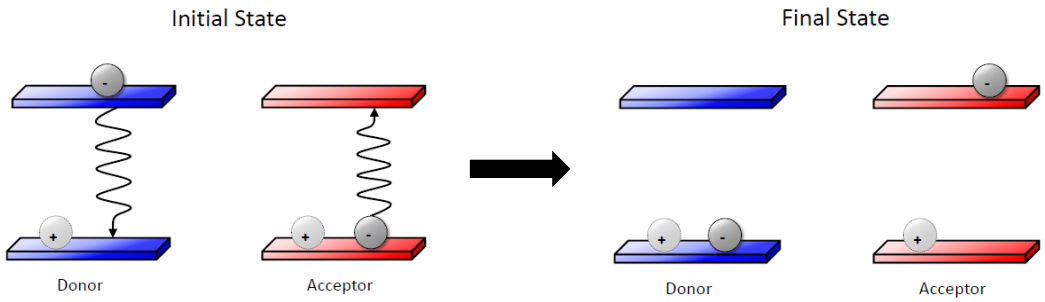

Figure 1.7: Diagram depicting the process of Förster energy transfer between a donor and acceptor molecule.

Dexter Energy Transfer

Another type of energy transfer is Dexter transfer. As opposed to Förster energy transfer, Dexter transfer involves the physical exchange of electrons between the donor and acceptor molecules in which electronic-dipole transitions between the two molecules are forbidden and is shown in Figure 1.8.[41] The electron on the donor excited state and the electron in the ground state of the acceptor undergo a simultaneous exchange of electrons. Due to the forbidden electronic-dipole transition, Dexter transfer requires overlap of the donor and acceptor wavefunctions. While typically considered to be the transfer mechanism for triplet materials, Dexter transfer is possible in the singlet state through spin conservation in Equation 1.5

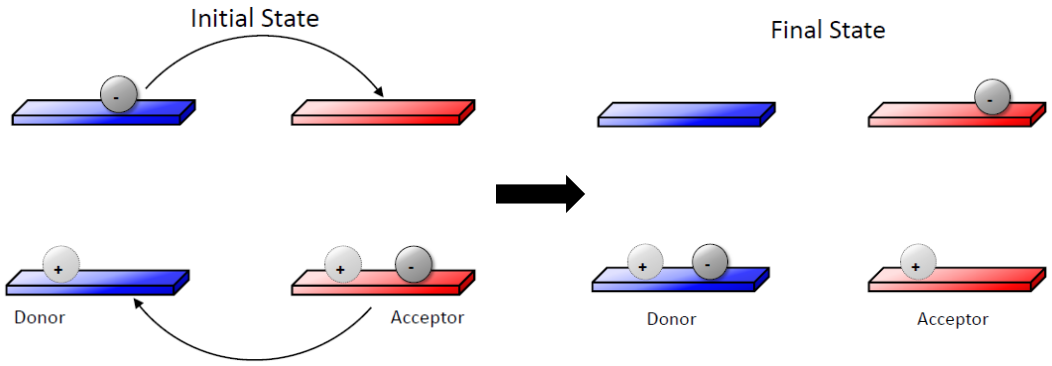

Figure 1.8: Dexter energy transfer process between a donor and acceptor molecule.

$$^1D* + ^1A \rightarrow ^1D + ^1A* \tag{1.5}$$

The rate of Dexter transfer, k_D, is described as:

$$k_D = \frac{2\pi}{\hbar} Z^2 \int F_D(E) F_A(E) dE \tag{1.6}$$

where Z^2 represents the exchange interaction between molecules and F_D and F_A are the normalized donor emission and acceptor absorption spectra, respectively. If we assume that the probability of energy transfer falls off exponentially at long distances, Equation 1.6 reduces to Equation 1.7.

$$k_D = \frac{2\pi}{\hbar} Z^2 J \exp -2r/L \tag{1.7}$$

$$k_D = K \exp -2r/L \tag{1.8}$$

where J is the overlap integral, r is the distance between donor and acceptor molecules, and L is the Dexter radius. Typically, the pre-exponential factors are combined to look like equation 1.8 which includes the wavefunction overlap of the donor and acceptor molecules. The physical exchange of electrons limits the distance in which Dexter transfer can occur to nearest neighbor interactions, typically on the order of 1-2 nm whereas Förster transfer is typically on the order of 1-10 nm.[38]

1.2.5 Photovoltaic Device Operation

Inorganic Solar Cells

Traditional inorganic solar cell operation relies on a creating a p-n junction within a single silicon crystal. The silicon is doped by adding atoms to create impurities in the semiconductor and form electron rich and electron poor regions of the crystal. The product of the doping is a p-n junction as shown in Figure 1.9. One portion of the silicon is typically doped with boron to form the hole rich p-type semiconductor material, whereas the other is doped with phosphorous to create the electron rich n-type material.

When light is incident on the photovoltaic, an electron is promoted from the valence band to the conduction band in the p-doped semiconductor (Figure 1.10). Photoexcitation of the electron leaves behind a net positive charge on the atom called a hole. The high dielectric constant of the material causes free carriers to be formed upon excitation

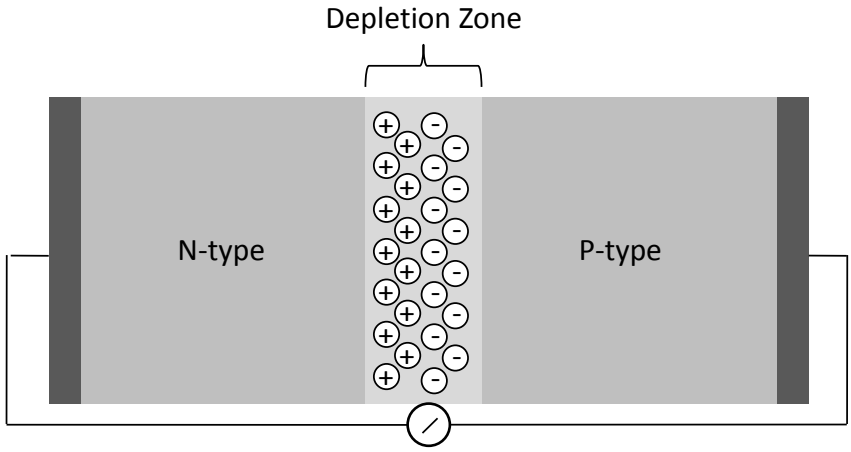

Figure 1.9: Schematic of a simple p-n junction silicon solar cell.

which are allowed to freely move around the material.[42] When a load is placed on the cell, the electrons will flow from the p-doped region of the cell to the n-doped region, be collected at the anode with its energy extracted in the external circuit.

The efficiency of the photovoltaic cell is based on several aspects. The limits of these processes has been defined by Shockley and Queisser, outlining the losses due to blackbody radiation, recombination and absorption losses and estimating a maximum efficiency of 33.7% in silicon photovoltaics.[43;44;45]

After photoexcitation in the p-doped region, the electron must transfer to the n-doped region.[46] Along the way, any slow moving holes in the p-doped region heading toward the cathode may recombine with the excited electron, leading to loss of the

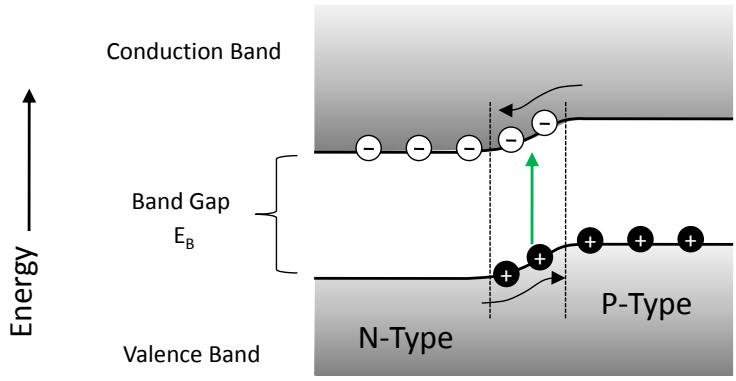

Figure 1.10: Valence and conduction band in a p-n junction solar cell.

energy. The recombination event is dependent on the concentration of electron and hole carriers in the semiconductor and thus puts a limit on the rate of charge carrier generation and subsequently the overall efficiency of the device.

Absorption of the solar spectrum plays a vital role in the efficiency of a photovoltaic cell and is shown in Figure 1.11. Maximizing the absorption of photons of all wavelengths is crucial to achieving optimal efficiency, however, silicon semiconductors are limited to a single band gap, typically around 1.1 eV. If we consider the case where a photon with energy E_{ph} ¡ E_B (Figure 1.10), the photon will not be absorbed by the semiconductor material and the energy associated with the photon will be lost. When E_{ph} ¿ E_B, the photon will be absorbed but will relax to the lowest vibrational state, losing excess

energy in the amount of the difference between the photon and bandgap ($\Delta E = E_{ph} - E_B$). If $E_{ph} = E_B$, the photon is absorbed with no loss in energy.

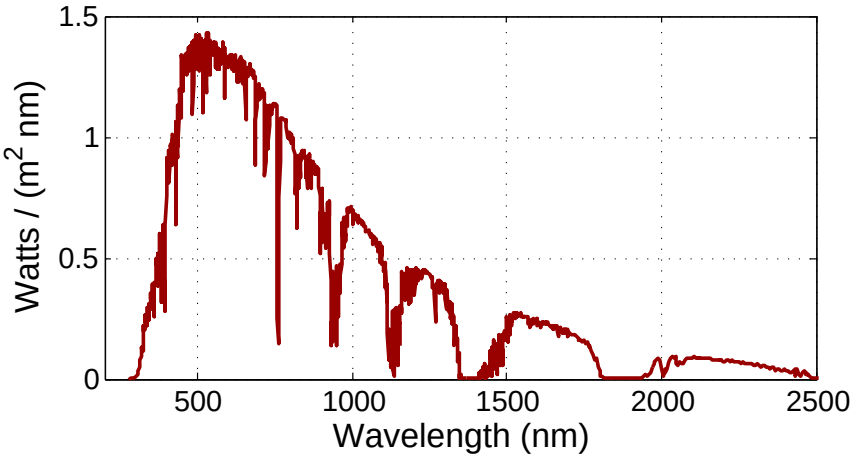

Figure 1.11: Solar irradiation spectrum taken at sea level, air mass = 1.5. Data taken from National Renewable Energy Laboratory (NREL).[4]

One approach to exceed the theoretical Shockley-Queisser limit is to use tandem or multijunction cells. These multijunction cells utilize difference materials with varying band gaps to minimize the loss of efficiency through relaxation or lack of absorption. It should be noted the Shockley-Queisser limit assumes a material with a single band gap and vibrational relaxation above the LUMO.[43]

Organic Solar Cells

Organic photovoltaics rely on many similar processes as inorganic photovoltaics in device operation including absorption and charge collection across an external circuit. However, the device morphology and fabrication techniques differ while the process of converting the absorbed energy into electrical energy is more complex.

The first step in an organic photovoltaic is absorption of a photon. As mentioned previously, photovoltaic power conversion efficiency will depend on overlap of the molecular band gap with the solar spectrum. In the case of organic photovoltaics, the band gap is determined by the difference in energy between the highest occupied molecular orbital (HOMO) and the lowest unoccupied molecular orbital (LUMO). One advantage of materials typically used in OPVs is a relatively thin absorptive layer, typically on the order of 100 nm - 200 nm[47;48] or at most 1 μm[49]. The thin layer allows for adequate absorption of the photon while minimizing the amount of materials used. The absorbed photon excites an electron from the one of the occupied molecular orbitals to an unoccupied molecular orbital (typically a HOMO $\rightarrow$ LUMO transition). Due to the low dielectric constant in organic materials,[42] the promoted electron is coulombically bound to its hole, creating an exciton as shown in Figure 1.12a. Since the electron-hole pair is bound, the electron and hole must be separated in order to generate free charge carriers.

To separate the bound electron from its hole, another molecule must be added to create charge separation through an energetic offset of the molecular orbitals. Figure

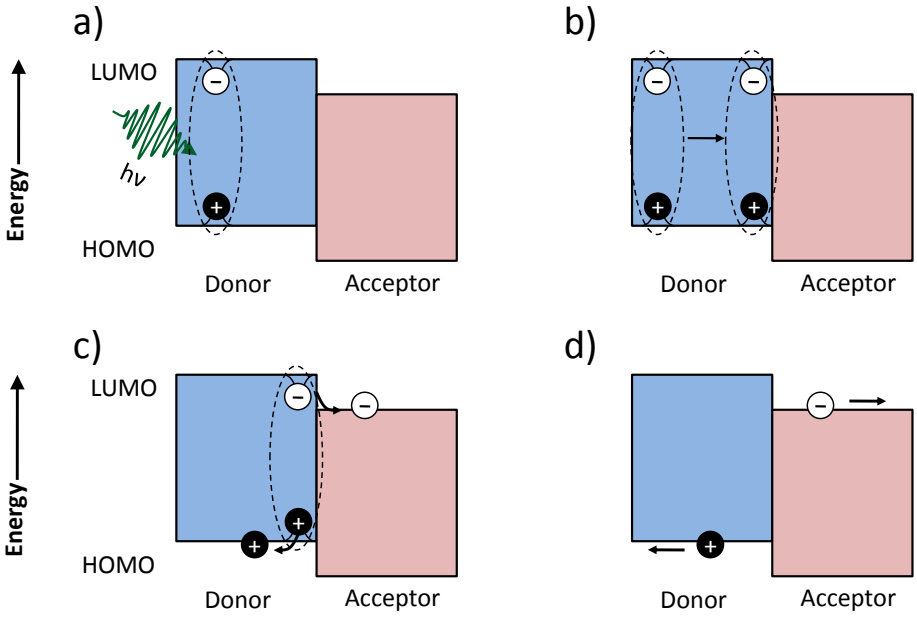

Figure 1.12: HOMO and LUMO of the donor (blue) and acceptor (red) in a bilayer organic photovoltaic. The vertical axis on the squares represents energy difference between the HOMO and LUMO while the x axis shows arbitrary distance from the donor-acceptor interface. Panel a) shows absorption of a photon, b) is the diffusion of the exciton in the donor mateial, c) depicts the charge separation of the exciton at the donor-acceptor interface, and d) shows the drift and diffusion of the electron and hole to the respective electrodes.

1.12 shows a simple donor-acceptor bilayer and the interface where charge separation occurs. Note that the molecule with the lower energy LUMO is considered to be the electron acceptor. In order to get to the interface, the exciton must diffuse or transfer the energy from one molecule to another. One of the limitations of the photovoltaic process rests with the fact that the exciton diffusion length, L_D, is typically short ($\sim$ 10 nm)[47;50;48] compared to the absorption layer thickness ($\sim$ 200 nm). Excitons created outside of L_D relative to the interface will, on average, not reach the interface and lose its energy through recombination.

Adjustments to the device architecture have sought to increase the interfacial contact between the donor and acceptor layer while reducing the distance the exciton must travel to reach an interface.

When an exciton reaches an interface, as shown in Figure 1.12c, charge separation can occur if the acceptor LUMO is lower in energy than the donor LUMO. Once electron transfer has occurred, the hole and electron can drift or diffuse to their respective electrodes for charge collection (Figure 1.12d) The external quantum efficiency η_{EQE} of the photovoltaic is dependent on the efficiencies of each process such that,

$$\eta_{EQE} = \eta_A \, \eta_{ED} \, \eta_{CT} \, \eta_{CC} \tag{1.9}$$

where η_A is the absorption efficiency, η_{ED} is the efficiency of exciton diffusion, η_{CT} is the charge transfer efficiency, and η_{CC} is the efficiency of charge collection at the electrodes.

While the efficiencies of the charge transfer and charge collection cannot be overlooked, the disparity between the thickness of the absorptive layer and exciton diffusion length remains a critical concern. Efficient operation of OPVs is dependent on the behavior of the excited states in the devices, specifically the transfer of energy from the absorption site to the interface.

1.3 Probing Excited States in Photovoltaic Materials

1.3.1 Ultrafast Pump-Probe Spectroscopy

Oscillator Operation and Mode Locked Pulses

In order to perform ultrafast experiments, creation of a pulse train is necessary. By manipulating constructive and deconstructive interference in an oscillator cavity, we can create temporally short, high energy pulses to coherently excite samples in a short period of time and observe the dynamics without worry of further excitation which is presented in Figure 1.13. Operation of the oscillator begins with a Spectra Physics Millenium V laser in which 3.0 Watts of p-polarized, continuous wave, 2.33 eV light exit the laser head. After exiting the laser head, 2.33 eV light is directed towards the laser cavity by two 2.33 eV dielectric mirrors. A 10 cm convex lens focuses the light through the first inner cavity mirror (CM1, 10 cm focus) onto a 4 mm, 0.25% doped, brewster cut Titanium-Sapphire (Ti:Sapph) crystal.

Light is absorbed in the gain medium with an efficiency of about 80% with emission

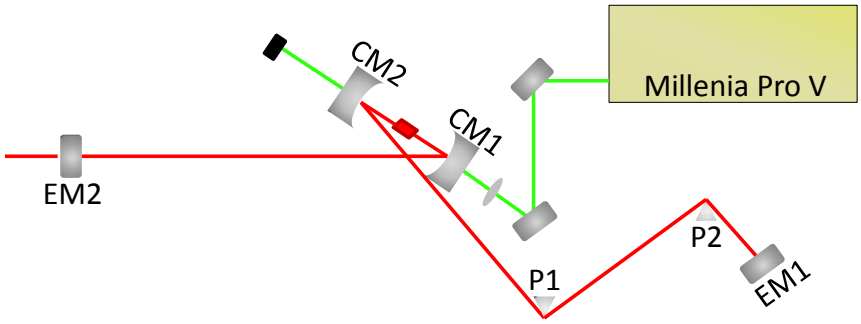

Figure 1.13: Top-down view of the oscillator. CM represents the inner cavity mirrors, P1 and P2 are the prism pair, EM1 is the end mirror and EM2 is the output coupler. The black square is an anodized aluminum block for light dumping.

energies between 1.9 eV and 1.13 eV.[51;52] Photons that traverse the cavity and re-enter the gain medium cause stimulated emission, amplifying the gain of the frequency of the photon. As long as conditions for population inversion are met, lasing in the cavity can be achieved. Frequency doubled Nd:YAG lasers with a Ti:Sapph gain medium, as in our laser system, have optimum operation energies around 1.55 eV.

After exiting the gain medium, light is reflected of the second cavity mirror (CM2, 10 cm focus) and directed towards a pair of fused silica prisms. Prisms are set at the brewster angle at a distance of 53.5 cm and correct for group velocity dispersion created in the oscillator cavity. Increasing or decreasing the intraprism path length will adjust the compensation of the group velocity dispersion. Photons are reflected back through

the prisms and gain medium by an end mirror (EM1, ∞ focus), towards the output coupler (EM2, ∞ focus) where some radiation exits the cavity.

In order to achieve the pulse train required for pump-probe measurements, different modes of the laser need to be locked in phase.[53;54] A laser is considered mode locked when all pulses constructively interfere at on point in time and deconstructively interfere at all other points in time, thereby creating a single pulse. There are several methods to mode locking a laser, including active, passive, and Kerr-lens mode-locking. Active mode-locking involves the use of an acousto-optic device placed in the cavity, modulating the amplitude of the light and locking the modes in the gain bandwidth. Passive mode locking incorporates a saturable absorber that decreases its absorption as the intensity of the light increases. After several passes through the laser cavity, continuous selective amplification results in mode-locking of the laser. Kerr-lens mode-locking is similar to a passive mode-lock but there is no saturable absorber. By adjusting the focus of the low intensity light relative to the high intensity light, the high intensity light is selectively amplified, creating a pulse train.

In our laser setup, we adopt a Kerr-lens mode-locked, 4-mirror laser with slight adjustments to orientation and path lengths.[55] Mode-lock is achieved through rapid movement of a translation stage underneath prism 2 (P2), causing a strong perturbation in the dispersion. Achieving mode-lock increases the output power from 100 mW to 150 mW with a gain in bandwidth from 5 nm to 50 nm centered at 800 nm. Pulses have a repetition rate of 80 MHz with a pulse width between 5 fs and 10 fs.

In order to amplify the pulse train, pulses must be stretched in time to prevent high energy, temporally short pulses from damaging sensitive optics in the regenerative amplifier. Upon exiting the oscillator, the pulse train is incident on a 1500 g/mm stretcher grating. Through the use of spherical mirrors and other reflective optics, the pulse makes 4 total hits on the grating, returning at a slight upward angle and directed into the regenerative amplifier.

Regenerative Amplification of a Pulse Train

The energy required to perform ultrafast measurements, create optical parametric amplifiers, 2 dimensional electronic spectroscopy, etc. surpasses the energy put out by the oscillator. Thus, amplification of the pulse train is necessary to fulfill the needs for the aforementioned experiments and occurs in the regenerative amplifier (regen) A Spectra Physics Empower 15 pumps the regen cavity, as shown in Figure 1.14 with 10 W of p-polarized, 2.35 eV light. The laser is focused down to a beam waist of 470 μm at a 0.25 % doped, 4 mm Ti:Sapph crystal located 38.8 cm from CM1. 1.55 eV light travels another 71.2 cm before reflecting off the second cavity mirror (CM2, 1 m focus), then 1.1 m towards the third cavity mirror (CM3, ∞ focus). Excess 1.55 eV light not absorbed by the crystal is reflected back to the crystal with the return mirror (RM, 50 cm focus). When exchanging the high reflective dielectric mirror with a 95% output coupler, 1.2 W are measured behind the output coupler.

As the seed pulse enters the regen, two fused silica polarization cubes are used to send

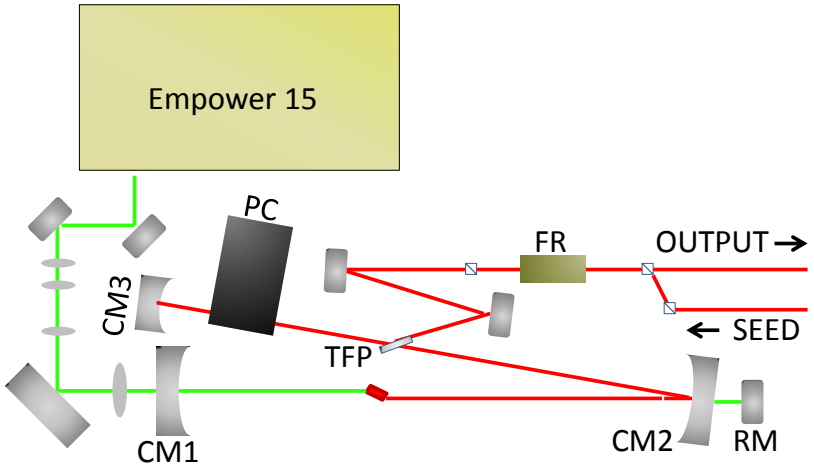

Figure 1.14: Top down schematic of the regenerative amplifier. CM1, CM2, and CM3 are the 3 cavity mirrors while RM is a return mirror for increased gain. FR is the Faraday Rotator responsible for one-way polarization rotation to enter the cavity off the thin film polarizer (TFP) while the Pockels cell (PC) traps the pulses by rotating the polarization of the light.

s-polarized light through the Faraday Rotator (FR) towards the cavity. The Faraday Rotator is a one way polarization rotator which affects the incoming beam and rotates it 90° but does not adjust the polarization of the outgoing pulse. After passing through the Rotator, the p-polarized light reflects off a thin-film polarizer towards the Pockels Cell. In order to amplify the pulse train, individual pulses need to become trapped in the cavity to ensure adequate amplification. A Pockels Cell is employed to trap the pulses, allow for amplification, then eject the amplified pulse.

When the correct voltage is applied to the Pockels Cell, known as the quarter wave voltage (3.6 kV), polarized light that travels through the Pockels Cell is rotated 45° per pass. When no voltage is applied, the polarization is not rotated and the light exits the cavity in the same path it came in. By using both of these properties, we can trap pulses for amplification and release them at our discretion. As the quarter wave voltage is applied, the seed pulse enters the cavity through the thin film polarizer and makes two passes through the Pockels Cell, which rotates the s-polarized pulse to a p-polarized pulse. The voltage to the Pockels Cell is turned off and the p-polarized pulse can make a desired number of passes in the cavity and absorb the energy in the crystal. When the desired number of passes have been made, another quarter wave voltage is applied to rotate the polarization 90° and allowing the pulse to leave the cavity. The p-polarized pulse then travels through the Faraday Rotator, where the polarization is not rotated, with an energy of 1 mJ/pulse.

Upon exiting the regen, pulses are sent into the compressor consisting of two 1200

g/mm gratings. Two hits are observed on each grating to counteract the dispersion from the stretcher and regen optics, resulting in a compressed 80 fs pulse as measured through 1.55 eV autocorrelation in a BBO crystal. Each grating is 91% efficient, resulting in a total loss of 32% and 680 mW exiting the compressor.

Non-collinear Optical Parametric Amplification

Probing excited states of a variety of materials requires tunability of excitation pulses. Emission from Ti:Sapph lasers are limited to 1.55 eV and through use of frequency doubling crystals, 3.1 eV and 4.66 eV light can be achieved. However, by utilizing processes in a non-collinear parametric amplifier (NOPA), a continuum of excitation wavelengths in the visible and near infrared can be produced to excite a very broad range of samples.[56;57;58;59]

Implementation of nonlinear processes was made possible with the increase of high energy lasers from millijoule to multijoule and creation of nonlinear crystals such as β-barium borate (BBO).[56] The nonlinear crystals lack inversion symmetry and show χ^2 (second order) nonlinearity. The BBO crystal is birefringent which means the index of refraction of the material is dependent on the polarization of light. If we consider two beams of different wavelengths with polarization difference of 90°, there exists an angle of the crystal where the indices of refraction are equal in both beams and is a crucial property in the phase matching of the beams.

Optical parametric amplification utilizes two beams, a high energy pump *(p)* and

low energy signal *(s)*. Energy is conserved in the nonlinear process as shown in Equation 1.10 where ω represents the frequency of the pulse and p, s, and i subscripts stand for the pump, signal, and idler, respectively. Momentum is also conserved between the wave vectors, k, of the idler, pump, and signal in Equation 1.11.

$$\hbar\omega_p = \hbar\omega_s + \hbar\omega_i \tag{1.10}$$

$$\hbar k_p = \hbar k_s + \hbar k_i \tag{1.11}$$

In the NOPA setup, the high energy pump beam and signal are incident on the BBO crystal in a noncollinear fashion such that the angle between the two beams is α and the angle between the idler and signal is Ω as shown in Figure 1.15. In order to achieve amplification in the NOPA, the phase matching angle must be satisfied such that both the parallel and perpendicular wave vector equations are zero.

$$\Delta k_{par} = k_p cos\alpha - k_s - k_i sin\Omega = 0$$

$$\Delta k_{perp} = k_p cos\alpha - k_s - k_i sin\Omega = 0$$

If we increase the frequency of the signal by $\Delta\omega$, the idler will decrease by $\Delta\omega$ and to first order approximations, we can describe the relationship between the group velocity

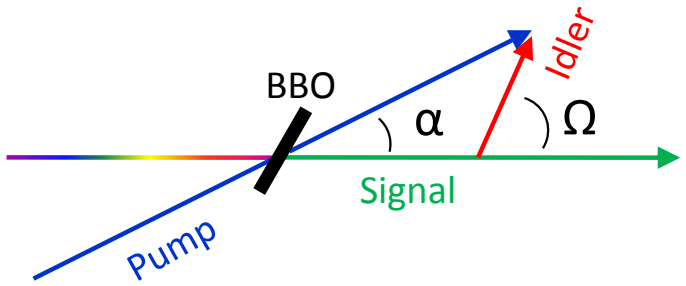

Figure 1.15: Phase matching the pump, signal, and idler beams with phase matching angle α and idler emission angle Ω.

of the signal (ν_{gs}) and the idler (ν_{gi}) as:

$$\nu_{gs} = \nu_{gi} cos\Omega \tag{1.12}$$

In a collinear setup, the phase matching angle $\alpha = 0$ which limits the bandwidth of the generated pulses. However, noncollinearaity allows for the generation of broadband pulses with the correct phase matching and BBO crystal angle θ, which is dependent on the cut of the crystal. The optimal geometry phase matching at one crystal angle to produce a broadband pulse is $\alpha = 3.7°$ and $\theta = 31.3°$ for type I BBO crystals. Care must be taken to reduce temporal chirp as it will limit the temporal overlap of the pump with multiple frequencies of the white light signal and reduce the output bandwidth.

Sources of Pump Probe Signals

Probing the excited state of molecules can lead to very useful information about the excited state dynamics of molecules but pump probe spectra must be discerned in both frequency and time. To determine the dynamics, the change in optical density, ΔO.D., is measured every other shot by measuring the transmission of the white light probe with and without the presence of the pump as shown in Equation 1.13.

$$\Delta O.D.(\lambda) = -log\left(\frac{I(\lambda)}{I_0(\lambda)}\right) \tag{1.13}$$

In time integrated, UV/Vis spectroscopy (Figure 1.16a), transitions from the ground state to higher lying excited states are probed. Pump-probe spectra is more complicated due to addition of complicated relaxation and time dependent dynamics. Similar to UV/Vis spectroscopy, absorption from the excited state to unoccupied higher lying states at some wavelength λ (Figure 1.16b) can be observed and is called transient absorption or excited state absorption. As the excited state is depopulated, the transient absorption will also decay. If the excited state transitions to another excited state, it may be possible to see transient absorption from the newly populated state and the time dependence of these features should be correlated.

Due to population of the excited state when the pump is present, the ground state no longer has the same amount of absorbers of wavelength λ to populate the excited states. A change in optical density is observed as more probe light reaches the detector and is observed as a negative feature at λ in the spectra, called a ground state hole.

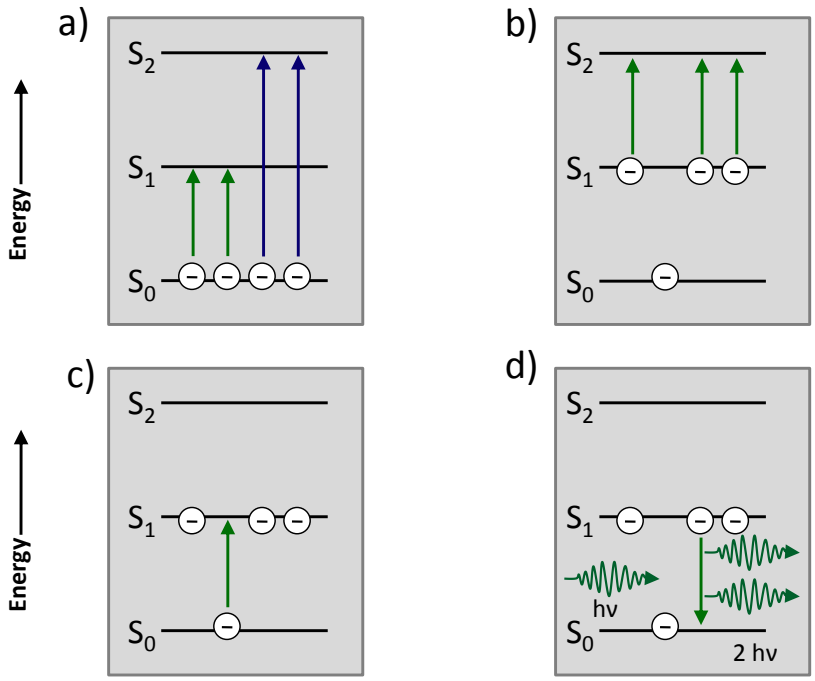

Figure 1.16: Representation of processes occurring in pump probe spectroscopy. Typical ground state absorption from the ground state to higher excited states is shown in panel a). Transient absorption from the excited to higher states can be seen in panel b). The ground state hole, lack of absorption from the ground state, is seen in c). Stimulated emission is shown in panel d).

The ground state hole has a similar shape as the ground state absorption bands due to missing transitions at wavelength λ. If there is relaxation to the ground state, the negative ground state hole feature will become more positive.

While in the excited state, presence of light at wavelength λ can stimulate radiative transitions from an excited state to lower states (typically $S_1 \rightarrow S_0$) and is called stimulated emission.[25] Stimulated emission causes more light of wavelength λ to reach the detector and is seen as a negative feature in the spectra.

All observed processes cause more or less light to reach the detector but are convoluted with one another and only net changes in the light are seen (Figure 1.17). Attributing pump probe spectral features to excited state processes can be aided through measurement of time integrated absorption or fluorescence. Furthermore, the spectral evolution of the pump probe spectra as a function of time is crucial in elucidating the excited state dynamics.

Ultrafast Measurements on Solid State Materials

Ultrafast measurements have typically been performed on sample in liquid and gaseous forms, yet probing the dynamics in thin film and solid crystals remains relatively unexplored. With the developments of OLED's and OPV's, investigation into excited state dynamics in thin film materials is crucial to improving device performance. Several issues restrict the ability to probe excited states in solid state devices, specifically contrasted with compounds in solutions.

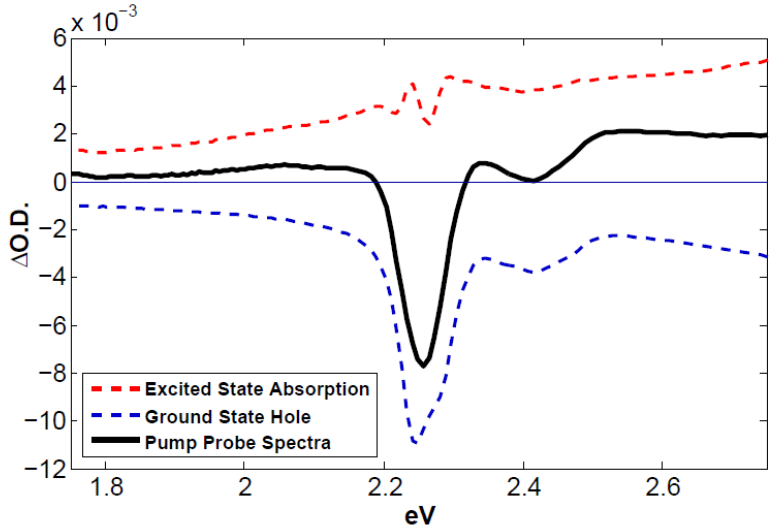

Figure 1.17: Deconvoluted pump probe spectra in PtOEP. A ground state hole (blue dash) is overlapped with a broad excited state absorption (red dash) and results in the observed pump probe spectra (black solid). Fluctuation in the transient absorption is due to noise in subtraction of the ground state hole from the pump probe spectra.

First, the excitation pulses must continually excite new molecules to prevent any bleaching or degradation of the sample. In liquid samples, solutions are flowed through a 1 mm path length cell using a Cole-Parmer gear pump at an approximate rate of 1 mL/s. 25-30 mL of solution are used during each pump-probe scan allowing for fresh sample to be probed at any time during the scan. Solid state devices present a more difficult path to acquiring fresh, unbleached samples during scans. Figure 1.18 represents a pump-probe spectra of a 60 nm film of PtOEP in which the sample is stationary (a) and manually translated (b). Scans were averaged 50 seconds per time point, totalling 11 min per data collection. After 11 minutes under laser excitation, magnitude of the ground state bleach in the static sample is $\sim 1/2$ the magnitude of the translated sample. Variations in the excited state densities will necessitate much longer averaging times to achieve a good signal to noise ratio.

In order to combat loss of signal due to bleaching, construction of a mechanical device to refresh solid state sample is imperative. Figure 1.19 is a picture of the apparatus built to rotate thin film samples. Many ideas were explored to continuously translate the film, including the purchase of piezo motor stages to move in "S" like patterns and utilizing already acquired Newport rotation mounts. However, building a rotation stage using a small motor and ball bearings in a pulley style represented the simplest form of sample translation. Parts were machined to create flat surfaces as any perturbation in planar rotation can result in unnecessary scatter and inaccuracies in excitation density measurements. Implementation of the rotation stage has resulted in no loss of signal,

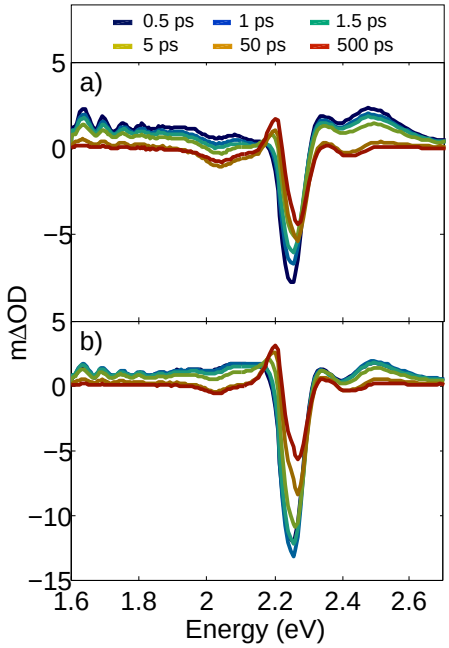

Figure 1.18: Pump-probe spectra of a 60 nm PtOEP film without (a) and with (b) sample translation.

no excess scatter or restrictions on measurements, and no significant visible bleaching of the sample.

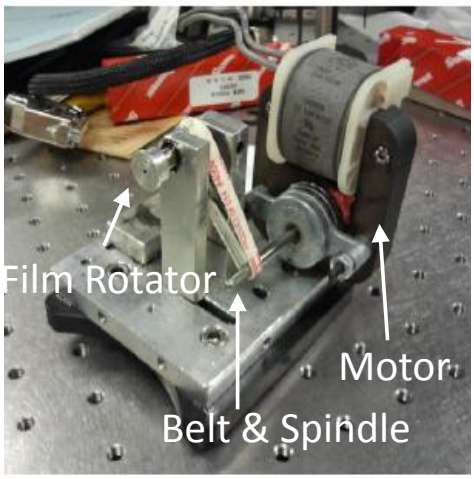

Figure 1.19: Custom made rotation stage to replenish the sample and prevent photobleaching.

Secondly, all samples must have optical clarity. Significant loss of the probe signal will decrease, if not prevent, all ability to measure excited states. Ultrafast measurements on single crystals have been performed and represent limitations on probe transmittance through sample as shown in Figure 1.20. Due to the high optical density of the crystal, probe energies higher than 1.8 eV have a significant decrease in ΔO.D.

signal versus noise. Magnitude of the probe light exiting the crystal is also significantly decreased at these energies. Limitations on the thickness of thin films should also be recognized to allow adequate probing of the sample. In all measurements presented, film thicknesses do not exceed 100 nm and are vapor deposited on a 1.5" quartz substrate. During vapor deposition, samples are concurrently deposited on quartz and a silicon substrate. Samples deposited on silicon are used for ellipsometric measurements to determine actual film thickness. The quality of the thin films and thickness is crucial for observing small changes in ultrafast pump probe spectra.

Finally, presence of oxygen can affect the population and charge transfer rates of triplet states.[60;61;62] Molecular oxygen can quench excited triplet states via the mechanism in Equation 1.14. Unlike most molecules, oxygen is a triplet in its ground state. Upon interaction with the triplet excited state, energy is transfer from the triplet state on the chromophore to the oxygen, promoting the oxygen to a metastable singlet state and returning the chromophore to the ground state. The process takes nanoseconds to occur due to the close proximity of the molecules but quenches phosphorescence through deactivation of the chromophore excited state *(M*)*.

$$^3M* + ^3O_2 \rightarrow ^1M + ^1O_2* \tag{1.14}$$

To prevent any possibility of excited state quenching, flowed samples are purged with nitrogen or argon at 5 psi for 5 minutes, then sealed with rubber stoppers and Parafilm to prevent reintroduction of oxygen. In solid state samples, a purge box surrounds the

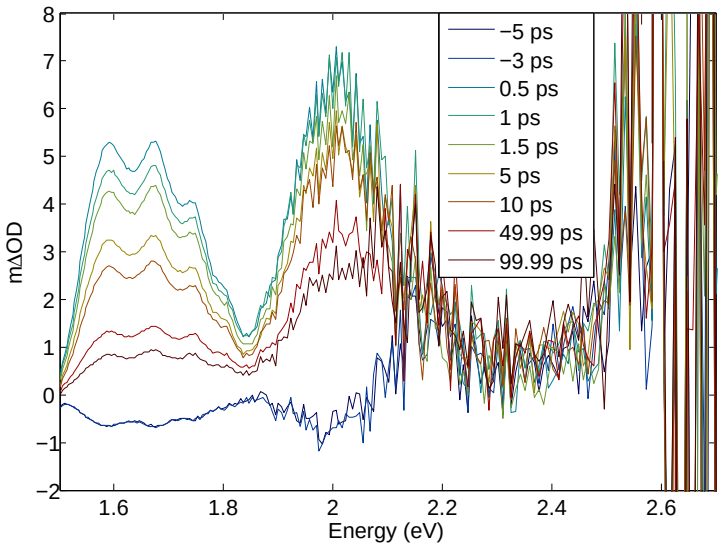

Figure 1.20: Pump-probe spectra of a 2mm x 3mm x 1mm thick G2ABDS-C314 single crystal. Probe energies above 1.8 eV have a lower signal to noise ratio than those below 1.8 eV.

rotation apparatus to prevent oxygen from reaching the sample. Openings in the box allow for the entrance and exit of light, along with a purge line connected to a nitrogen tank. The box is purged with nitrogen for approximately 1 min at a pressure of 10 psi, then reduced to less than 5 psi for the remainder of the experiment. Pump-probe has been performed on PtOEP 60 nm film with and without the purge box as represented in Figure 1.21. Within the first 100 ps, no noticeable difference is observed in the pump-probe spectra under the presence of oxygen and under nitrogen. However, the 500 ps trace in panel b shows slightly more repopulation of the ground state when comparing the ΔO.D. and my indicate some excited state quenching in the oxygen environment. Although oxygen quenching typically begins to occur around 1 ns,[60;63] the affect of oxygen cannot be overlooked around 500 ps.

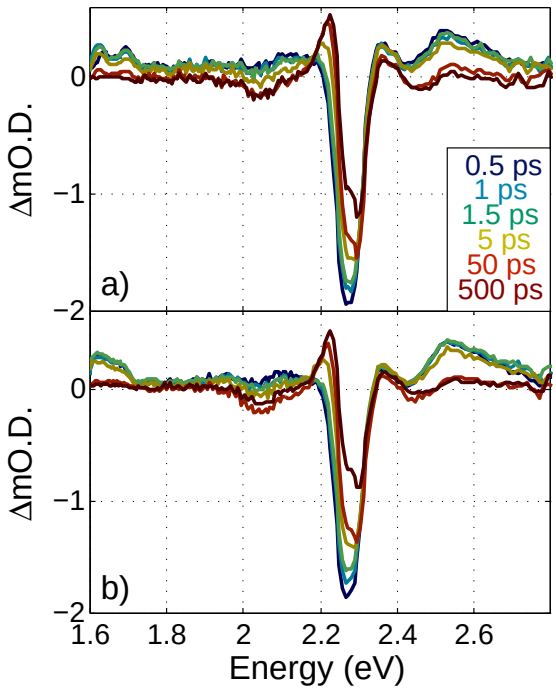

Figure 1.21: Pump-probe spectra of a 60 nm PtOEP under the same experimental conditions pumped in a container with a nitrogen environment (a) and a normal atmospheric environment (b).

Chapter 2

Picosecond Excited State Localization in Nickel Substituted Porphyrins

2.1 Introduction

Metalloporphyrins, derivatives of chlorophylls, have been under study due to their applications in biological and photosynthetic models,[64;65] strong redox properties,[66;67;68;69] and ability to form strong arrays and reaction centers.[70;71;72] Nickel porphyrins remain under investigation due to their fundamental excited state processes that are useful in photovoltaics including internal conversion, intersystem crossing and electron and energy transfer.[73;74;75;76;5;77;78;79;80]

Nickel porphyrins have been shown to undergo rapid excited state deactivation to $d_{(x^2-y^2)}$ within $\sim$ 1 ps.[73;74;75;5;77;78;81;82;83] There is some disagreement, however, on the excited state dynamics upon excitation. Several results have indicated that upon excitation to S_2 the excited state internally converts to S_1.[74;73;77;78;84]. Recent ultrafast pump-probe results on nickel(II)tetrakis(2,4,6-trimethylphenyl)porphyrin (NiTMP) revealed stimulated emission upon excitation to S_1 but no stimulated emission with S_2 excitation.[5] Lack of stimulated emission led to assignment of another deactivation pathway $S_2 \rightarrow d_{(x^2-y^2)}$ within the time resolution of 120 fs.

Other transient absorption studies contradicted $S_2 \rightarrow d_{(x^2-y^2)}$ transitions inferred by Zhang.[74] Pump probe measurements on nickel octaethyl porphrin (NiOEP) and nickel tetrapheynyl porphyrin (NiTPP) lacked the presence of stimulated emission in both B band and Q band excitation. The difference in energy between the $^1(\pi,\pi^*)$ and $^3(d_{z^2},d_{x^2-y^2})$ was estimated to be 10,000 cm^{-1} so transition from S_1 $^1(\pi,\pi^*) \rightarrow$ $^3(d_{z^2},d_{x^2-y^2})$ would generate vibrationally hot molecules in the $(d_{z^2},d_{x^2-y^2})$ manifold. Two decay processes were observed: A fast 1 ps decay attributed to intramolecular vibrational relaxaton and a 10-20 ps decay assigned as a change between ruffled and planar conformations. The $^1(d_{z^2},d_{x^2-y^2})$ and $^3(\pi,\pi^*)$ were initially included as intermediates in the deactivation of S_1, but no absorption between 750-850 nm was seen, indicative of $^3(\pi,\pi^*)$ species. No spectral evidence was presented for intermediates between $^1(\pi,\pi^*)$ $\rightarrow$ $^3(d_{z^2},d_{x^2-y^2})$ transitions, but were not excluded.[74]

Spectral evolution of pump probe studies on nickel porphyrins indicate transitions

to lower lying states before repopulation of the ground state.[73;74;85;5;78;86] The excited intermediate state has also been disputed based on experimental and theoretical results. Kobayashi et. al. attributed the spectral change to the intermediate $^1B_{1g}$ $^1(d_{z^2},d_{x^2-y^2})$ state.[87] Kim et. al. predicted the lowest lying $^3B_{1g}$ responsible for the spectral shape and is populated through $^1B_{1g}$ and $^3(\pi,\pi^*)$ intermediates.[75] Resonant raman experiments on NiOEP supported the $^1B_{1g}$ intermediate as the $^1B_{1g}$ state is stabilized upon conversion from the ruffled macrocycle of the ground state to a planar form.[88] The planarization predicted energetic shifts of the Q and B bands and explained the derivative shape observed in transient absorption studies.

Time dependent density functional theory (TDDFT) studies predicted several excited states between the excited S_1 state and the ground state.[84] These studies found the energy of the $^1B_{1g}$ state lies above the S_1 state and cannot play a role as an intermediate in the deactivation of S_1. The $^3B_{1g}$ state, corresponding to $^3(d_{z^2},d_{x^2-y^2})$, was predicted as the lowest excited state and exhibits a relaxed geometry that increases the Ni-N bond length and reduces macrocycle ruffling by 75%. $^1B_{1g}$ was concluded to cause the derivative like spectra and the lowest intervening state in ground state relaxation ($^1(\pi,\pi^*) \rightarrow {}^3(d_{z^2},d_{x^2-y^2}) \rightarrow$ ground state).[84] X-ray transient absorption spectroscopy experimentally confirmed the increase in the Ni-N bond length and planarization of the nickel porphyrin upon transfer to the $^3(d_{z^2},d_{x^2-y^2})$ with singly occupied $3d_{z^2}$ and $3d_{x^2-y^2}$ molecular orbitals.[89]

While the excited states of nickel porphyrins have been studied in depth, the disagreement of the excited state dynamics must be investigated to effectively incorporate them into photovoltaic and other electronic devices. Here we present the excited state dynamics of nickel(II) octaethyl porphyrin (NiOEP) and nickel(II) meso-tetrakis(2,4,6-trimethylphenyl)porphyrin (NiTMP) in aqueous solution following excitation at multiple energies.

2.2 Experimental Procedure

2.2.1 Materials

Nickel octaethyl porphine (NiOEP) was purchased from Sigma Aldrich with no further purifications. Nickel(II) meso-tetrakis(2,4,6-trimethylphenyl)porphyrin (NiTMP) was synthesized under a previously described procedure using free base meso-tetrakis(2,4,6-trimethylphenyl)porphyrin (H_2TMP).[5] Briefly, 0.099 grams of H_2TMP was dissolved in 150 mL of dimethyl formamide (DMF) and treated with 1.272 grams nickel acetate $(Ni(OAc)_2 \cdot 4H_2O$. The solution was placed in an oil bath and refluxed under argon and heat for 24 hours, then was allowed to cool. The greenish solid residue was treated with 50 mL DMF, 50 mL water with $NaHCO_3$, then 50 mL brine. The organic layer was extracted using a separatory funnel, and rinsed again with 50 mL water with $NaHCO_3$ and 50 mL brine. The NiTMP compound was purified using a silica gel column and flushed with 2:1 mixture of hexanes:methylene chloride, resulting in a purple solid. NiTMP was

analyzed through NMR (Appendix A.1) and purity was checked through chromatography. Finally, NiOEP and NiTMP were dissolved in toluene at concentrations of 150 μM for absorption, emission, and time resolved measurements. The molecular structures are shown in Figure 2.1.

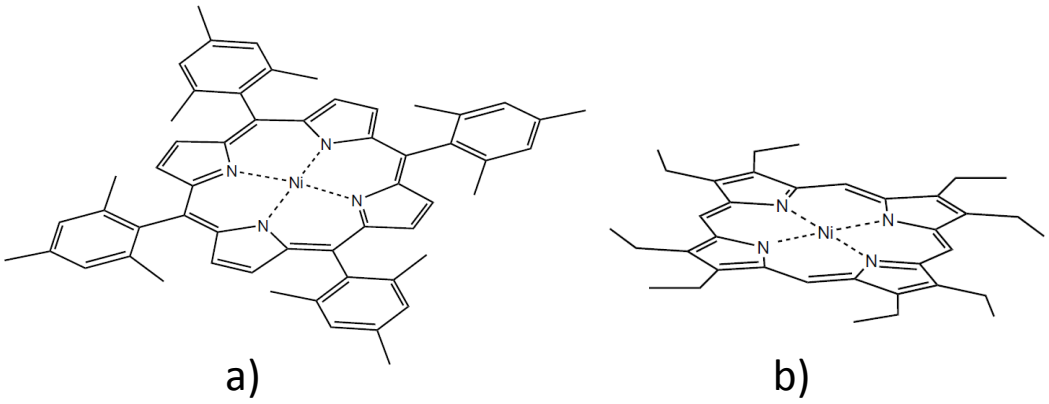

Figure 2.1: Molecular structure of a) NiTMP, and b) NiOEP.

2.2.2 Steady State Absorption and Emission

Absorption and emission measurements were performed with the aforementioned Cary 14 absorption spectrometer and Fluorolog 1680 0.2 mm double grating spectrometer. A 1 mm cuvette was used for absorption measurements to determine the optical density of the samples for ultrafast measurements. Fluorescence measurements employed front face geometry on a 1 cm cell containing 10x diluted solutions to prevent reabsorption.

2.2.3 Time Resolved Measurements

Ultrafast measurements utilized a similar setup as mentioned in the descriptive experimental section. S_1 excitation required use of the previously mentioned NOPA. Excitation light was tuned to 2.35 eV and 2.25 eV to match the Q bands for NiTMP and NiOEP, respectively, with an approximate 20 nm bandwidth (FWHM) for the excitation pulses. The repetition rate of the pulses was modulated by a beam chopper to 500 Hz and focused to a spot size of 93 μm with a 10 cm parabolic mirror. For S_2 excitation, the 500 Hz, 1.55 eV pulse train was attenuated and sent into a 1 mm frequency doubling BBO crystal resulting in 3.1 eV pulses. The excitation light was focused onto a sample with a 10 cm parabolic mirror to a spot size of 115 μm.

An 80/20 beamsplitter was used to create separate pump and probe lines. The line with 20% of the 1.55 eV light was focused onto a 2 mm thick piece of sapphire, generating a continuum probe between 1.38 eV and 2.85 eV. The probe light was focused onto the sample at the same location as the pump beam. The probe beam was collimated and refocused through a 1,1' diethyl 4,4' dicarbocyanine iodide dye filter and onto a dispersive grating. The light was detected by a Hamamatsu silicon diode array.

2.3 Results and Discussion

2.3.1 Steady State Absorption and Emission Measurements

The absorption and emission spectra of NiOEP and NiTMP are shown in Figure 2.2. NiOEP and NiTMP show a prominent B band at 3.15 eV and 2.99 eV, respectively. Q band absorption is located at 2.25 eV and 2.35 eV for NiOEP and NiTMP, consistent with previous measurements.[5;74] Nickel porphyrins are typically considered nonemitters due to their extremely low quantum yields.[90] However, Figure 2.2 appears to show the first measurements of NiOEP and NiTMP emission under B band excitation. NiOEP fluoresecence is observed at 2.16 eV (571 nm) and NiTMP fluorescence is seen around 1.91 eV (650 nm), showing a Stokes' shift of 20 nm and 123 nm, respectively. Fluorescence measurements under Q band excitation were inconclusive due to smaller Q absorption compared to the B band and increased scatter from the excitation light. The small quantum yields reported in Table 2.3.1 at the end of the chapter were from B band excitation.

The importance of emission measurements in nickel porphyrins relies on the fact that previous results have inferred the excited state dynamics based on ultrafast stimulated emission. Zhang et al. proposed different excited state deactivation pathways when exciting into the first and second excited states. Their claims were based on the presence of a short lived negative "dip" feature at 630 nm as shown in Figure 2.3 upon S_1 excitation but was absent in S_2 excitation. They assigned the negative feature to

stimulated emission ($S_1 \rightarrow S_0$) and further claimed excitation into S_2 does not result in population of S_1 through internal conversion but rather deactivates directly to a ^{3}(d,d). The fluorescence measurements presented in Figure 2.2 indicate that upon population of S_2, the radiative $S_1 \rightarrow S_0$ transition is observed at 650 nm (1.91 eV). If the relaxation pathway presented by Zhang was correct, no fluorescence should be observed when exciting to S_2. Furthermore, there is a 20 nm discrepancy in the wavelength of the $S_1 \rightarrow S_0$ transition. The time integrated results imply a simple picture of internal conversion (IC) followed by excitation localization (EL) ($S_2 \xrightarrow{IC} S_1 \xrightarrow{EL} {}^3$(d,d)). The full excited state dynamics will be examined further in the next section.

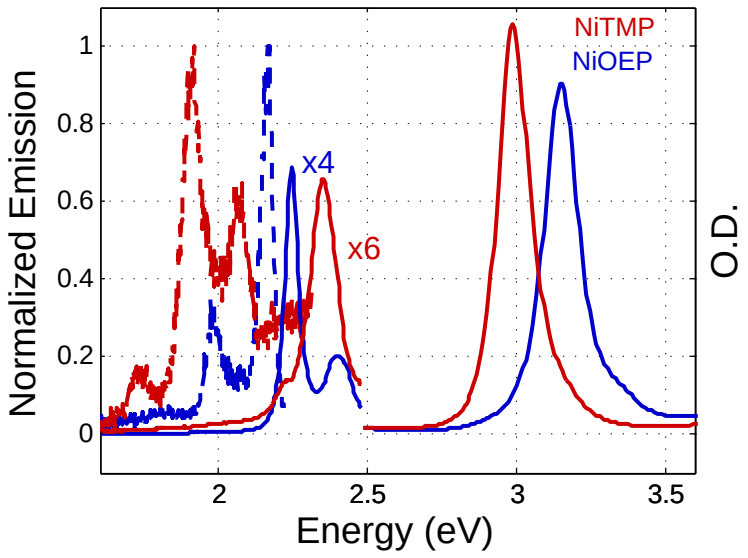

Figure 2.2: Absorption (—) and emission (- - -) spectra of NiTMP (red) and NiOEP (blue). Absorption and emission values are shown in Table 2.3.1

Molecule	B_{abs} (eV,nm)	Q_{abs} (eV,nm)	Fl. (eV,nm)	ϕ_{Fl}
NiTMP	(2.99,415)	(2.35,527)	(1.91,650)	$<10^{-3}$
NiOEP	(3.15,393)	(2.25,551)	(2.16,573)	$6x10^{-3}$

Table 2.1: Absorption, fluorescence, and quantum yield (ϕ_{Fl}) of NiTMP and NiOEP.

2.3.2 Excited State Dynamics of Nickel(II) Porphyrins

Previous pump-probe measurements on NiTMP by Zhang[5] led to a proposed relaxation pathway based on their ultrafast results. There are, however, a few inconsistencies with their studies presented in Figure 2.3. Under S_2 excitation, the dynamics across their white light probe are not correlated in time. There is a rise at 450 nm between 0.4 ps and 0.8 ps, then subsequent decay at 1.5 ps. The dynamics on the red side of the ground state hole show only growth as a function of time. In S_1 excitation, transient absorption on the red side of the negative feature, assigned as stimulated emission, grows between 0.4 ps and 0.6 ps, then subsequently decays. The absorption around 450 nm only decays over that time span. Since they assign the early time transient absorptions spectra to initally created singlets, changes should be correlated with one another. These observations indicate a possible problem with their time 0, temporal chirp correction and reported instrument response of 120 fs.

A second issue lies in the assignment of the negative feature to stimulated emission. If the negative feature was $S_1 \rightarrow S_0$ stimulated emission, the decay of the feature should be correlated with loss of S_1 in Figure 2.3. The feature, however, completely disappears at 0.8 ps. Transient absorption between 600-800 nm, assigned to S_1, still shows decay

over 1 and 1.5 ps while growth of a transient absorption at 550 nm, resulting from ^{3}(d,d) population, is correlated to loss of S_1.

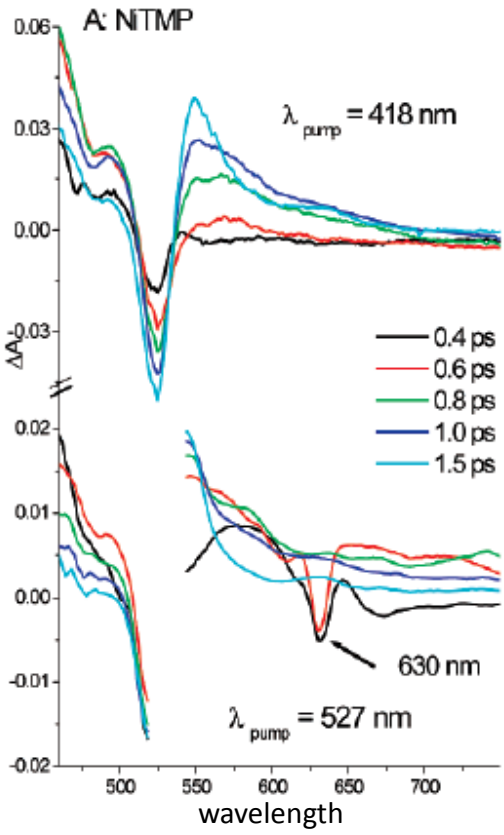

Figure 2.3: Pump-probe spectra of NiTMP under S_2 (top) and S_1 (bottom) excitation collected by Zhang and collaborators.[5]

Pump-probe measurements performed on NiOEP, PdOEP, and PtOEP in Figure 2.4 also show this negative feature around time zero when excited into the Q band. The negative feature around 1.9 eV (650 nm) for all three porphyrins appears when the pump

and probe pulses are temporally overlapped then disappears when the pulses are not overlapped. Those negative features show the same trend in all three porphyrins when compared to NiTMP, including the studies by Zhang.[5] First, the dips do not recede correlated with loss of S_1, which would occur with stimulated emission, rather they vanish when the pulses are not overlapped in time ($\sim$ 200 fs). Secondly, all S_1 excited porphyrins show an approximate 100 nm shift between detection of the negative feature and excitation wavelengths during ultrafast measurements. The detected wavelengths of these negative features also do not correspond to emission wavelengths detected through time integrated fluorescence studies. Furthermore, the fluorescence studies all show S_1 $\rightarrow$ S_0 emission when excited into S_2 (PdOEP and PtOEP will be discussed in the subsequent chapter). It is possible these features are due raman bands from the toluene solvent and have not been ruled out. The time integrated studies compounded with the ultrafast phenomenon observed in S_1 excited porphyrins reveal uncertainty with the deactivation scheme proposed by Zhang.[5]

The excited state dynamics of NiTMP, excited into S_2 and S_1, are presented in Figure 2.6. When compared to Zhang, similar spectra are observed.[5] Excitations in S_1 and S_2 (2.35 eV and 3.1 eV pump) result in excited $^1(\pi,\pi^*)$ species. In S_2 exciation a ground state hole from S_1 is observed at 2.35 eV while some scatter from the pump light in S_1 excitation obscures the ground state hole dynamics. At short pump probe delays (0.1 ps), a broad transient absorption between 1.8 and 2.8 eV is observed under both S_2 and S_1 excitations. The only disparity is under S_1 excitation, where a negative

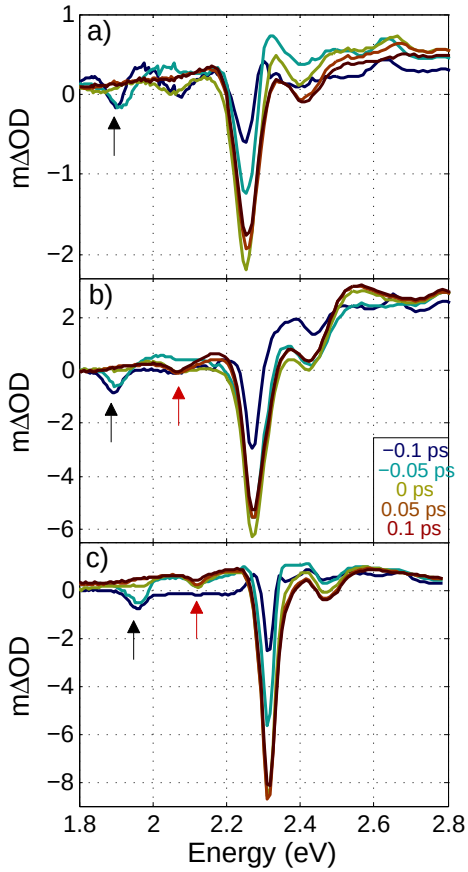

Figure 2.4: Pump-probe spectra of NiOEP (a), PdOEP (b), and PtOEP (c) in toluene under S_1 excitation. Black arrows indicate the negative feature only present during pulse overlap whereas the red arrows indicate the location of stimulated emission observed in PdOEP and PtOEP, discussed in the next chapter. The shift between excitation and the negative feature for NiOEP, PdOEP, and PtOEP is 0.35 eV (97 nm), 0.37 eV (103 nm), and 0.35 eV (102 nm).

"dip" feature at 2.0 eV is observed, consistent with previous results.[5] This feature is attributed to the pulse overlap curiosity rather than stimulated emission and stimulated emission should be observed at 1.9 eV as confirmed by fluorescence measurements in Figure 2.2. The broad transient absorption is assigned to the initially created singlet state to higher excited states, $S_1 \rightarrow S_n$. In both S_2 and S_1 emission, loss of the broad transient absorption on the red and blue sides of the ground state hole are correlated with each other, opposed to the results seen in Figure 2.3. Similarities between the spectra at the earliest time delays suggest internal conversion ($S_2 \rightarrow S_1$) within the experimental time resolution.

As the broad transient absorption decays, correlated growth at 2.25 eV is observed. An isosbestic point is seen at 2.18 eV, indicating presence of a new species. Previous transient absorption studies have observed the broad transient decay and sharp growth[73;74;75;5;77;78;81;84] and is assigned as $^1(\pi,\pi^*) \rightarrow {}^3(d_{z^2},d_{x^2-y^2})$.[84;89] Population of the $^3(d_{z^2},d_{x^2-y^2})$ state induces a conformation change of the molecule from the ruffled to the planar form. Subsequently, the planarization perturbs the molecular orbitals, causing a red-shift of the $^1(\pi,\pi^*)$ absorption and is observed as the absorption growth at 2.25 eV.

Time dependence of the $^1(\pi,\pi^*) \rightarrow {}^3(d_{z^2},d_{x^2-y^2})$ transition is presented in Figure 2.7. Decay of the broad $^1(\pi,\pi^*)$ transient absorption and growth of the $^3(d_{z^2},d_{x^2-y^2})$ absorption were measured at 2.5 eV and 2.25 eV, respectively. The time dependence of $^1(\pi,\pi^*) \rightarrow {}^3(d_{z^2},d_{x^2-y^2})$ was fit with a stretched exponential function shown in Equation

2.1 while loss of the $^3(d_{z^2},d_{x^2-y^2})$ was fit with a single exponential.

$$y = Ae^{(\frac{-t}{\tau})^{\Gamma}} \tag{2.1}$$

The 410 fs time constant for formation of the $^3(d_{z^2},d_{x^2-y^2})$ was consistent with previous results.[5] However, the stretched exponential function defines a system in which the initially excited $^1(\pi,\pi^*)$ species is vibrationally hot. As the electron vibrationally relaxes in the (π,π^*) excited state, the rate of $^1(\pi,\pi^*) \rightarrow {}^3(d_{z^2},d_{x^2-y^2})$ transfer decreases, as defined by Γ and shown in Figure 2.5. Vibrational relaxation of the $^3(d_{z^2},d_{x^2-y^2})$ state was not observed but would be difficult to discern due to the blue shifting of the broad transient absorption to the (d,d) state and the close proximity of the absorption to the ground state hole. When forming the $^3(d_{z^2},d_{x^2-y^2})$ state, the molecule is conforming to a more planar geometry and the only observed transient absorption is due to the perturbed ground state and not the $^3(d_{z^2},d_{x^2-y^2})$. Therefore, detection of vibrational relaxation through observation of blue shifting of the transient absorption is not possible. Furthermore, the presence of any intermediate species between $^1(\pi,\pi^*)$ and $^3(d_{z^2},d_{x^2-y^2})$, such as $^3(\pi,\pi^*)$ and $^1(d_{z^2},d_{x^2-y^2})$, is not observed. Population of $^3(\pi,\pi^*)$ would cause a slight change of the broad excited state absorption accompanied by growth of transient absorption around 1.55 eV.[74;5] If $^1(d_{z^2},d_{x^2-y^2})$ played a role as an intermediate, it would be difficult to detect. The $(d_{z^2},d_{x^2-y^2})$ state is optically dark under these studies as no excited state absorption of the electron in the $d_{x^2-y^2}$ orbital is observed in the energy range of the probe. The transient absorptions observed due

to population of the $d_{x^2-y^2}$ orbital are from the ground state π orbitals perturbed by molecular conformation. Decay of the $^3(d_{z^2},d_{x^2-y^2})$ through repopulation of the singly occupied d_{z^2} was measured with a single exponential of (230 $\pm$ 10) ps, consistent with past results.[5]

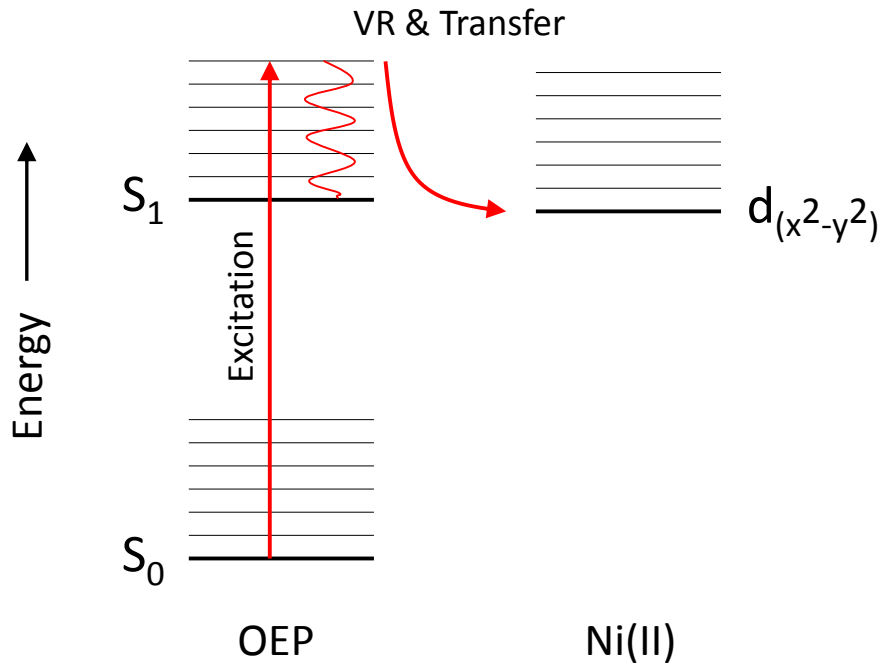

Figure 2.5: Schematic showing the change of the transfer rate due to vibrational relaxation (VR).

The excited state of NiOEP in Figure 2.8 reveals similar dynamics as NiTMP. While not observed in Figure 2.8b but seen in Figure 2.4, the pulse overlap phenomenon is observed under Q band excitation in Figure 2.4a. At early time delays, a broad transient

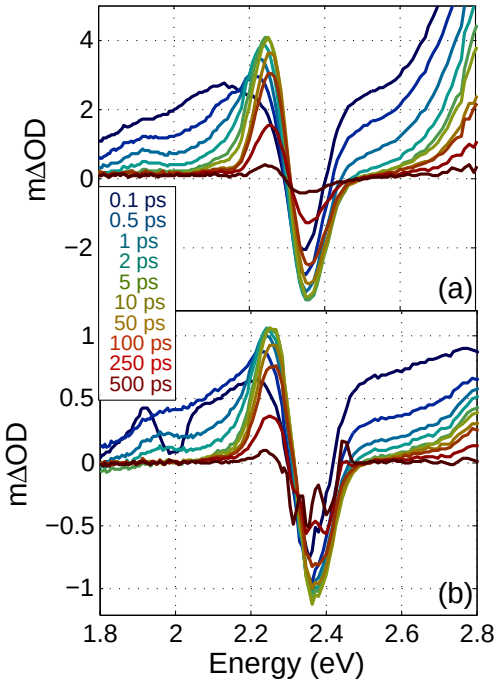

Figure 2.6: Full frequency, pump-probe spectra of NiTMP excited into S_2 (a) and S_1 (b).

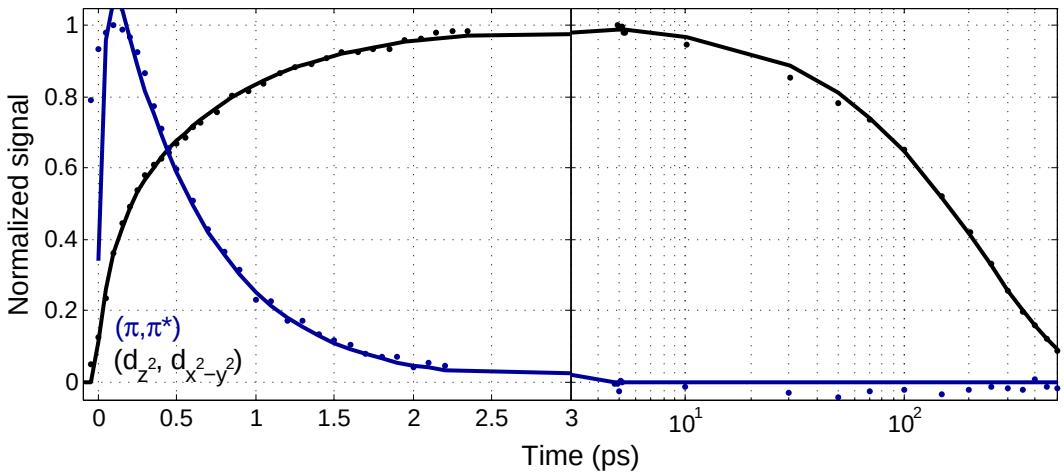

Figure 2.7: Linear and logarithmic plot of the transient decay of (π,π*)(blue) at 2.5 eV and growth of (d_{z^2},$d_{x^2-y^2}$)(black) at 2.25 eV in NiTMP. The (π,π*) $\rightarrow$ (d_{z^2},$d_{x^2-y^2}$) transition has been fit with a stretched exponential (solid line) while loss of the (d_{z^2},$d_{x^2-y^2}$) is fit with a single exponential.

absorption spans 1.8 eV to 2.8 eV, overlapping the ground state hole at 2.5 eV and is due to the optically created $^1(\pi,\pi^*)$ state. The transient absorption decay on both sides of the ground state hole is temporally correlated as expected with decay of the $^1(\pi,\pi^*)$ state. Loss of the broad $^1(\pi,\pi^*)$ transient absorption is accompanied by growth at 2.18 eV, corresponding to the $^3(d_{z^2},d_{x^2-y^2})$ state. Analysis of the transient dynamics in both B and Q band excitation indicate rapid internal conversion from $S_2 \rightarrow S_1$ when excited into the B band.

Decay of the $^1(\pi,\pi^*)$ state and growth of the $^3(d_{z^2},d_{x^2-y^2})$ state were detected at 2.5 eV and 2.19 eV, respectively, and is presented in Figure 2.9. The transition from $^1(\pi,\pi^*)$ $\rightarrow$ $^3(d_{z^2},d_{x^2-y^2})$ was fit with a stretched exponential function with a time constant of (2.2 $\pm$ 0.16) ps. As with NiTMP, the stretched exponential fit indicates vibrational relaxation of the $^1(\pi,\pi^*)$ with increasing $^1(\pi,\pi^*)$ lifetime during thermalization of the excited state, consistent with previous hypotheses of NiOEP.[74] After population of the $^3(d_{z^2},d_{x^2-y^2})$, the NiOEP adopts a planar molecular configuration like that observed in NiTMP.[84] Repopulation of the singly occupied $^3d_{z^2}$ results in a ground state with a time constant of (270 $\pm$ 50) ps. The time constants for NiTMP and NiOEP are shown in Table 2.3.2.

Further analysis into the presence of intermediate states in the full frequency spectra can be observed in Figure 2.10. Two separate time delays were selected as representations of the $^1(\pi,\pi^*)$ and $^3(d_{z^2},d_{x^2-y^2})$ transient spectra. A 50 fs trace was chosen as the best representation for the $^1(\pi,\pi^*)$ with minimal population of the $^3(d_{z^2},d_{x^2-y^2})$.

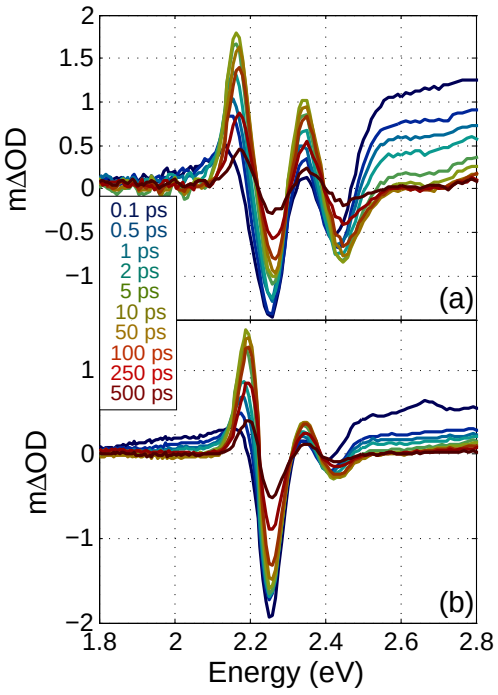

Figure 2.8: Full frequency, pump-probe spectra of NiOEP under S_2 (a) and S_1 (b) exctation.

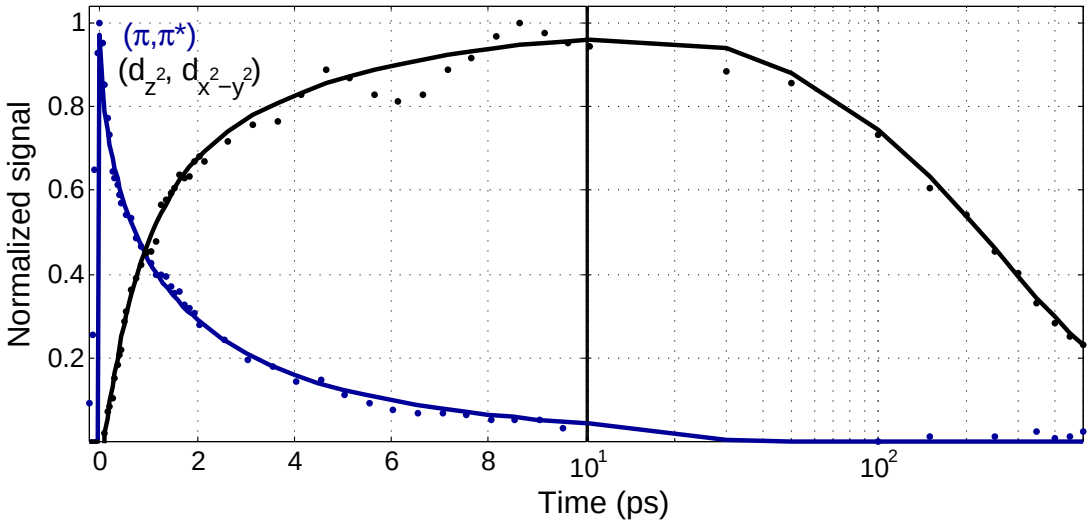

Figure 2.9: Decay of (π,π*) (blue) at 2.6 eV and growth of the (d_{z^2},$d_{x^2-y^2}$) (black) at 2.19 eV in NiOEP. Both (π,π*) decay and (d_{z^2},$d_{x^2-y^2}$) growth have been fit with a stretched exponential (solid line) and results are shown in Table 2.3.1.

Likewise, a late time delay of 50 ps represents the $^3(d_{z^2},d_{x^2-y^2})$ with little $^1(\pi,\pi^*)$ contribution. All full frequency pump probe delays were fit as a linear combination of the spectra representing these states, shown in Equation 2.2.

$$\Delta O.D.(E) = A * M(E) + B * N(E) \tag{2.2}$$

A and B represent weight parameters for the full frequency spectra, M and N, and the resulting optical density at each energy, *(E)*. Only the weights of the two full frequency traces, A and B, were optimized to fit each time trace.

Three chosen time delays of 200 fs, 500 fs, and 5 ps are shown in Figure 2.10 though all pump probe delays were fit and are shown in Appendix A.2. All full frequency optimizations show good agreement with the data, further reinforcing the lack of intermediates with only the spectral presence of $^1(\pi,\pi^*)$ and $^3(d_{z^2},d_{x^2-y^2})$ states. The optimized weight parameters of A and B for each time delay are plotted in Figure 2.11 and fit with a stretched exponential function. A time constant of (1.94 $\pm$ 0.40) ps and (260 $\pm$ 60) ps were determined as formation and loss of the $^3(d_{z^2},d_{x^2-y^2})$ state, respectively. Figure 2.9 and 2.11 reveal near identical behavior which should be expected since both data sets originate from a single set.

2.4 Conclusions

The presented work clarified some ambiguous experimental results in NiTMP. Excitation in the B and Q band reveal similar dynamics due to internal conversion, opposed

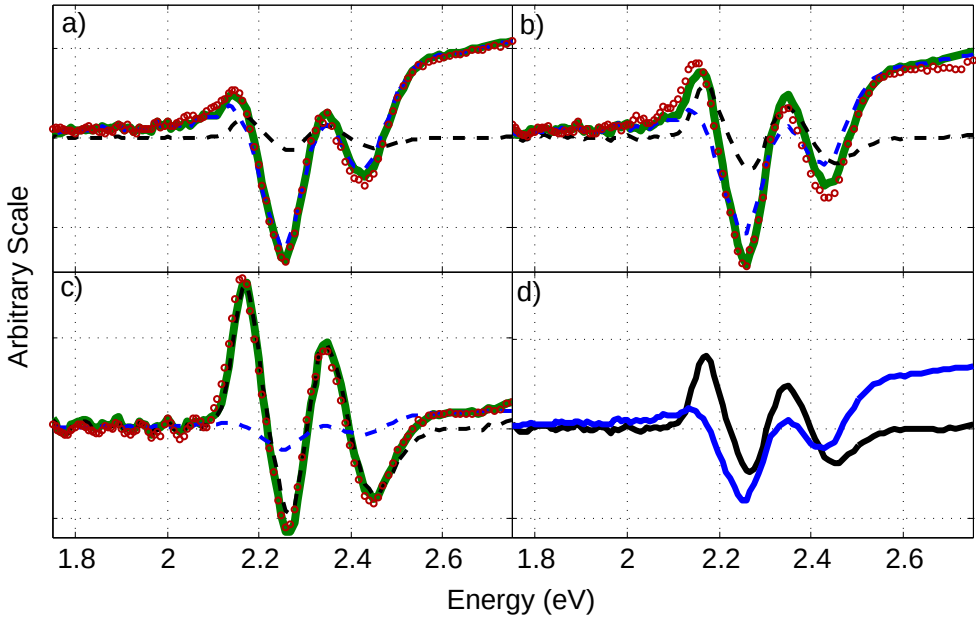

Figure 2.10: Full frequency deconvolution of pump probe results on NiOEP. The transient absorption data (red ∘) are fit with a weighted 50 fs (π,π*) trace (black) and a 50 ps (d_{z^2},$d_{x^2-y^2}$) state (blue) with the optimization shown in green. a) is 200 fs, b) is 500 fs, c) is 5 ps, and d) represents the spectral shapes, blue and black, assigned to the (π,π*) and (d_{z^2},$d_{x^2-y^2}$), respectively.

Molecule	τ_{S_1} (ps)	Γ	τ_D (ps)
NiTMP	0.41 ± 0.14	0.62 ± 0.13	230 ± 40
NiOEP	2.2 ± 0.16	1.0 ± 0.15	270 ± 50
NiOEP°	1.94 ± 0.4	0.69 ± 0.12	260 ± 60

Table 2.2: Time resolved dynamics for NiTMP and NiOEP. The bottom NiOEP° represents the fit parameters for the full frequency deconvoluted spectra in Figure 2.11. τ_{S_1} is the lifetime of S_1 through formation of the localized (d_z^2,$d_(x^2-y^2)$) and τ_D is loss of (d_z^2,$d_(x^2-y^2)$) and formation of the ground state. Γ represents the stretching parameter in the stretched exponential fit. All errors were reported at the 68.2 % confidence interval.

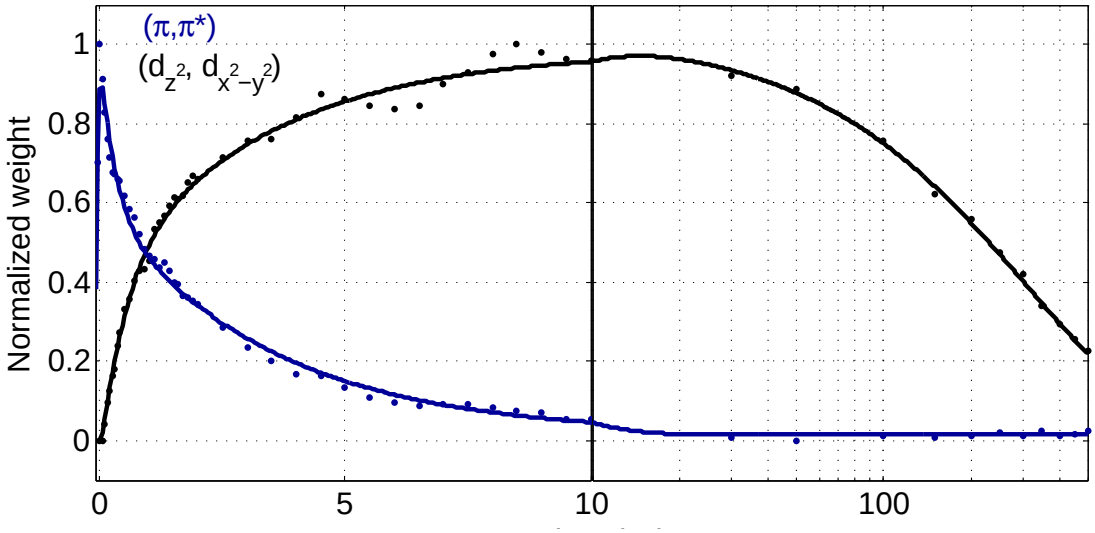

Figure 2.11: Decay of the (π,π*) state (blue) and growth of the (d_{z^2},$d_{x^2-y^2}$) (black) state from the weight parameters in the full frequency deconvolution plot in Figure 2.10. Weight parameters have been fit with a stretched exponential (solid line).

to previous measurements on NiTMP.[5] Those experiments also revealed a negative feature assigned to $S_1 \rightarrow S_0$ stimulated emission in Q band excitation. However, time integrated measurements showed a 20 nm disparity between the declared stimulated emission and $S_1 \rightarrow S_0$ fluorescence. The negative feature was also only present around time zero in previous results and those shown here, a phenomenon observed in several other porphyrins that is inconsistent the the singlet lifetime and emission energy.

Formation of the $^3(d_{z^2},d_{x^2-y^2})$ state occured with time constants of 0.41 and 2.2 ps in NiTMP and NiOEP, respectively. There was no spectral evidence for intermediates in the transition from the ruffled to planar form ($^1(\pi,\pi^*) \rightarrow {}^3(d_{z^2},d_{x^2-y^2})$) in NiOEP and NiTMP. The presence of the intermediate $^1(d_{z^2},d_{x^2-y^2})$ may not clearly manifest itself in the transient absorption spectra. A stretched exponential fit of the $^1(\pi,\pi^*)$ decay and $^3(d_{z^2},d_{x^2-y^2})$ growth indicates the rate of transfer is lowered by vibrational relaxation of $^1(\pi,\pi^*)$ during the interconversion process. Loss of the $^3(d_{z^2},d_{x^2-y^2})$ state results in repopulation of the ground state in approximately 200 ps, consistent with previous measurements.[74;5]

Chapter 3

Femtosecond and Picosecond Singlet Lifetimes in Platinum and Palladium Octaethyl Porphyrin Solutions and Films

3.1 Introduction

Platinum and palladium porphyrins have been shown as useful materials for OLED and OPV devices.[48;50;91;92;93;94;95] These planar porphyrins have the ability to form strong molecular arrays with efficient energy conversion and charge transport processes useful for artificial photosynthesis.[96;97;98;72] While exciton transport remains poor, platinum

and palladium porphyrins have a long triplet lifetime of ∼100 μs and ∼1.5 ms, respectively,[99] which can be useful for transporting excitons over a long distance. A common comparison to "the tortoise and the hare" resides with these types of materials in determining whether a singlet materials with a short lifetime and an efficient transfer rate is better than triplet materials with a much longer lifetime but poor transfer rate.

Platinum porphyrins show further promise as exciton diffusion lengths have been measured to be 18 nm through photoluminescent measurements[48] and 30 nm in power conversion efficiency studies.[100] While the long diffusion length shows promise for PtOEP in devices, the excited state dynamics are poorly understood. Measured reports of PtOEP singlet lifetimes in solution have been limited by time resolution, reporting between 9 ps and 13 ps singlet lifetimes[101] but further clarified in films to be 160 fs.[102] Other reports have estimated a very short singlet lifetime and measured long time excited state dynamics of platinum porphyrins including time integrated phosphorescence.[103;104;105;106;107;108;109;99;79] No measurements of stimulated emission have been reported on thin films of PtOEP, likely due to the need for optically clear and uniform samples, low excitation densities needed to prevent exciton annihilation, and inability to overcome low signal to noise with high time resolution.

Palladium porphyrins have been employed as oxygen sensers[110;111;112;113], thin film dopants[114] and as sensitizing molecules[115;116;95;117;104;118;61]. The singlet lifetime of a PQ_4Pd palladium porphyrin sensitizer has been reported between 10 ps and 20 ps through ultrafast measurements and observation of triplet annihilation.[115] The 10-20 ps

singlet lifetime is consistent with the heavy atom effect as more spin orbit coupling from the platinum atom should cause shorter singlet lifetimes than the palladium atom.[119] Because of the excited state properties of PdOEP including a long triplet lifetime[99] and picosecond singlet lifetime, it shows promise as a potential OPV material.

An important factor in implementation of palladium and platinum porphyrins in devices is the change in the excited state dynamics when changing from isolated chromophores in solutions to tightly packed π-stacked neat films. Studies have shown the presence of external heavy atoms increase the spin orbit coupling and intersystem crossing of molecules.[120;26;121] Devices incorporating palladium and platinum porphryins rely on the intramolecular and intermolecular excited state behavior of the molecules in all environments and understanding the dynamics is crucial to improving device performance.

3.2 Experimental Procedure

3.2.1 Materials

Palladium octaethyl porphyrin (PdOEP) and platinum octaethyl porphyrin (PtOEP), shown in Figure 3.1, were purchased from Sigma Aldrich and used as delivered with no further purifications. The porphyrins were dissolved in 40 mL of tetrahydrofuran (THF) at a concentration of 150 μM. Chloroform and toluene were also used as solvents and all showed qualitative agreement. Thin films of PdOEP and PtOEP were made

using a vapor deposition technique. The solid material to be sublimated was placed in a container and a current was applied to the container to reach the sublimation temperature. Vaporized particles were dispersed in the vacuum chamber and deposited on a quartz substrate at a rate of 0.2 $\AA$/sec until a thickness of 60 nm was reached. Mixed films of 4,4-bis(N-carbazolyl)biphenyl (CBP) and porphyrin were co-deposited at a 10% porphyrin ratio by weight to a thickness of 60 nm.

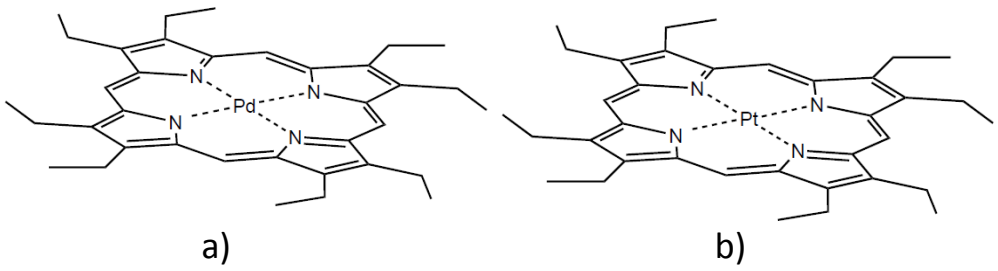

Figure 3.1: Molecular structure of a) PdOEP, and b) PtOEP.

3.2.2 Steady State Absorption and Emission

Absorption measurements of PdOEP and PtOEP were obtained using the Cary-14 spectrometer previously described. A 1 mm path length quartz cuvette was used for solutions of PtOEP and PdOEP with solvent absorption background subtracted off.

Time integrated emission measurements were performed using a Fluorolog 1680 0.2 mm double grating spectrometer with a Xenon lamp source and photomultiplier tube

for detection. Solutions were purged with nitrogen in a 1 cm cell for 5 min before measurement. Thin films were placed in the sample holder which was purged with nitrogen with front face geometry employed on all measurements. Fluorescence was measured through excitation into the Soret band for each sample. Excitation into the Q band detected too much scatter to resolve the small Stokes' shifts in samples where fluorescence was detected.

3.2.3 Time Resolved Measurements

Ultrafast measurements on PtOEP and PdOEP thin films and solutions were performed on the aforementioned laser system. Briefly, a 1.05 W, 1 kHz, 1.55 eV pulse train exiting the regen was compressed to 110 fs with a 1200 g/mm Richardson grating pair, resulting in a 700 mW output. For Q band excitation, 60% of the light was diverted, using a beamsplitter, into a non-collinear optical parametric amplifier (NOPA). 380 mW of 1.55 eV light was converted to 300 μW of 2.27 eV excitation light and compressed to 85 fs using a pair of SF 10 prisms. The pump light was frequency modulated to 500 Hz using a beam chopper and focused down to a 96 μm diameter spot size using a 5 cm parabolic mirror.

Excitation into the B band excluded use of the NOPA and the 1.55 eV pulses were compressed to 90 fs. The pulse train was frequency modulated to 500 Hz and sent through a BBO doubling crystal, generating 3.1 eV light. 3.1 eV excitation pulses were focused by a 5 cm parabolic mirror to a 118 μm diameter spot size at the sample.

A white light continuum probe for PdOEP and PtOEP sample measurements was created by focusing 1.55 eV light on a 2 mm fused silica window which which resulted in light between 3.0 eV and 1.37 eV. The probe was focused on the sample, collimated with a 5 cm lens, refocused with a 10 cm lens into an Action Spectra Pro 2150i, 0.150 m imaging dual grating monochrometer and dispersed onto a Hamamatsu diode array to collect full frequency spectra.

Solutions of PdOEP and PtOEP were continuously replenished using a Cole Parmer mechanical pump which flowed the sample at a rate around 1 mL/s. PtOEP and PdOEP thin films were rotated at a rate of 5 rotations per second under the presence of nitrogen in a sealed box to prevent any quenching of the excited states through interactions with molecular oxygen.

Pump intensities can cause intermolecular effects in thin films such as exciton annihilation, which will be discussed in Chapter 4. The loss of signal due to annihilation could be spectrally convoluted with intersystem crossing (ISC) and cause overestimation of the ISC rate. To get accurate measurements of the ISC rate, the pump intensities were kept low enough to prevent intermolecular interactions under both Q and B band excitations.

3.3 Results and Discussion

3.3.1 Absorption and emission of PdOEP and PtOEP

The absorption and emission measurements performed on PdOEP and PtOEP are shown in Figure 3.2 and consistent with previous results.[122;107;108;123;124;125] A Q(0,0) band consisting of doubly degenerate Q_1 and Q_2 bands is located around 2.27 eV and 2.31 eV for PdOEP and PtOEP, respectively. A weak 2.47 eV Q' band, Q(1,0), corresponds to a vibronic transition from $S_0 \rightarrow S_1$ vibrationally coupled to a $S_0 \rightarrow S_2$ transition.[104] Aggregation is not present in these solutions as it would spectrally manifest itself with red-shifting and splitting of the Soret band as well as further splitting of the Q_1 and Q_2 bands as presented in Figure 3.3.[126;127]

Photoluminescence spectra were measured through excitation of the Q(0,0) band at varying energies corresponding to the absorption maximum. Both fluorescence and phosphorescence are observed for PdOEP solution and neat film and shown in Figure 3.2a. PdOEP in THF reveals fluorescence at 2.24 eV, a Stokes' shift of 0.03 eV and phosphorescence at 1.87 eV. The Stokes' shift is also small when changing from solution to film, as fluorescence in PdOEP neat film is seen at 2.16 PtOEP, a shift of 0.5 eV. A small phosphorescence peak in PdOEP 60 nm neat film is observed at 1.85 eV. Fluorescence was not detected in 10% PdOEP:CBP as the spectral range between 2.0 eV and 2.2 eV was dominated by noise and fluorescence from the quartz substrate while phosphorescence was detected at 1.86 eV.

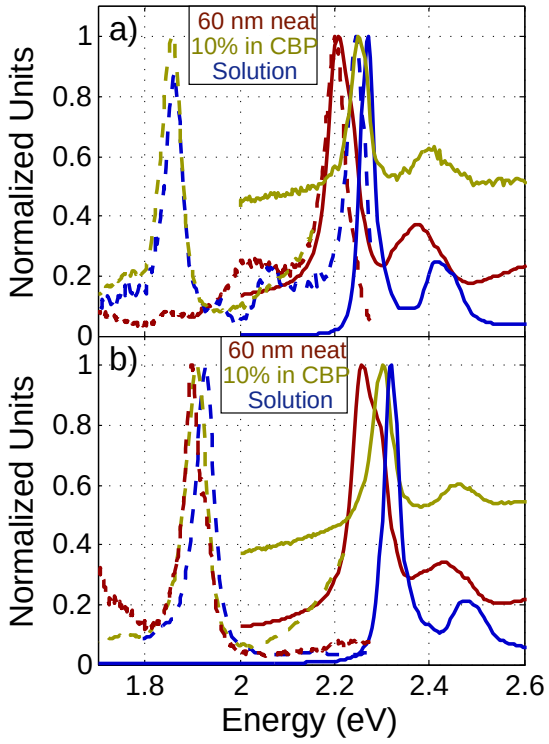

Figure 3.2: Absorption (—) and emission (- - -) spectra of a) PdOEP and b) PtOEP. Porphyrins in THF solvent are blue, 60 nm 10% porphyrin:CBP films are gold, and 60 nm neat porphyrin films are red. Rise in the emission spectra of 10% films between 2.0 eV and 2.2 eV was dominated by ambient noise and emission from the quartz substrate. Small Stokes' shifts were observed for PdOEP in THF and PdOEP 60 nm film.

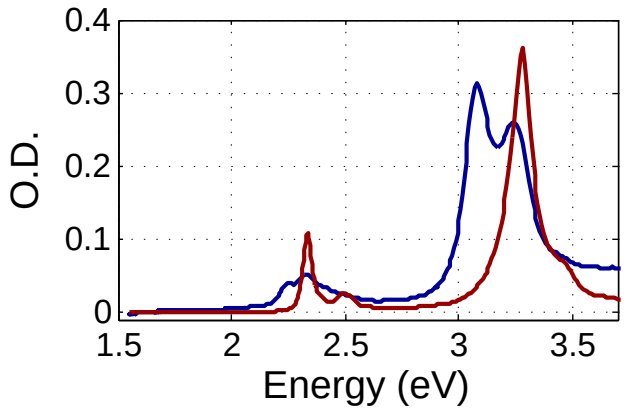

Figure 3.3: Comparison between PtOEP absorption in toluene (red) and an aggregated sample of PtOEP in toluene (blue). Aggregation occurred due to unknown issues with sample preparation at a slightly higher concentration.

PtOEP in THF, 10% PtOEP:CBP, and neat PtOEP 60 nm film reveals phosphorescence around 1.93 eV, 1.91 eV, and 1.90 eV in Figure 3.2b, consistent with previous measurements.[103;110] PtOEP is a known phosphor but no $S_1 \rightarrow S_0$ fluorescence has been observed in literature or present here in solution or film. Sub-200 fs intersystem crossing minimizes the quantum yield of fluorescence complicating detection through time integrated spectroscopic means.[102]

3.3.2 Excited State Dynamics in Octaethyl Porphyrins

Previous reports on nickel porphyrins observed differing dynamics upon excitation to S_1 and S_2[74;5] and similar excited state behavior may occur in platinum porphyrins. Figure 3.4 shows the pump probe spectra of PtOEP in chloroform under S_1 (Q band) excitation and under S_2 (B band) excitation. Both figures reveal a ground state hole and 2.31 eV and a broad excited state absorption between 2.45 and 2.8 eV. The transient absorption lives longer than the measured 500 ps with no apparent changes in the dynamics due to excitation energy. It is likely that upon excitation to S_2, there is rapid internal conversion $S_2 \rightarrow S_1$ within the 90 fs time resolution. Porphyrin samples in chloroform, THF, and toluene all show similar dynamics in solution.

Investigation of the excited state dynamics of PdOEP is presented in Figure 3.5 and Figure 3.6. The S_1 ground state hole is observed in Figure 3.5 at 2.27 eV, 2.20 eV, and 2.21 eV in panels a, b, and c, respectively. Broad excited state absorption in lies between 1.8 eV and 2.75 eV is attributed to absorption from the initially created singlet

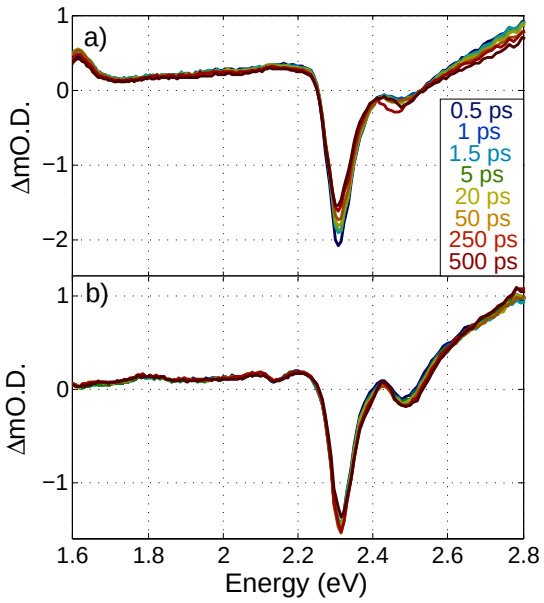

Figure 3.4: Full frequency spectra of PtOEP in chloroform, under a) S_1 excitation (2.31 eV) and b) S_2 excitation (3.06 eV). Excited state dynamics reveal very similar behavior regardless of excitation.

state ($S_1 \rightarrow S_n$) and is further explored in Figure 3.6. The transient absorption decays with a time constant of (8.5 ± 3.2) ps in THF indicating loss of the initially created S_1 state. As we transition from solution to dilute 10% wt PdOEP:CBP 60 nm films, the porphyrins lie nearer to each other in the amorphous films and the singlet lifetime decreases to (8.2 ± 3) ps. In the 60 nm PdOEP neat film, the π-stacking arrangement situates palladium porphyrins adjacent to each other, resulting in a singlet lifetime of (7.0 ± 4.2) ps.

A negative feature is observed at 2.07 eV for PdOEP in THF, 2.01 eV for 10% wt PdOEP:CBP, and 2.0 eV for PdOEP neat film in Figure 3.6. The shape and energy of the negative feature is consistent with the vibronic emission peak Q(0,1) observed in Figure 3.2 and Franck-Condon fluorescence while the time resolved dynamics of the feature are correlated to loss of the transient absorption. The small Stokes' shift in the fluorescence likely means the large $S_1 \rightarrow S_0$ (Q(0,0)) stimulated emission feature may be convoluted in the $S_0 \rightarrow S_1$ (Q(0,0)) ground state hole. Convolution of these overlapped features may also explain the correlated gain in the ground state hole as a disappearance of stimulated emission rather than any ground state recovery.

Disappearance of S_1 stimulated emission and correlated loss of transient absorption on the order of 10 ps is consistent with intersystem crossing.[115] The results also show the first ultrafast measurement of stimulated emission in PdOEP. The rate of intersystem crossing in PdOEP also increases in the presence of other external PdOEP molecules and is displayed in Table 3.3.2.

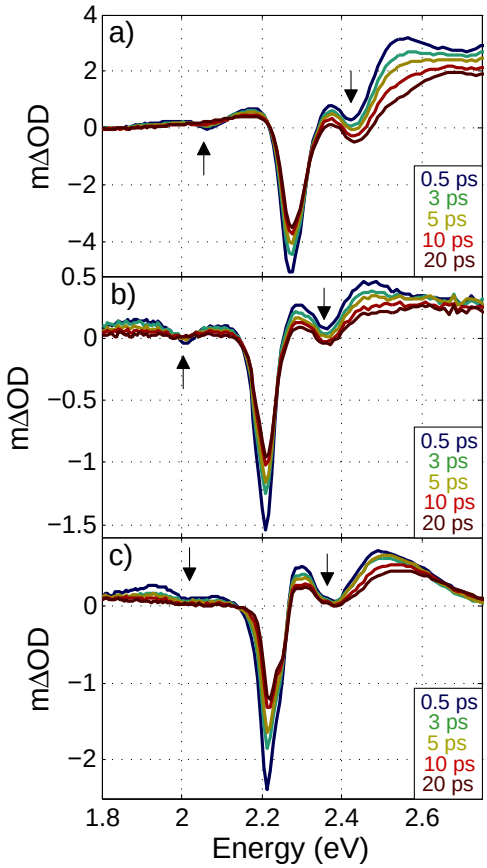

Figure 3.5: Full frequency pump-probe spectra of a) PdOEP in THF and b) 10% wt PdOEP:CBP film and c)PdOEP 60 nm neat film.

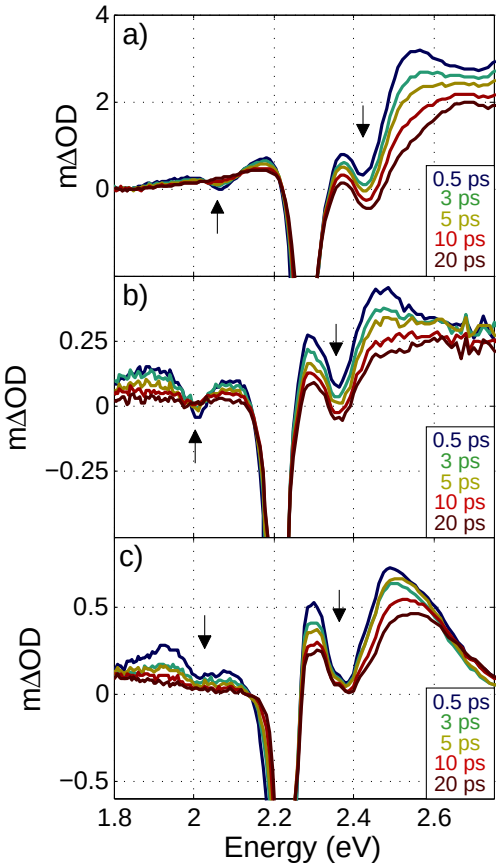

Figure 3.6: Full frequency pump-probe spectra of a) PdOEP in THF and b) 10% wt PdOEP:CBP film and c)PdOEP 60 nm neat film, magnified to show transient absorption dynamics.

The singlet lifetime of PtOEP in solution, dilute film, and neat film has also been measured and is shown in Figure 3.7. PtOEP in THF shows a the $S_0 \rightarrow S_1$ ground state hole centered at 2.31 eV for PtOEP in THF, 2.29 eV for 10% PtOEP:CBP, and 2.25 eV for PtOEP neat film. A broad transient absorption spans 1.8 eV to 2.75 eV in Figure 3.8 and decays slightly over the first few hundred femtoseconds with a time constant of (0.21 $\pm$ 0.17) ps for PtOEP in THF, (0.14 $\pm$ 0.12) ps for 10% PtOEP:CBP, and (0.16 $\pm$ 0.1) ps for PtOEP neat film. This transient decay is similar to that observed in PdOEP and attributed to intersystem crossing. Given the instrument response of our experiment and the uncertainty of the singlet lifetimes, it is difficult to ascertain the external heavy atom effect between films and solution.

Stimulated emission is observed for PtOEP in solution and amorphous films. The shape of the stimulated emission closely resembles the Q(1,0) absorption band for each sample and is likely the Q(0,1) emission. Similar to PdOEP, the short-lived Q(0,0) emission may be convoluted with the ground state hole since loss of the ground state hole feature is observed as $S_1 \rightarrow T_1$. The sub-200 fs singlet lifetime also explains the lack of fluorescence detected through time integrated measurements. These ultrafast results are the first known detection of stimulated emission from $S_1 \rightarrow S_0$ in platinum porphyrins.

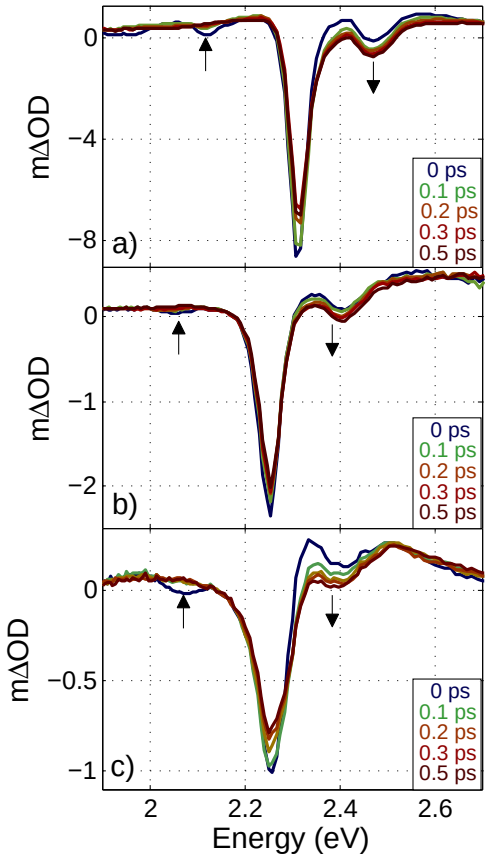

Figure 3.7: Full frequency pump-probe spectra of a) PtOEP in THF and b) 10% wt PtOEP:CBP film and c) PtOEP 60 nm neat film.

Molecule	τ_{ISC} (ps)
PdOEP in THF	8.5 ± 3.2
10% PdOEP:CBP 60 nm film	8.2 ± 3.0
PdOEP 60 nm film	7.0 ± 4.2
PtOEP in THF	0.21 ± 0.17
10% PtOEP:CBP 60 nm film	0.14 ± 0.12
PtOEP 60 nm film	0.16 ± 0.13

Table 3.1: Fitting parameters for excited state decays of PdOEP and PtOEP solutions and films. All τ values represent the singlet lifetime and are reported in ps with weights using a normalized scale. Errors were determined using the 68.2% confidence interval.

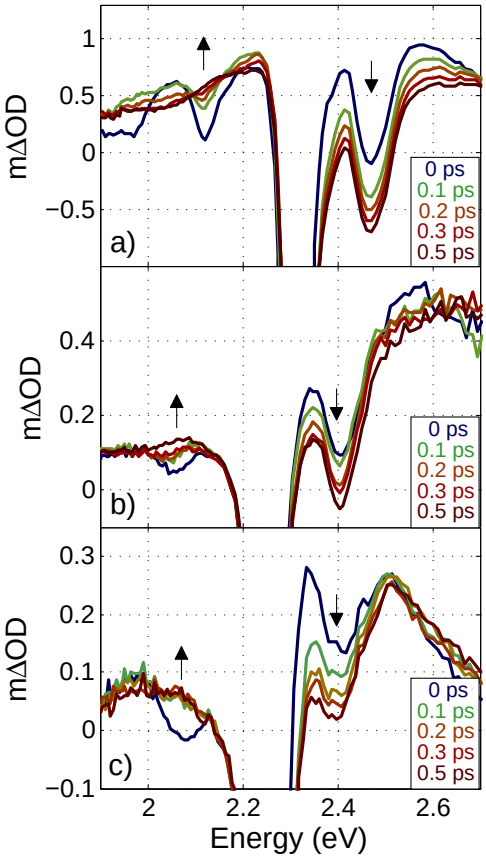

Figure 3.8: Full frequency pump-probe spectra of a) PtOEP in THF and b) 10% wt PtOEP:CBP film and c) PtOEP 60 nm neat film magnified to show transient absorption.

3.4 Conclusions

The presented results show the first ultrafast detection of stimulated emission in PdOEP and PtOEP. Due to the rapid intersystem crossing in PtOEP, the stimulated emission detected is the first reported observation of $S_1 \rightarrow S_0$ fluorescence. Experimental measurements on the increase of intersystem crossing rate from palladium porphyrin to platinum porphyrin follows the expected spin-orbit coupling trend.[121;26;120] The presence of external heavy atoms increases the spin-orbit coupling and subsequent intersystem crossing rate when comparing metalloporphyrin isolation in solutions to π-stacked amorphous films. Devices incorporating palladium and platinum porphyrins rely on excited singlet and triplet state behavior to increase device performance. The 7-8 ps singlet lifetime and 1.5 ms triplet lifetime[99] of PdOEP could be more useful in OPVs than PtOEP by utilizing both singlet Förster and triplet Dexter transfer which will be further explored in Chapter 4.

Chapter 4

Excited State Dynamics of Triplet Fusion in PtOEP Thin Films

4.1 Introduction

Organic photovoltaics (OPVs) have come under significant study due to their increasing efficiencies and their potential as a low cost, mass produced renewable energy resource.[46;18;128;47;129;130;131;17;132;133] Platinum porphyrins remain among the most successful triplet sensitizers utilized in OPVs, opto-electronics and excited state upconversion.[134;135;136;137;138] The long excited triplet lifetime (95 μs)[139] aids the exciton diffusion process, leading to long reported diffusion lengths.[48;140] However, the extended lifetime facilitates a triplet-triplet annihilation (TTA) process that limits the efficiency of OPVs

and OLED devices.[141;142] Investigation of the triplet-triplet annihilation process is essential for improving OPV and OLED device performance.

Annihilation, upconversion, and fusion of excited states have been explored in the literature.[137;138;114] The process of annihilation is typically considered to be a $2 \rightarrow 1$ excited state process in which energy is tranferred from one excited state to the other, but quickly relaxes down to the originating state as shown in Equation 4.1.

$$S_1 * + S_1 * \rightarrow S_n * + S_0 \rightarrow S_1 * + S_0 \tag{4.1}$$

Fusion represents a unique type of annihilation process where the intermediate excited state exist long enough to be transferred to adjacent or attached molecules.[137;138;114] PtOEP molecules have exhibited annihilation of the triplet excited states that resulted in the upconverted fluorescence of PF26, an adjacent polymer.[137;138] Similarly, PdOEP films have shown upconversion of excited states using an attached copolymer and observation of singlet emission of the polymer.[114] While these studies illustrate annihilation in PtOEP and PdOEP, they only observe the result of annihilation and lack information about intermediate states or excited state dynamics that may be integral in the process.

Here we present the triplet-triplet fusion process in PtOEP through a previously unreported mechanism. Interaction of two triplet excitons leads to formation of a higher energetic exciton located on the $d_{(x^2-y^2)}$ orbital of the platinum atom and one ground state. The resulting excited exciton has an extended lifetime and shows potential for long-lived energy storage in optically inacessible states which could be utilized in OPV

devices.

4.2 Experimental Procedure

4.2.1 Thin Film Processing

Platinum (II) octaethyl porphine (PtOEP) was purchased from Frontier Scientific, used as is with no further purifications. PtOEP thin films were vapor deposited using thermal deposition under high vacuum (10^{-7} torr) at a rate of 0.2 nm/sec on a 3.8 cm diameter, 0.16 cm thick quartz substrate, grown to a film thickness of 60 nm. Ellipsometric techniques were used to determine actual film thickness.

4.2.2 Steady State Absorption and Emission

Absorption and emission measurements were performed on the Cary 14 absorption spectrometer using OLIS Globalworks software. The aforementioned quartz substrate was used for background subtraction on all absorption collections. Fluorescence measurements were taken using the Fluorolog double grating monochrometer with slit width set at 1 mm. 3.31 eV excitation light was incident on the 60 nm PtOEP film which was sealed in a nitrogen environment to reduce triplet state quenching with singlet oxygen.

4.2.3 Pump Probe Spectroscopy on Solid State Materials

Pump-probe measurements were performed using a home-built Ti:sapphire laser system described in the experimental sections. Briefly, a 200 mW, 86 MHz pulse train

was created through a mode locked oscillator pumped at 2.7 W from a CW Nd:YVO_4 Spectra Physics Millenia Pro laser. Pulses were amplified at 1 kHz with a home-built regenerative amplifier pumped by a Q-switched Nd:YAG Spectra Physics Empower 15. The 810 nm pulses were compressed to 80 fs at an energy of 350 μJ. Frequency doubling of the 1.55 eV pulses using a 1 mm BBO crystal resulted in 3.1 eV pulses which were frequency modulated to 500 Hz and rotated to the magic angle (54.7 degrees) relative to P-polarization.

A white light continuum probe (1.35 eV - 2.76 eV) was generated by focusing 1.55 eV pulses into 2 mm thick sapphire with P-polarization. Pump and probe beams were directed towards the sample with a 5 cm parabolic mirror at an angle of 22.6 degrees between beams and focused to a spot size of 107 μm ($1/e^2$) as measured with a 1 μm pinhole. PtOEP films were situated at the focus and rotated at a speed of 5 revolutions per second at a distance of 1.3 cm from the center, resulting in a traveling velocity of approximately 40 cm/s. The rotating film was contained in a 5" x 5" x 5" box purged with high purity nitrogen gas to prevent photobleaching and singlet oxygen quenching. The continuum probe was collected with a a 256 pixel diode array (Hamamatsu) after incident dispersion from a 150 g/mm grating blazed at 2.48 eV. Residual 1.55 eV light was absorbed by a 0.2 mM 1,1'-diethyl-4,4' dicarbocyanine iodide (Sigma Aldrich) in a 1 mm path length cuvette.

Dilute film measurements were performed with a similar setup but small changes in the focal parameters. The 3.1 eV excitation beam waist at the sample was 122 μm

($1/e^2$), again measured by the 1 μm pinhole. All pump fluences were held constant with experiments performed back to back to limit long time fluctuation of the laser, room conditions and thin film exposure to the environment.

Power dependent traces were measured by detecting the transmitted probe with a Thorlabs DET210 photodiode fitted with 2.58 eV, 2.27 eV, and 2.21 eV (FWHM 10 nm, Thorlabs) interference filters using Lock-in detection (SRS-810) at the modulation frequency of the pump (500 Hz). The reported pump laser fluences were measured concurrently with the pump-probe signals by splitting off a small portion of excitation light before the sample and detecting it with a separate DET210 photodiode calibrated to the laser power incident on the sample using a Coherent LM-2-VIS silicon detector and Fieldmaster GS power meter. The pump power was continuously varied through the use of a half-wave plate and subsequent polarizer. The half-wave plate was slowly rotated while the pump-probe and incident power were simultaneously measured. Incident power was converted to fluence using the experimental geometry described above.

The time dependent measurements were collected under the same conditions as the power dependent measurements. Pump-probe signal was measured at 2.58 eV using the same DET210 photodiode and interference filter and time delays ranging from -5 ps to 500 ps. Laser fluences were determined with the same equipment as the power dependent measurements and adjusted between the back to back scans.

The number of absorbed photons by the PtOEP thin film was determined through

measurement of the power before and after the sample, accounting for loss at interfaces using Snell's Law. Refraction indices for air (1.0003), PtOEP (2.15), and quartz (1.47) were used to determine the reflective loss of the 400 nm excitation light, which was incident on the PtOEP interface at an angle of 11.3 degrees from normal. The measured transmitted and reflected losses were subtracted from the incident power to determine the number of photons absorbed by the PtOEP. The initial exciton density was calculated given the spot size, film thickness, and photons absorbed assuming each photon absorbed creates one excited state.

4.3 Results and Discussion

4.3.1 Absorption and Emission Measurements

Steady state absorption and emission measurements are presented in Figure 4.1. The Soret and Q absorption bands originate from transitions previously described.[33;143] The Q band absorption has been scaled by a multiplicative factor as indicated in Figure 4.1.

4.3.2 Spectral Signature of Triplet-Triplet Fusion in PtOEP neat films

Time and frequency resolved pump-probe experiments were collected on neat 60 nm PtOEP films and are presented in Figure 4.2. Optical excitations into the Q band (Figure 4.2b) and B band (Figure 4.2c) yield similar excited state dynamics indicating excited singlets internally convert from S_2 to S_1 within our 80 fs time resolution. Subsequent singlets in S_1 have been shown to undergo 160 fs intersystem crossing[102] leading

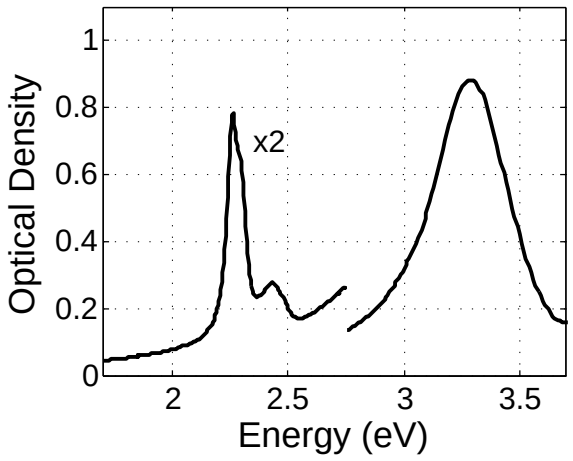

Figure 4.1: Absorption of a PtOEP 60 nm neat film. Optical density of the Q band absorption has been scaled x2.

to near instantaneously optically excited $^3(\pi,\pi^*)$ A ground state bleach is located at 2.27 eV and consistent with missing Q band absorption. Broad transient absorption between 2.75 eV and 1.7 eV is assigned to excited state triplet absorption.

Figure 4.2a and 4.2b represent Q band excitation at low (1.2 x 10^{14} ph/cm^2), and high (1.4 x 10^{15} ph/cm^2) laser fluences. At low fluences, there is minimal change in the broad, featureless transient absorption correlated with small changes in the ground state hole. There was no evidence for significant loss of T_1 on the timescales of the experiment. At high fluences, there is clear evidence of loss of T_1 at 2.58 eV and correlated growth of a new species at 2.21 eV. B band excitation at high fluences (Figure 4.2c) yields similar loss of T_1 at 2.58 eV and transient growth at 2.21 eV. Two photon absorption has

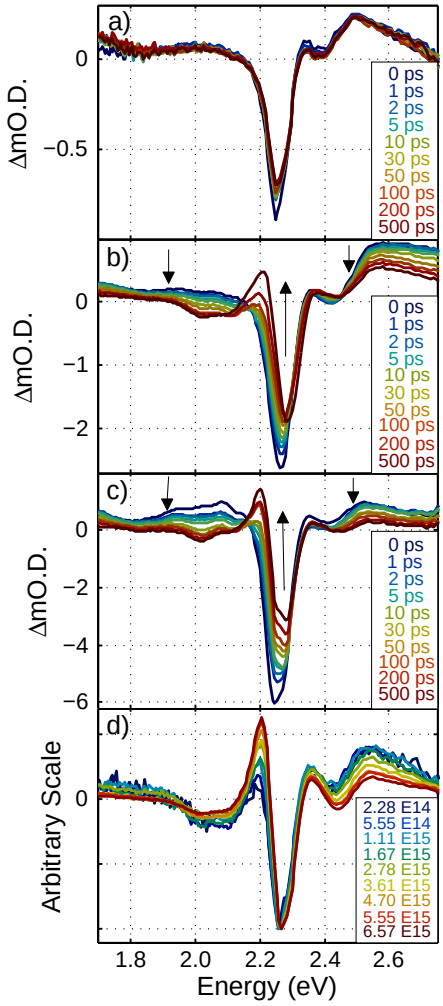

Figure 4.2: Full frequency results indicating the power dependence of the absorption growth at 2.21 eV. No transient growth is observed when excited to S_1 at low fluences in panel a). As the fluence increases, panel b), growth at 2.21 eV is observed. The transient absorption at 2.21 eV is also observed at high fluences and excitation into S_2 in panel c), consistent with rapid internal conversion to S_1 and similar resulting dynamics. Panel d) reveals the power dependence of the transient growth upon excitation to S_2, normalized to to the ground state hole.

been ruled out as it is not observed under similar experimental conditions and shown in Figure 3.7.

A direct comparison between the spectral shape and fluence is shown in Figure 4.2d. When normalized to the 2.25 eV ground state hole at a constant delay of 500 ps, the amount of 2.21 eV transient absorption increases with laser fluence. Formation of the new species is dependent on the exciton density and the corresponding derivative-like spectra looks similar to spectra in nickel porphyrins.[86;74;5;81;85]

In nickel porphyrins, excited singlets transfer from the initially excited ring $\pi \rightarrow \pi^*$ to the energetically favorable $d_{(x^2-y^2)}$ orbital.[86;74;5;81;85] Localization of the excitation on the nickel atom perturbs ring conformation and red shifts ground state absorption,[73;88] leading to a pump-probe spectrum similar to that presented in Figure 4.2b and 4.2c. In the case of nickel porphyrins, transient absorption from the populated singlet decays with correlated growth of the red-shifted absorption at 2.18 eV of the perturbed molecule.

In PtOEP the $^3(\pi,\pi^*)$ is formed in 160 fs before any further dynamics are observed. There are a few energetic pathways out of $^3(\pi,\pi^*)$ which can account for spectral changes. Relaxation from $T_1 \rightarrow S_0$ has been shown to have a lifetime of 95 μs[139] and is unlikely to significantly contribute on our timescales. Back transfer from $S_1 \leftarrow T_1$ is unlikely given the (3/2)kt energy at room temperature cannot overcome the 0.3 eV offset between the singlet and triplet states. If we consider exciton interactions, we allow for population of higher lying excited states, including $d_{(x^2-y^2)}$, and can explain

similar spectral shapes between platinum and nickel porphyrins.

Excited state localization to the $d_{(x^2-y^2)}$ orbital in PtOEP is achievable through triplet-triplet fusion, $T_1 + T_1 \rightarrow T_n + S_0$ or $T_1 + T_1 \rightarrow S_n + S_0$, where T_n and S_n represent potentially short-lived intermediates. Following annihilation, spin statistics designate a 3:1 ratio between triplets and singlets.[67;134] Singlet states near the resultant triplet fusion excitonic energy (3.8 eV) are the S_2 (2.9 eV) and the S_3 (3.8 eV). If the S_2 was a short-lived intermediate in the fusion process, it would likely result in rapid localization to the $d_{(x^2-y^2)}$ orbital upon direct excitation to S_2. However, in Figure 4.2d, population of the $d_{(x^2-y^2)}$ orbital decreases non-linearly as a function of laser power when compared to the ground state hole and is almost absent at the lowest fluence. Furthermore, we may expect population of the $d_{(x^2-y^2)}$ orbital and corresponding spectral signature in PtOEP solution measurements but it was not observed. The pump-probe result eliminates S_2 as an intermediate in the triplet fusion process as previously thought.[138] Onset of S_3 absorption is located at 3.8 eV which is energetically accessible through triplet fusion (3.8 eV) and could be a short-lived intermediate in the fusion process ($S_3 \rightarrow d_{(x^2-y^2)}$).

If a similar triplet and singlet manifold is assumed, an intermediate triplet state may also exist with energy around 3.8 eV. Like the excited singlet, the high lying excited triplet state subsequently undergoes rapid localization from $T_n \rightarrow d_{(x^2-y^2)}$, producing the derivative-like spectra at 2.21 eV in Figure 4.2b. The current pump-probe results show no evidence for either singlet or triplet intermediates so direct population of

$d_{(x^2-y^2)}$ through the fusion of two triplets is assumed. The diagram for the fusion process is shown in Figure 4.3 while further evidence for a bimolecular process is presented in Appendix A.3.

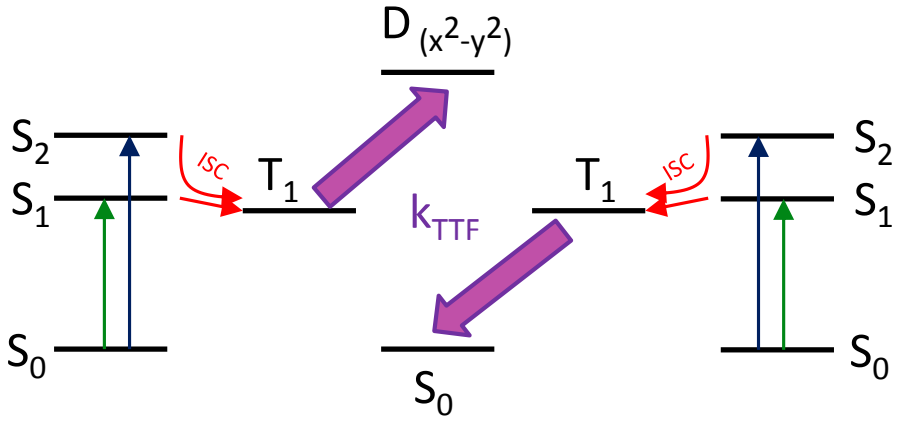

Figure 4.3: Schematic of the triplet fusion process. After excitation to S_1 or S_2, rapid intersystem crossing to T_1 is observed. The triplet excited state may transfer its energy to another triplet, populating S_0 and $d_{(x^2-y^2)}$ with a rate k_{TTF}.

Population of $d_{(x^2-y^2)}$ in nickel porphyrins has been shown as energy transfer (π,$\pi*$) $\rightarrow$ (d_{z^2},$d_{x^2-y^2}$).[84] The similarity of the spectral shape may lead to a similar thought for the PtOEP fusion process. However, the fusion process results in an exciton that is approximately 2 times the 1.9 eV triplet exciton energy. Theoretical calculations have shown that as the central porphyrin metal changes from nickel to palladium, the splitting of the unfilled $d_{(x^2-y^2)}$ orbital to the highest occupied d orbital increases from 1.3 eV to 3.8 eV.[86] It should be expected that a change from palladium to platinum

would further enhance the orbital splitting, meaning energy transfer of the short-lived 3.8 eV exciton would likely be forbidden. Population of $d_{(x^2-y^2)}$ through an intermediate would be an intramolecular charge transfer event.

The high energy exciton following triplet fusion lives longer than 11 ns as presented in Figure 4.4. Delayed fluorescence studies have already shown extraction of the energy through attachment of a large band gap emitter.[137;138] Large band gap molecules are not typically considered for OPVs since they do not absorb the solar spectrum though some may have desirable exciton transfer properties. Utilization of the long lived, upconverted energy and an efficient large band gap transport molecule may increase conversion efficiency in OPV devices.

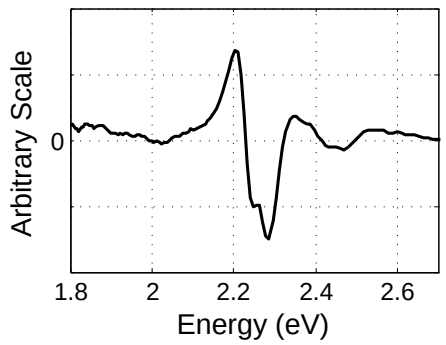

Figure 4.4: Pump-probe spectra of 60 nm PtOEP at 11 ns delay.

4.3.3 Triplet Fusion in PtOEP:CBP Films

Previous measurements have changed the exciton interactions by adjusting the laser fluence and subsequent exciton density in PtOEP neat films. By co-depositing a 4,4-bis(N-carbazolyl)biphenyl (CBP) molecule with PtOEP at varying concentrations, we can isolate the PtOEP molecules and physically limit the exciton interactions. The large band-gap and high energy LUMO in CBP is useful in preventing energy transfer and electron transfer from PtOEP to CBP, respectively.

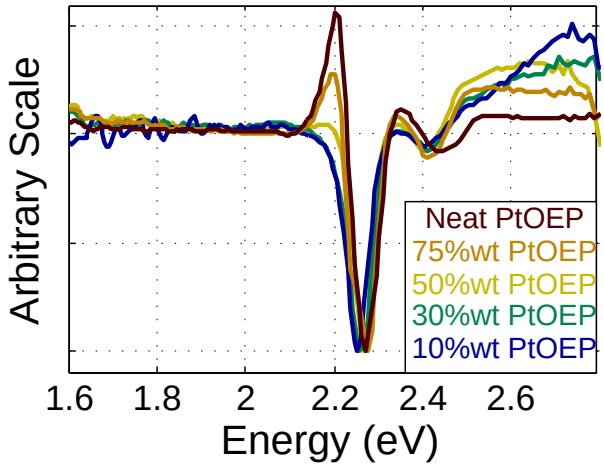

Figure 4.5: Pump-probe spectra of PtOEP diluted in CBP at varying concentrations at a 500 ps time delay. All traces have been normalized to the ground state hole at 2.25 eV at a laser fluence of 5.41 x 10^{15}.

Figure 4.5 shows the pump-probe results of a PtOEP neat film and varying PtOEP:CBP weight percentages with a constant laser fluence. The derivative-like spectra observed in

the neat film is consistent with previous measurements. Dilute films of PtOEP also show triplet fusion but is reduced by lowering the PtOEP concentration and non-existent at the 10% concentration by weight. The 10% weight PtOEP:CBP approximates to a 1:13.5 molecular ratio of PtOEP:CBP and given the 1.2 nm size of PtOEP and CBP, PtOEP molecules are separated by an average distance of about 2 nm. By physcally separating PtOEP molecules and thereby preventing any nearest neighbor interactions, the triplet fusion process has been turned off. The correlation between the loss of triplet fusion and lack of neighboring chromophores suggests that the short-range physical exchange mechanism is necessary for triplet fusion. A Förster mechanism is not physical since it would require a Förster radius to be less than 1 nm.

4.3.4 Time Dependent Application of Förster and Dexter Transfer Mechanisms

The presented experimental results revealed the first time dependent observation of the triplet fusion dynamics in PtOEP that had previously only been inferred through time integrated photoluminescent measurements.[137;138] It has been shown to be a bimolecular process through fitting with a second order kinetic model. Determination of the energy transfer mechanism of annihilation is crucial in reducing processes that limit OLEDs and can improve OPV device performance.

In order to fit the time dependent and power dependent traces, the equations that describe the rate of Förster and Dexter need to be described as a function of time.

Inokuti descriptively outlined the process of converting the distance dependent equations to time dependent equations for a donor surrounded by infinite acceptor molecules.[144] The derivation, which is shown in Appendix A.5 yields equation solved for the number of excited states, N, as a function of time, t, and initial concentration of excited states N_0 using a simple approximation published previously.[145] While solving for Equation 4.2, the equation is reduced to $g(\mathrm{kt})$ which must be numerically approximated in the time dependent fit. The Förster fit in equation 4.3 is solved analytically with no further approximations or numeric solutions.

$$N = \alpha \frac{N_0}{1 + \frac{N_0 \pi L^3}{6} g(kt)} \tag{4.2}$$

$$N = \alpha \frac{1}{1 + \frac{4\pi^{3/2}}{3} N_0 \sqrt{t}} \tag{4.3}$$

The time dependent and power dependent traces are fit with the Dexter parameters in equation 4.2 and are shown in Figure 4.6 and Figure 4.7. By adjusting the input of the x data from time to power in equation 4.2, both the power dependent and time dependent traces have global fitting parameters except for a single scalar for each trace. The results from the global optimization of the Dexter parameters can be seen in Table 4.1.

A few important variables listed in Table 4.1 are K and L. K is the pre-exponential constant in Equation 1.8 and gives an average value of 2.52 x $10^{-}1$ 1/ps. At the moment, the K value is only an adjustable parameter but is physically made up of the exchange

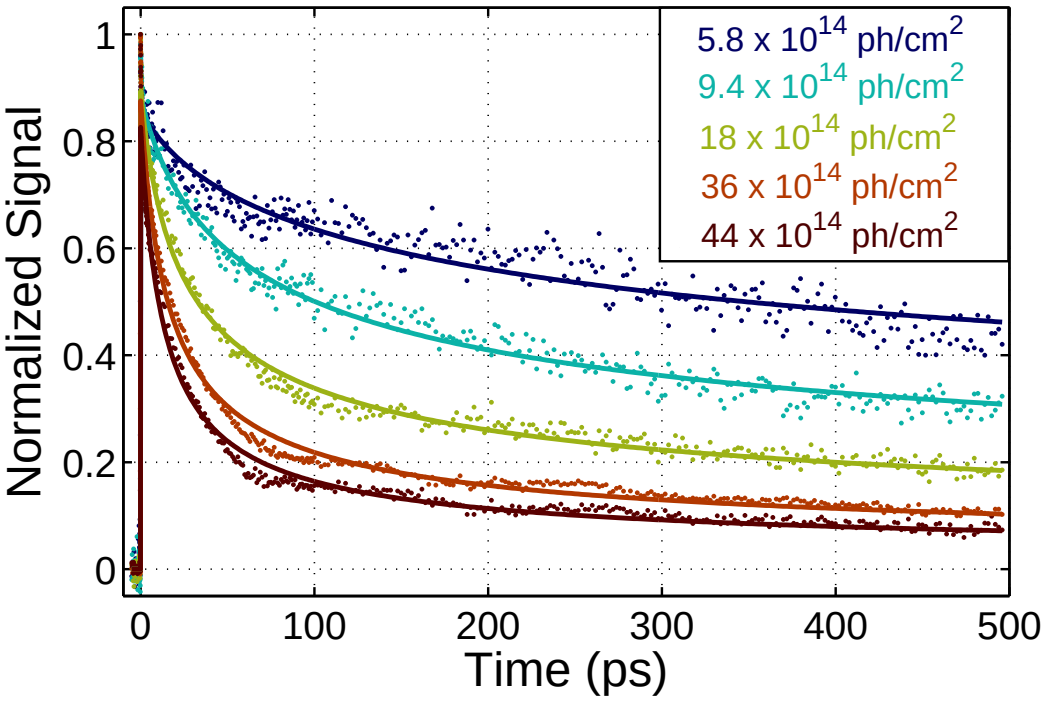

Figure 4.6: Time dependent decays of PtOEP at various fluences. The Dexter transfer fits from equation 4.2 are globally fit except for a scaling factor accounting for slight experimental fluctuations and any error in determining the initial laser fluence and exciton density.

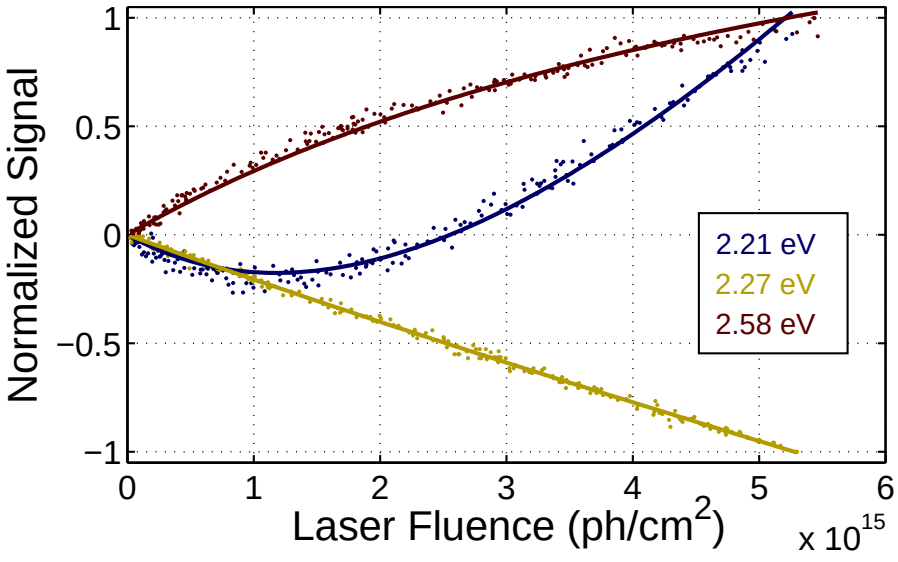

Figure 4.7: Global fitting to the power dependence of the pump-probe signals using equation 4.2.

interaction between molecules as well as the overlap integral (Equation 1.7). With more information about the overlap integral and exchange interaction, we could deconvolute K and compare to other results. The Dexter radius, L, returns an average value of 0.78 nm which is 0.65 of the 1.2 nm PtOEP diameter and consistent with a theoretical Dexter radius.[41]

Figure 4.8 compares the Dexter and Förster fits at a low and high fluence. At low fluence, both mechanisms fit fairly well as triplet fusion isn't as prevalent. However, at high exciton densities, Förster transfer significantly overestimates the amount of triplet fusion that occurs within 20 ps while underestimating the amount of fusion between 40 ps and 500 ps. The numerical results from Förster fits shown in Table 4.2 overestimate the

average Förster radius (14.9 nm) compared to the 1-10 nm radius typically considered.

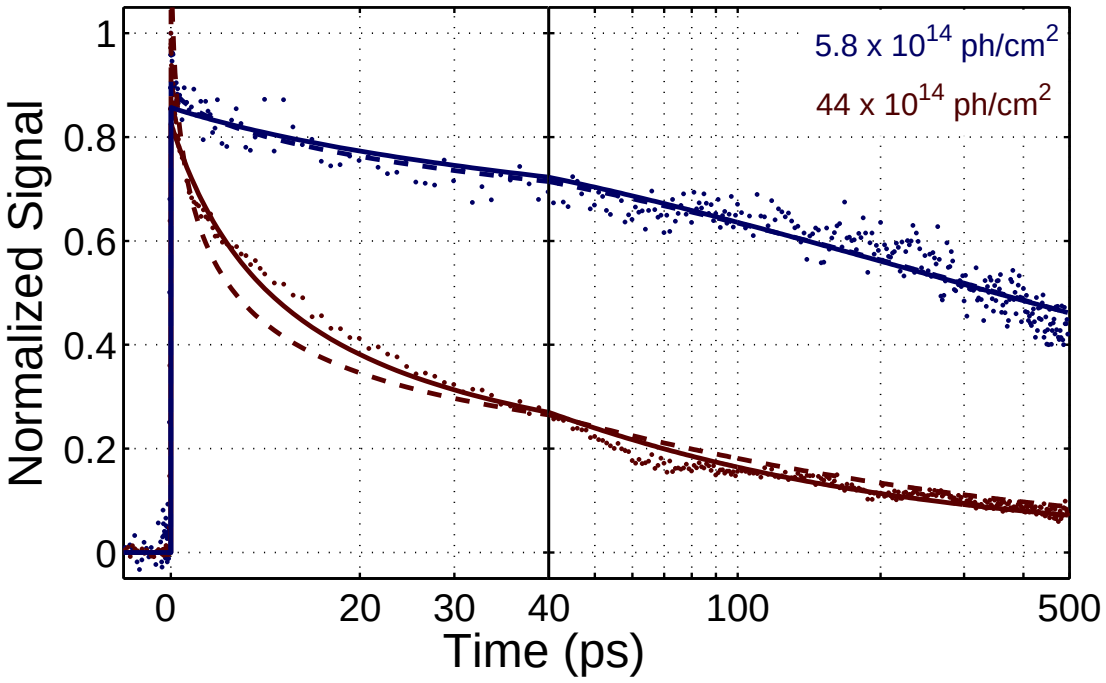

Figure 4.8: Time dependent comparison of the Förster (- - -) and Dexter (—) fits at low fluence (blue) and high fluence(red).

Fits presented in this section were done by Tom Pundsack on data collected by Jon Hinke.

4.3.5 Conclusion

The results reveal the first time-dependent observation of the triplet fusion process in PtOEP. This study also clarified the triplet fusion dynamics that former proposed

Fluence (ph/cm^2)	α	K (1/ps)	L (nm)
5.76 x 10^{14}	3.37 x 10^{-20}	2.49 x 10^{-1}	0.70
9.35 x 10^{14}	2.14 x 10^{-20}	2.63 x 10^{-1}	0.77
1.80 x 10^{15}	1.13 x 10^{-20}	3.55 x 10^{-1}	0.75
3.59 x 10^{15}	5.55 x 10^{-21}	2.28 x 10^{-1}	0.80
4.38 x 10^{15}	4.29 x 10^{-21}	1.66 x 10^{-1}	0.88

Table 4.1: Fitting parameters for the time dependent trace using the Dexter transfer equation 4.2

Fluence (ph/cm^2)	α	$R_0^3/\sqrt{\tau}$	R_0 (nm)
5.76 x 10^{14}	3.59 x 10^{-20}	2.32 x 10^{-22}	13.1
9.35 x 10^{14}	2.43 x 10^{-20}	3.22 x 10^{-22}	14.6
1.80 x 10^{15}	1.37 x 10^{-20}	3.66 x 10^{-22}	15.3
3.59 x 10^{15}	7.87 x 10^{-21}	3.73 x 10^{-22}	15.4
4.38 x 10^{15}	6.78 x 10^{-21}	4.35 x 10^{-22}	16.2

Table 4.2: Fitting parameters for the time dependent trace using the Förster transfer equation 4.3

mechanisms were unable to resolve.[137;138] Triplet fusion of two PtOEP triplets results in a long lived state localized on the $d_{(x^2-y^2)}$ orbital with a rate constant of k_{TTF} = (5.4 $\pm$ 0.4) x 10^{-10} cm^3 s^{-1}. Time dependent analysis of triplet fusion through the use of energy transfer mechanisms indicates the decay follows a Dexter transfer functional form rather than a Förster transfer form. Dexter transfer is typically considered an excited state and ground state interaction so further analysis would need to be performed to elucidate the excited state-excited state fusion as a Dexter process.

Chapter 5

Photoluminescent Quenching in Chlorine and Ferrocene Substituted Tin and Indium Tetraphenyl Porphyrins

5.1 Introduction

New research into emerging photovoltaics has directed analysis into photosynthetic model systems. Focus on the fundamentals of photoabsorption and electron transfer can lead to improvements in device efficiency through knowledge of the fundamental processes of photosynthesis.[68;146;67;66;147;148;149;71] Direct linkage between porphyrins and

ferrocenes[150] represent versatile molecules which exhibit multi-electron redox catalysis[151], information retention,[152] multi-porphyrin arrays,[153;66;147], energy and electron transfer,[154;155;156;157] and photoluminescent quenching.[158;69] Applications of these porphryins are dependent on the excited state dynamics including electron transfer and intermediate states only measureable by femtosecond pump probe systems. Current studies on ferrocene ligands axially bonded directly to porphyrin ring systems are limited to germanium porphyrins that have not been utilized for the redox and electron transfer applications.[3] Due to the vast applications of tin porphyrins and the unique structural properties, excited state dynamics must be elucidated to provide better insight into reactivity and device modeling.

Recent studies on the photoluminescence and ultrafast dynamics of trans-dichloro (5,10,15,20 - tetraphenylporphrinato) tin(IV) ($SnCl_2TPP$) and trans-bis (ferrocenecarboxylato) (5,10,15,20 - tetraphenylporphyrinato) tin(IV) ($Sn(FcCO_2)_2TPP$) revealed fluorescence quenching due to attachment of the $FcCO_2$ ligands while the singlet lifetimes remained relatively unperturbed.[69] After excitation to S_2, loss of the excited state is largely affected by intramolecular electron transfer to the (SnTPP)-($FcCO_2$) charge separated (CS) state ($\phi_{CS} = 0.4$). Non-radiative deactivation of S_1 did not occur through the CS state but rather through the proposed mechanism of enhanced ISC or IC due to the attached $FcCO_2$ groups.

Further exploration of tin porphyrins directly attached to ferrocene ligands revealed

similar PL quenching as an unexpected loss of the quantum yield was observed in trans-bisferrocene (5,10,15,20-tetraphenylporphyrinato) tin(IV) ($SnFc_2TPP$) when compared to $SnCl_2TPP$.[158] The presence of metal to ligand charge transfer (MLCT) bands provides deactivation pathways for the initially created (π,π^*) that may explain the disparity in the quantum yield. The previous results obtained by communicate the importance of ultrafast measurements to determine excited state intermediates and deactivation pathways.[69]

Indium porphyrins have been relatively unexplored in their usage in photovoltaics. These porphyrins exhibit strong bonding properties that are useful in biological functions with potential in molecular arrays.[159] Similar chlorophyll derivatives, indium phthalocyanines, have been utilized in guest-host systems in optically limiting devices.[160;161] Substitution of the axial ligand in the 5-coordinate indium phthalocyanine adjusts the excited state properties of these optically limiting molecules.[162] Photoluminescence, excited state lifetimes, and quantum yields have also been explored in indium phthalocyanines and show similar properties to tin porphyrins.[163] Optical band gap tuning through deposition and annealing in thin films have been studied[164] and, coupled with the photophysical properties, illustrate promise in electronic devices.

Tin porphyrins show useful photovoltaic properties that show potential in OPV's. Indium porphyrins may exhibit properties much like tin porphyrins and need to be explored. Investigation into the photophysical properties of tin and indium porphyrins through ultrafast spectroscopy are crucial for optimum implementation into devices.

Here we present the effect of ferrocene ligand substitution in Sn(IV)Cl_2TPP on the fluorescence quantum yield by probing the excited state dynamics of tin and indium porphyrins.

5.2 Experimental Procedure

5.2.1 Materials

Tin tetraphenyl porphyrins were synthesized by a previously described method.[158] Briefly, free-base tetraphenyl porphyrin (H_2TPP) was treated with $SnCl_2 \cdot H_2O$ and hydrolyzed with K_2CO_3 in THF-H_2O at reflux.[165] The sample containing THF was dried and evaporated and added to dichloromethane. Further drying, evaporation and recrystallizations were performed to improve purity. $SnCl_2$TPP was treated with FcLi under low-temperature conditions, resulting in trans-chloro-ferrocene (5,10,15,20-tetraphenyl porphyrinato) tin(IV) (SnFcClTPP) and trans-bisferrocene (5,10,15,20 - tetraphenyl-porphyrinato) tin(IV) ($SnFc_2$TPP). The synthesized six-coordinate tin porphyrins exhibit an octahedral molecular configuration consisting of a planar porphyrin macrocycle and two axial ligands.

Indium porphyrins were synthesized using the same procedure as tin porphyrins.

Chloro-(5,10,15,20-tetraphenylporphyrinato) indium(III)(InClTPP) was synthesized using H_2TPP and treating with InCl $\cdot$ H_2O, hydrolyzed with K_2CO_3 in THF-H_2O, refluxed for 24 hr, dried, recyrstalized and purified. InClTPP was treated with ferrocene carboxylic acid and dissolved in dichloromethane. The solution was refluxed for 24 hours, evaporated and recrystalized, yielding ferrocenecarboxylato-(5,10,15,20-tetraphenylporphyrinato) indium(III)(InFcCO_2TPP).[166] Preparation of InFcTPP substituted ferrocene carboxylic acid with FcLi in the synthetic procedure, resulting in ferrocene(5,10,15,20-tetraphenylporphyrinato) indium(III)(InFcTPP). Synthesized five coordinate indium porphyrins exhibit out of plane torsion on the porphyrin ring into a pyramidal geometry. All molecular structures of indium and tin porphyrins can be seen in Figure 5.1.

5.2.2 Steady State Absorption and Emission

Absorption measurements of tin and indium porphyrins were obtained using the Cary-14 spectrometer. A 1 mm path length quartz cuvette was used for tin porphyrin solutions and background subtracted. Emission measurements were performed using a Fluorolog 1680 0.2 mm double grating spectrometer with a Xenon lamp source and photomultiplier tube for detection. Front face geometry was employed for photoluminescence measurements and prepared solutions were diluted in toluene to a concentrations of 100 μM.

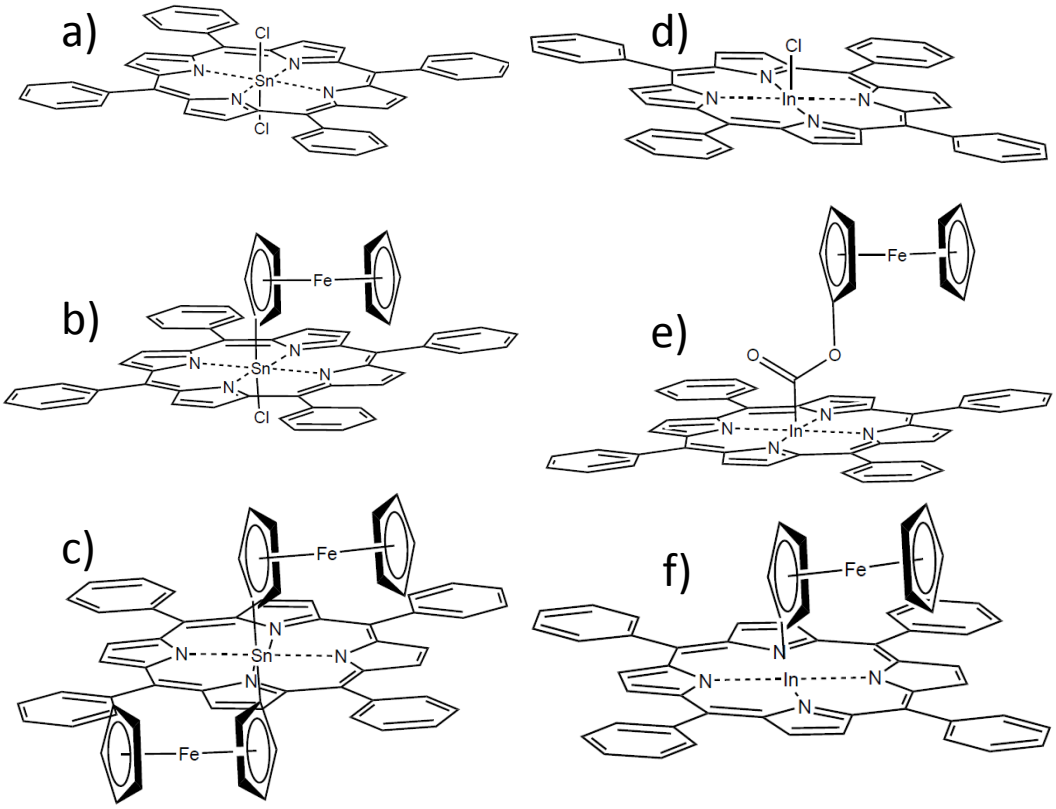

Figure 5.1: Molecular structures of tin and indium porphyrins. Molecule (a) is $SnCl_2TPP$, (b) is SnFcClTPP, (c) is $SnFc_2TPP$, (d) is InClTPP, (e) is $InFcCO_2TPP$, and (f) is InFcTPP.

5.2.3 Time Resolved Single Photon Counting

Time resolved single photon counting experiments were performed at the University of Minnesota-Duluth by Pavlo Solntsev under the direction of Professor Ahmed Heikal. A 2.64 eV pulse was incident on the sample in a 1 cm cuvette. Fluorescence collected with a 2 cm focusing lens employing front face geometry.

5.2.4 Ultrafast Pump-Probe Measurements

Ultrafast measurements on tin porphyrins involved excitation in both Q (S_1) and B (S_2) bands for comparisons of the excited state dynamics and their dependence on excitation energy. Samples were run continuously with no changes in spot size, fluence, pulse crossing, or polarization. For B band excitation, 1.55 eV, 1 kHz pulses were compressed to 94 fs, modulated through a beam chopper to 500 Hz and then frequency doubled through a BBO crystal to 3.1 eV. The pulse was focused to a 114 μm ($1/e^2$) diameter spot with a pump energy of 120 nJ per pulse. Probe light was focused with a 10 cm lens into a 1 mm thick CaF_2 window, generating a white light continuum from 3.54 eV to 1.45 eV. Due to the color centering effect observed in CaF_2, the window was linearly translated 3 mm from the origin with a random deviation of 0.3 mm at each end. The white light was focused on the sample, collimated and refocused into the array detector. Q band excitation incorporated the use of the non-collinear parametric amplifier. Excitation pulses ranged between 2.21 eV to 1.98 eV and were compressed to 86 fs using a pair of SF10 prisms. Pulses were chopped to 500 Hz and focused to

a 135 μm diameter spot at a pump energy of 60 nJ per pulse. Solutions for ultrafast measurements had a concentration of 200 μM for Q band excitation but were diluted to 50 μM for B band excitation to resolve the ground state hole dynamics.

5.3 Results and Discussion

5.3.1 Tin Porphyrins

The absorption and emission properties of tin porphyrins have been well characterized in previous studies and are depicted in Figure 5.2.[69;158;167;168;169;170;171;155;67;147] A Soret (B) band (S_2) dominates the absorption spectra around 2.75 eV while a set of weakly absorbing Q bands (S_1) spans 1.9 eV to 2.5 eV. The B absorption band solely consists of degenerate (π,π*) transitions as predicted through computations (Appendix A.6). The Q bands are (π,π*) but are also comprised of ferrocene to π*, charge separated character (Fc,π*). $S_1 \rightarrow S_0$ emission was observed between 1.5 eV and 2.1 eV and is consistent with previous measurements yet no S_2 emission was observed in any tin porphyrins.[69]

Under B band excitation, $SnCl_2TPP$ shows the highest quantum yield while SnFc-ClTPP and $SnFc_2TPP$ show successively lower quantum yields and are presented in Table 5.3.1. Direct attachment of ferrocene ligands to the tin porphyrin macrocycle significantly adjusts the excited state properties and causes a large decrease in the quantum yield.

Q band excitation exhibits an identical trend in tin porphyrin quantum yields.

$SnCl_2TPP$ has the highest quantum yield (5.8×10^{-3}) while SnFcClTPP and $SnFc_2TPP$ have lower quantum yields, 3.9×10^{-3} and 1.6×10^{-3} respectively. As shown in Appendix A.6, the Q band in SnFcClTPP and $SnFc_2TPP$ have a large contribution from the broad (Fe,π^*) metal to ligand charge transfer (MLCT). The MLCT excitation immediately reduces the porphyrin ring, forming the charge separated state and preventing any radiative $S_1 \rightarrow S_0$ fluorescence and contributing to the loss of the quantum yield. The B absorption band does not have significant contribution from the MLCT, indicating there are excited state processes responsible for the fluorescence quenching and reduction of the quantum yield.

Molecule	B ϕ_{Fl}	Q ϕ_{Fl}	B τ_{CS} (ps)	B τ_{CR} (ps)	Q τ_{CS} (ps)	Q τ_{CR} (ps)
$SnCl_2TPP$	7.8 x 10^-3	5.8 x 10^-3	–	–	–	–
SnFcClTPP	2.3 x 10^-3	3.9 x 10^-3	0.43 ± 0.19	16 ± 2	0.37 ± 0.29	13 ± 2
$SnFc_2TPP$	1.5 x 10^-3	1.6 x 10^-3	0.42 ± 0.25	22 ± 2	0.45 ± 0.33	14 ± 3

Table 5.1: $S_1 \rightarrow S_0$ quantum yield results with a Nile Blue standard for S_2 excitation and Rhodamine B for S_1 excitation. Timescales of the charge separation (CS) and charge recombination (CR) under both B and Q band excitation are also presented. Loss of the $^1(\pi,\pi^*)$ through charge separation was measured at 2.5 eV and loss of the charge separated state ($SnTPP^-$ - Fc^+) due to recombination was measured at 2.7 eV.

Investigation of the fluorescence quenching through time resolved single photon counting of $SnCl_2TPP$ (1), SnFcClTPP (2), and $SnFc_2TPP$ (3) is shown in Figure 5.3. $SnCl_2TPP$ initially appears to have a shorter fluorescence lifetime than SnFcClTPP and $SnFc_2TPP$. However, fitting of the decays through a biexponential function reveals an interesting change in the dynamics. All three tin porphyrins have a fast $\sim$ 800 ps τ_1 consistent with previous intersystem crossing measurements[69] but also an $\sim$ 8 ns decay also due to intersystem crossing (Table 5.3.1.

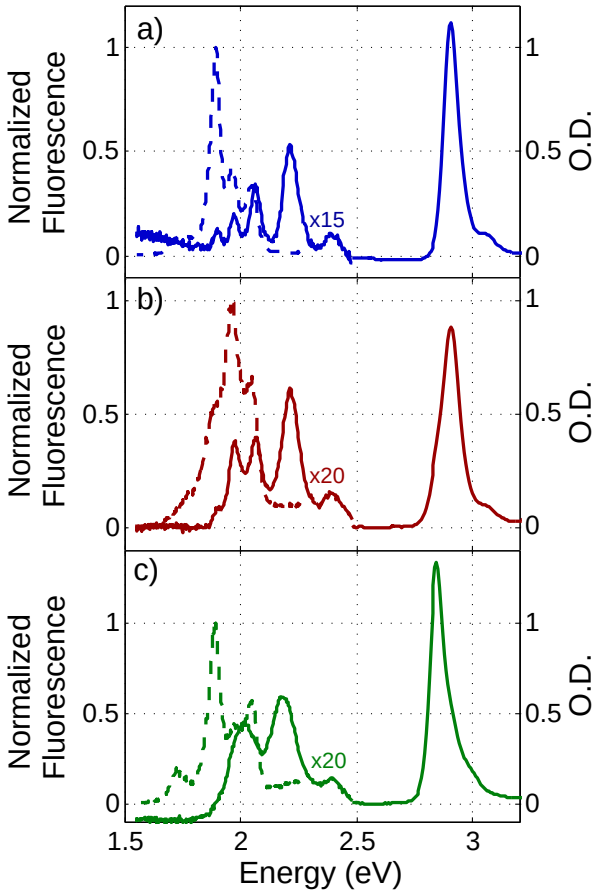

Figure 5.2: Absorption (solid) and normalized emission spectra (dashed) of $SnCl_2TPP$ (blue),SnFcClTPP (red), and $SnFc_2TPP$ (green) in panels a, b, and c, respectively.

Attachment of the ferrocene ligand does not significantly adjust the timescales but it does change the relative weights of these processes. $SnCl_2TPP$ is dominated by the fast 580 ps decay (96 %) weight. The weight is reduced to 61 % in SnFcClTPP and 31 % in $SnFc_2TPP$. While the 8 ns decay shows a corresponding weight increase with attachment of the ferrocene ligand, the amount of τ_2 decay between the porphyrins likely does not change. The fits shown are normalized to the intensity of the fluorescence, which, through time resolved measurements, is not equal in all three porphyrins. If all three decays were scaled to their respective quantum yield, the SnFcClTPP and $SnFc_2TPP$ decay would likely fit the tail of $SnCl_2TPP$ and reveal similar photoluminescent behavior beyond 1 ns.

Molecule	ISC τ_1 (ns)	Weight 1	ISC τ_2 (ns)	Weight 2
$SnCl_2TPP$	0.580	0.96	8.4	0.04
SnFcClTPP	0.830	0.61	8.2	0.39
$SnFc_2TPP$	0.790	0.31	8.6	0.69

Table 5.2: Parameters for biexponential fit of the time resolved fluorescence in Figure 5.3.

Ultrafast pump probe results on tin porphyrins under B band excitation are displayed in Figure 5.4. In the case of the non-substituted $SnCl_2TPP$ (Figure 5.4a), the excited state dynamics in B band excitation are very similar to the Q band excitation (Figure 5.5a). A broad transient absorption is observed between 2.4 and 2.7 eV and is attributed to transient absorption of the initially created $^1(\pi,\pi^*)$. Loss of the absorption around 2.7 eV and correlated growth at 2.6 eV is observed at long pump-probe delays, as indicated by the $\overset{3}{\rightarrow}$, and is attributed to intersystem crossing $^1(\pi,\pi^*) \rightarrow {}^3(\pi,\pi^*)$.

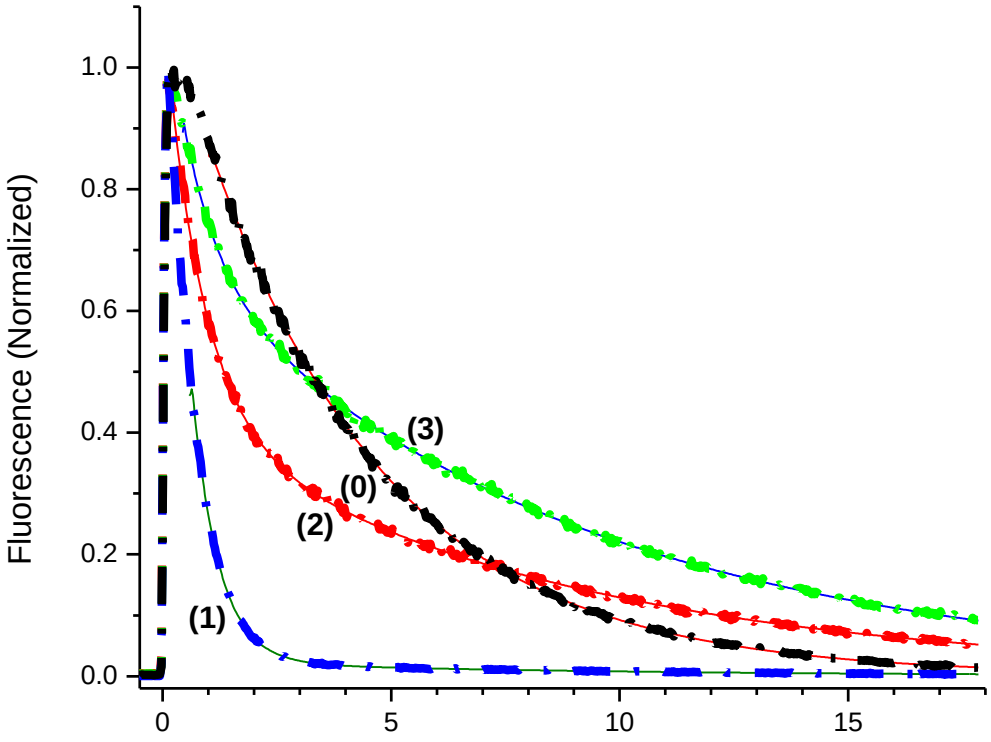

Figure 5.3: Time resolved fluorescence of (1, blue) $SnCl_2TPP$, (2, red) SnFcClTPP, and (3, green)$SnFc_2TPP$ with a (0, black) Rhodamine G standard.

The intersystem crossing assignment is consistent with previous singlet lifetime measurements around 1 ns.[69;171] The similarities in the excited state dynamics indicate very rapid internal conversion ($S_2 \rightarrow S_1$).

Attachment of the ferrocene ligand in SnFcClTPP significantly alters the excited state dynamics as shown in Figures 5.4b. The broad $^1(\pi,\pi^*)$ transient absorption between 2.4 and 2.6 eV decays rapidly and is correlated to growth of a sharp absorption at 2.75 eV with a time constant of (0.43 $\pm$ 0.19) ps as indicated on the spectra ($\overset{1}{\rightarrow}$). The resulting derivative like spectra indicates formation of a new species and is assigned to the reduced porphyrin[33;172] ($SnTPP^-$ - Fc^+) following electron transfer from the ferrocene ligand to the hole left behind on the highest occupied molecular orbital on the porphyrin ring. Sub-picosecond formation of the charge separated state prevents any radiative and non-radiative ($S_1 \rightarrow S_0$) decay. The transient absorption at 2.75 eV assigned to the reduced porphyrin decays with a time constant of (16 $\pm$ 2) ps ($\overset{2}{\rightarrow}$), indicating loss of the reduced porphyrin or charge separated state. Loss of the charge separated state is due to recombination of the electron in the lowest unoccupied molecular orbital (LUMO) with the hole on the ferrocene ligand, resulting in a net ground state as depicted in Figure 5.6. Following, but not correlated with, loss of the charge separated species, small growth is observed at 2.6 eV like that in $SnCl_2TPP$ and is attributed to intersystem crossing.

The excited state dynamics of $SnFc_2TPP$ are similar to SnFcClTPP and presented

in Figure 5.4c. After excitation, rapid electron transfer from the ferrocene to the porphyrin ring system creates the charge separated state ($SnTPP^-$ - Fc^+). More transient growth is observed at 2.8 eV, indicating more $^1(\pi,\pi^*)$ excited states deactivate through charge separation in $SnFc_2TPP$ compared to SnFcClTPP. Subsequently, the transient absorption at 2.8 eV is lost through recombination, indicating enhanced quenching of the excited states in $SnFc_2TPP$ relative to SnFcClTPP. At long pump probe delays after charge recombination, slight growth at 2.6 eV due to intersystem crossing is still observed.

Q band excitation reveals slight differences in the excited state dynamics in SnFcClTPP and $SnFc_2TPP$. DFT/TD-DFT calculations show both (π,π^*) and (Fe,π^*) contribute in Q band excitation as shown in the supporting information (SI1). The directly excited (Fe,π^*) charge separated state is evident in the excited state spectra in Figure 5.5b and 5.5c. Transient absorption at 0.1 ps shows more of the derivative shape than the B band excitation, yet still exhibits $^1(\pi,\pi^*) \rightarrow (Fe,\pi^*)$ charge separation with similar timescales. Loss of the charge separated states through recombination also occurs on timescales like those in B band excitation. The similarities of the excited state dynamics under B and Q band excitation in SnFcClTPP and $SnFc_2TPP$ indicate internal conversion dominates deactivation of S_2.

A proposal for the excited state quenching in tin tetraphenyl porphyrins involves multiple competing processes as shown in Equation 5.1. Upon excitation into the B band (S_2), the excited states quickly internally convert into the Q band (S_1) and form

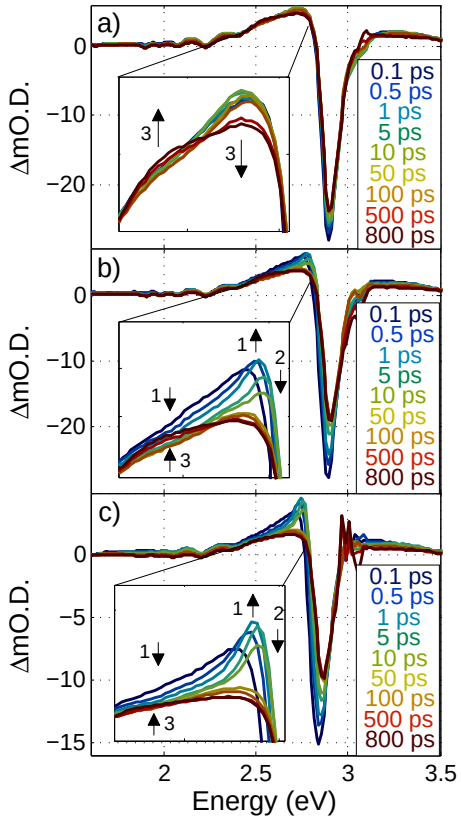

Figure 5.4: Pump-probe spectra of a) $SnCl_2TPP$, b) SnFcClTPP, and c)$SnFc_2TPP$ in toluene upon B band excitation. The zoomed panel shows the dynamics between 2.5 eV and 2.8 eV. for the respective porphyrin.

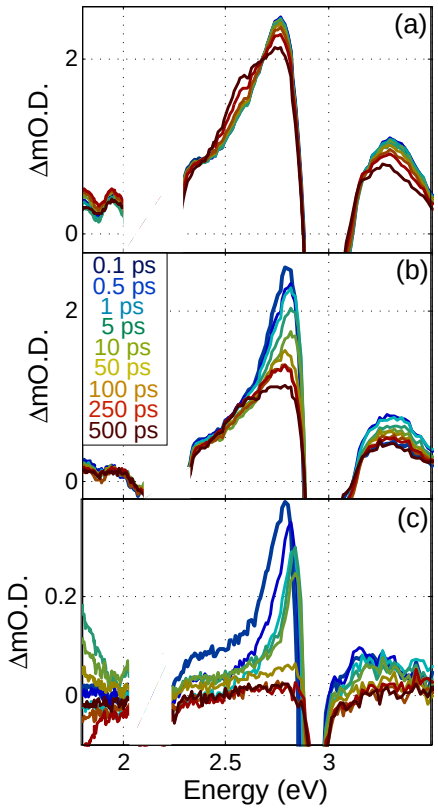

Figure 5.5: Pump-probe spectra of a) $SnCl_2TPP$, b) SnFcClTPP, and c)$SnFc_2TPP$ in toluene upon S_1 excitation. The zoomed panel shows the dynamics between 2.5 eV and 2.8 eV for each porphyrin. Regions around the Q and B ground state holes are removed due to pump scatter and strong absorption from the B band, respectively.

the excited singlet SnTPP*-Fc_2. The perturbation from equilibrium causes the charge separated state (SnTPP^{-}*-Fc_2^{+}) to form with a rate equal to the sum of the forward (k_{CS}) and backward (k_{CR}) rates. In this case, the backward rate dominates (τ_{CR} = 0.43 ps) while the forward rate is slow ($\tau_{CS} > 1$ ns). Loss of SnTPP*-Fc_2 through intersystem crossing occurs with a time constant $k_{ISC} \sim 1$ ns as observed in single photon counting experiments. While excitation in the Q band immediately creates some charge separated states, SnTPP*-Fc_2 and SnTPP^{-}*-Fc_2^{+} may not be at equilibrium and would show similar rates of formation.

There is a disparity between the time constants in the kinetics scheme proposed. Loss of the charge separated species through excited state quenching is $\sim$ 20 ps while intersystem crossing is $\sim$ 1 ns. Equilibrium between the neutral excited species (SnTPP* Fc_2) and charge separated species (SnTPP^{-*} $Fc_2{}^{+}$) is established shortly after excitation, however, loss of the charge separated species occurs much faster than the neutral excited species. The end result is predominant deactivation of the excited states through charge separation and quenching and little intersystem crossing. This result is at odds with the ultrafast results since roughly 50% of the singlets undergo intersystem crossing. The proposed scheme explains the dynamics within the first 50 ps, however, it does not account for, nor explain, the presence of singlet states and subsequent intersystem crossing at late pump probe delays (100-800 ps). Further analysis or experiments are

needed to fully explain the excited state dynamics.

$$SnTPP^{*}\,Fc_2\,(T_1) \xleftarrow{k_{ISC}} SnTPP^{*}\,Fc_2 \underset{k_{CS}}{\overset{k_{CR}}{\rightleftharpoons}} SnTPP^{-*}\,Fc_2{}^{+} \xrightarrow{k_{ESQ}} SnTPP\,Fc_2 \quad (5.1)$$

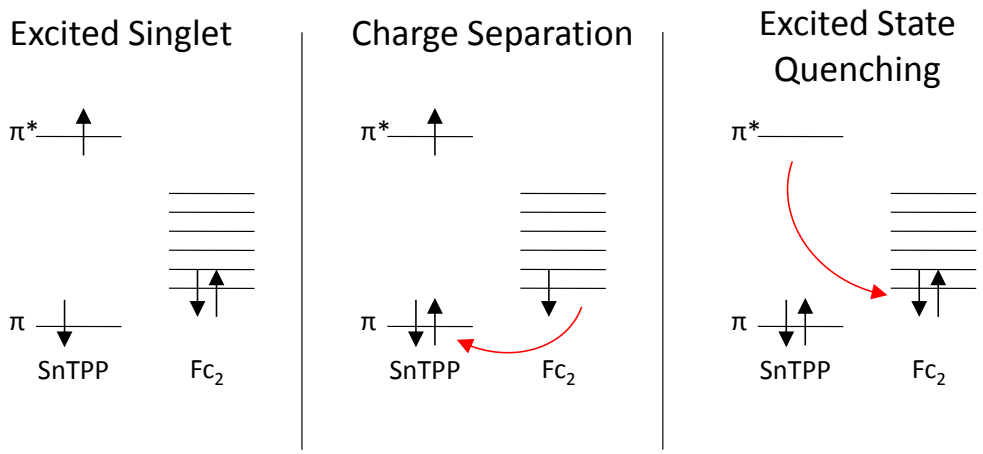

Figure 5.6: Molecular orbital depiction of charge separation and excited state quenching in $SnFc_2TPP$. The same processes apply to SnFcClTPP though there are only 3 ferrocene orbitals (Figure A.7.

5.3.2 Indium Porphyrins

InClTPP, $InFcCO_2TPP$, and InFcTPP reveal similar absorption and emission in Figure 5.7 when compared to tin porphyrin. InClTPP and $InFcCO_2TPP$ show nearly identical absorption and emission spectra. B band absorption is seen at 2.9 eV while the weakly

absorption Q bands are observed at 2.21 eV and 2.06 eV for InClTPP. InFcCO2TPP exhibits a small shift in both bands (2.89, 2.20, 2.05 eV), indicating the ferrocenecarboxylato ligand has some perturbation of the electronic structure of the indium porphyrin molecule. The small electronic perturbation was also seen in $Sn(FcCO_2)_2TPP$ studies.[69] Perturbation of the B band is observed with the directly attached ferrocene ligand in InFcTPP (2.89 eV) while the Q band has 3 absorption peaks rather than 2.

Emission is seen at 2.04 eV and 1.88 eV for all compounds, however, the fluorescence is slightly quenched in $InFcCO_2TPP$ and further quenched in $InFcCO_2TPP$ as shown in Table 5.3.2. Quenching of the fluorescence in through a carboxyl bridge was also observed in $Sn(FcCO_2)_2TPP$[69] while directly attached ferrocene groups in the previous section quenched the fluorescence of tin porphyrins.

Time resolved fluorescence behavior of the indium porphyrins is shown in Figure 5.8. All three porphyrins exhibited single exponential decay of the excited state with similar time constants around 0.3 ns, also the instrument response of the laser. Either little fluorescence is detected and is difficult to discern from any scatter or the lifetime is on the order of the instrument response. Due to the low quantum yield of the indium porphyrins and the lack of information retained through time correlated single photon counting, ultrafast spectroscopy is necessary to determine the excited state dynamics responsible for the fluorescence quenching behavior.

Investigation of the excited state dynamics of InClTPP, $InFcCO_2TPP$, and InFcTPP through pump probe spectroscopy are presented in Figures 5.9 and 5.10. As observed

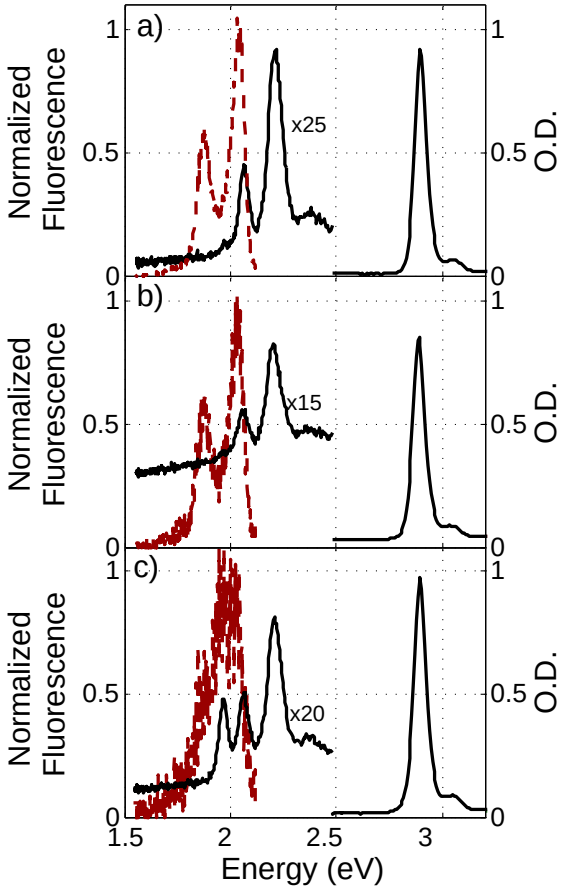

Figure 5.7: Absorption (black) and normalized emission spectra (red) of InClTPP (a),InFcCO_2TPP (b), and InFcTPP (c).

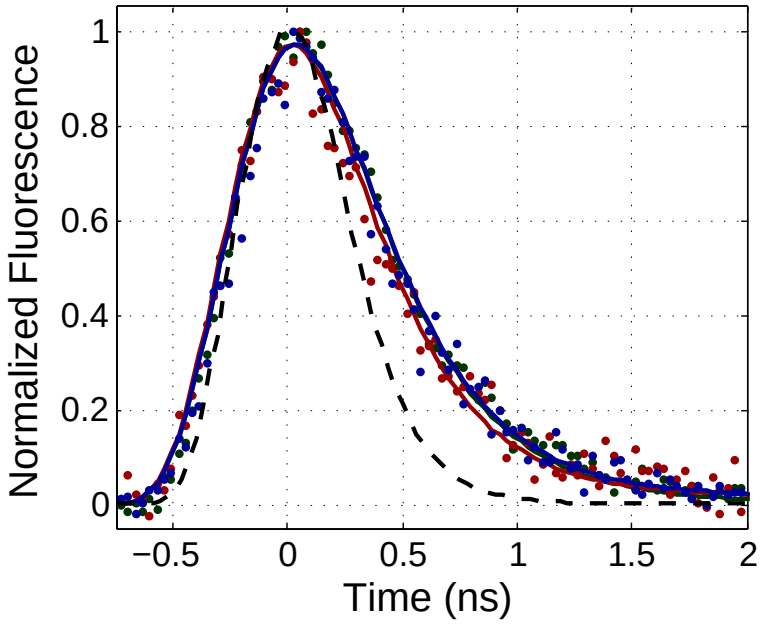

Figure 5.8: Time resolved fluorescence of InClTPP (blue), InFcCO_2TPP (red), and InFcTPP (green) with the instrument response dashed (black) using a single photon counter. Fluorescence was fit with 2 step sequential kinetics modeling the rise and decay of the spectra.

in the presented tin porphyrins, these indium porphyrins show similar dynamics in both B and Q band excitation. InClTPP exhibits behavior similar to $SnCl_2TPP$ as a broad $^1(\pi,\pi^*)$ transient absorption is seen between 1.8 eV and 2.8 eV with a ground state hole at 2.8 eV. Loss of transient absorption at 2.7 eV is correlated with growth at 2.6 eV at long time delays and closely resembles the $^1(\pi,\pi^*) \rightarrow {}^3(\pi,\pi^*)$ intersystem crossing transition observed in $SnCl_2TPP$ in Figure 5.4. Given the similarity of the size of these atoms, it is likely the spin orbit coupling would not be significantly altered and intersystem crossing rates would be comparable. Studies on indium phthalocyanines also estimate a 1 ns singlet lifetime[164] while the time resolved fluorescence measurements in Figure 5.8 estimate a singlet lifetime shorter than 1 ns.

Figure 5.9b illustrates the striking resemblance of the excited state dynamics in $InFcCO_2TPP$ when compared to InClTPP. The broad $^1(\pi,\pi^*)$ transient absorption decays at 2.7 eV with correlated growth at 2.6 eV, indicating S_1 deactivation occurs through $^1(\pi,\pi^*) \rightarrow {}^3(\pi,\pi^*)$ intersystem crossing. The similarities of the absorption, emission, and pump probe spectra in InClTPP and $InFcCO_2TPP$ suggests experimental error involving the two compounds. Any preparation errors would be apparent through multiple absorption and emission measurements with individual sample preparation. Furthermore, two separate batches of $InFcCO_2TPP$ were used for comparison.

Upon attachment of ferrocene in tin porphyrins, formation of charge separated states were observed. However, the pump probe evidence in Figure 5.9b suggests the carboxylic bridge prevents electron transfer from the iron in the ferrocene ligand to the HOMO in

the porphyrin macrocycle and the ferrocene does not significantly perturb the excited state dynamics. Previous measurements on carboxyl bridged $Sn(FcCO_2)_2$ observed photoluminescence quenching and changes in the pump probe spectra when compared to $SnCl_2TPP$.[69] The presented results show no fluorescence quenching and no significant changes in the excited state spectra in $InFcCO_2TPP$. Due to the difference in the central atom, molecular geometry and coordination, no direct comparison can be made to the $Sn(FcCO_2)_2$ results.[69]

Direct axial attachment of the ferrocene ligand to the indium porphyrin without a bridge alters the excited state dynamics in Figures 5.9c and 5.10c. Similar to that observed in SnFcClTPP and $SnFc_2TPP$, the broad $^1(\pi,\pi^*)$ shows rapid decay at 2.5 eV and correlated growth at 2.75 eV, corresponding to the charge separated (Fe,π^*) state. Formation of the charge separated state occurs on a similar timescales, (0.42 ± 0.1) ps, as those observed in tin porphyrins. The derivative like spectra is more clearly observed in Figure 5.10c and best illustrates the charge separated state. Spectral evidence indicates not all $^1(\pi,\pi^*)$ excited states undergo charge separation like that seen in tin porphyrins. Loss of the charge separated state occurs through recombination of the electron in the π^* orbital with the hole on the iron orbital. Recombination is observed with loss of the charge separated, derivative like spectra at 2.75 eV with a time constant of (18 ± 3.5) ps. Remaining $^1(\pi,\pi^*)$ excited states undergo intersystem crossing $^1(\pi,\pi^*) \rightarrow {}^3(\pi,\pi^*)$ and is observed between 500 ps and 800 ps.

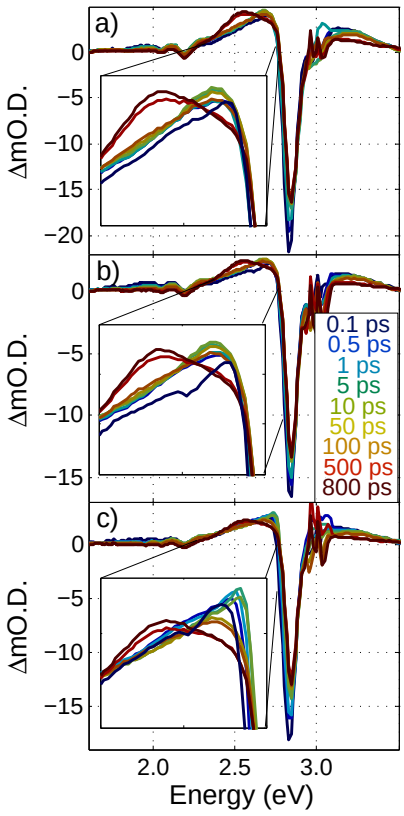

Figure 5.9: Pump-probe spectra of a) InClTPP, b) $InFcCO_2TPP$, and c)InFcTPP in toluene upon S_2 excitation. The zoomed panel illustrates the dynamics between 2.4 eV and 2.8 eV for each porphyrin. Regions around the Q and B ground state holes are removed due to pump scatter and strong absorption from the B band, respectively.

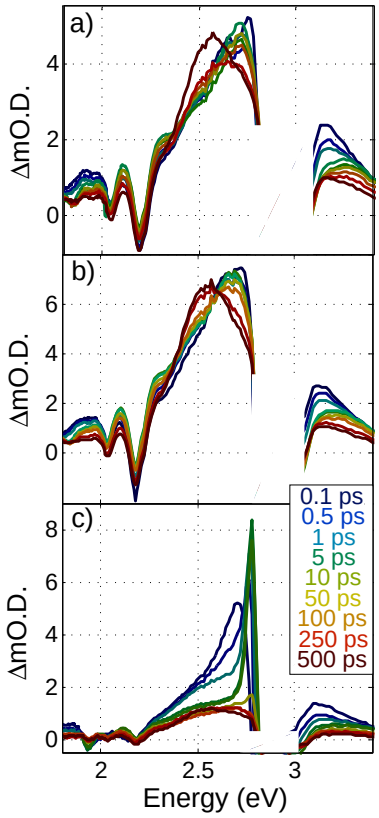

Figure 5.10: Pump-probe spectra of a) $SnCl_2TPP$, b) SnFcClTPP, and c)$SnFc_2TPP$ in toluene upon S_1 excitation. The zoomed panel shows the dynamics between 2.5 eV and 2.8 eV for each porphyrin. Regions around the Q and B ground state holes are removed due to pump scatter and strong absorption from the B band, respectively.

Molecule	B ϕ_{Fl}	Q ϕ_{Fl}	B τ_{CS} (ps)	B τ_{CR} (ps)	Q τ_{CS} (ps)	Q τ_{CR} (ps)
InClTPP	2.6 x 10^-3	2.0 x 10^-3	–	–	–	–
InFcCO_2TPP	1.8 x 10^-3	1.3 x 10^-3	–	–	–	–
InFcTPP	1.4 x 10^-3	1.3 x 10^-3	0.42 ± 0.1	18 ± 3.5	0.43 ± 0.1	7 ± 1

Table 5.3: $S_1 \rightarrow S_0$ fluorescence quantum yield results with a Nile Blue standard for S_2 excitation and Rhodamine B for S_1 excitation. Charge separation (CS) and charge recombination (CR) timescales are also presented. Loss of the $^1(\pi,\pi^*)$ through charge separation was measured at 2.5 eV and loss of the charge separated state ($InTPP^-$ - Fc^+) due to recombination was measured at 2.7 eV.

The photophysical behavior of the exicted state processes of $SnCl_2$TPP, SnFcClTPP, and $SnFc_2$TPP are presented in Figure 5.11. Excitation into S_2 results in internal conversion ($S_2 \rightarrow S_1$) in all studied porphyrins. For $SnCl_2$TPP, InClTPP, and InFcCO_2TPP, deactivation of S_1 is dominated through non-radiative $^1(\pi,\pi^*) \rightarrow {}^3(\pi,\pi^*)$ intersystem crossing. The presence of ferrocene ligands in SnFcClTPP, $SnFc_2$TPP, and InFcTPP provides another S_1 deactivation pathway. After excitation, some of the $^1(\pi,\pi^*)$ undergoes electron transfer from the ferrocene ligand to the porphryin centered HOMO and forms a charge separated state. The charge separated state is quenched through recombination ($\pi^* \rightarrow$ Fe) while remaining $^1(\pi,\pi^*)$ undergoes intersystem crossing ($^1(\pi,\pi^*) \rightarrow {}^3(\pi,\pi^*)$) as observed in $SnCl_2$TPP, InClTPP, and InFcCO_2TPP. As stated previously, the diagram explains the excited state quenching behavior but can not explain the presence of long lived $^1(\pi,\pi^*)$ and $^1(\pi,\pi^*) \rightarrow {}^3(\pi,\pi^*)$ intersystem crossing due to the large disparity in the time constants.

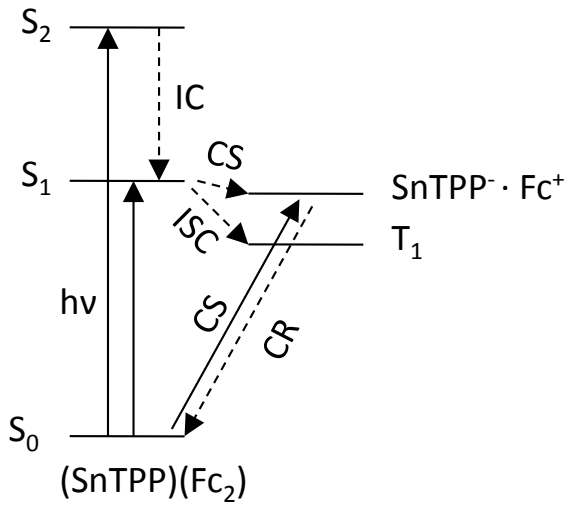

Figure 5.11: Deactivation of S_2 and S_1. S_2 decays through internal conversion (IC) to S_1 within our time resolution. S_1 is described here as the $^1(\pi,\pi^*)$ excited state and is deactivated through charge separation (CS) as well as intersystem crossing (ISC). The charge separated state ($SnTPP^-$ - Fc^+) can be formed through direct excitation or electron transfer after $^1(\pi,\pi^*)$ Q band excitation. Loss of the charge separated state occurs through charge recombination (CR, also excited state quenching, ESQ) from $\pi^* \rightarrow$ Fc and results in a ground state. Excited triplet states in T_1 will relax to the ground state through radiative and non-radiative means but are not observed through our experiments.

5.4 Conclusion

The dynamics of chloro and ferrocene substituted tin and indium porphyrins have been explored. All the studied tin and indium porphyrins exhibit low radiative quantum yields ($\sim$1 x 10^{-3}) with lower yields as a function of ferrocene substitution. Subpicosecond formation of the charge separated state in SnFcClTPP, $SnFc_2TPP$, and InFcTPP explains the enhanced fluorescence quenching in time-integrated photoluminescent measurements. Electron transfer (Fe $\rightarrow$ π) refills the hole on the porphyrin HOMO, preventing radiative decay from $S_1 \rightarrow S_0$. The charge separated state is quenched through ($\pi^* \rightarrow$ Fe) electron transfer, resulting in the ground state configuration. Curiously, there are long lived $^1(\pi,\pi^*)$ that remain after the rapid charge transfer and quenching which has yet to be fully explained. The useful combination of rapid charge separation and strong molecular arrays show promise for ferrocene substituted, tin porphyrin based photosynthetic devices.

References

[1] D.A. McQuarrie and J.D. Simon. *Physical Chemistry: A Molecular Approach.* University Science Books, Sausalito, CA, 1997.

[2] NREL Best Research-Cell Efficiencies. Accessed 6.1.2013, http://en.wikipedia.org/wiki/File:PVeff(rev100414).png, 2013.

[3] Q.Y. Xu K.M. Kadish and J.M. Barbe. Electrochemistry of a metalloporphyrin-bridging biferrocene complex. reactions of fc-(oep)ge-fc. *Inorganic Chemistry*, 26(16):2565–2566, 1987.

[4] NREL Reference Solar Spectrum Irradiance: AM 1.5. Accessed 6.10.2013, http://rredc.nrel.gov/solar/spectra/am1.5/, 2013.

[5] X. Zhang, E.C. Wasinger, A.Z. Muresan, K. Attenkofer, G. Jennings, J.S. Lindsey, and L.X. Chen. Ultrafast stimulated emission and structural dynamics in nickel porphyrins. *Journal of Physical Chemistry A*, 111(46):11736–11742, 2007.

[6] U.S. Energy Information Administration. International energy outlook 2011-highlights. *Website*, 2011.

[7] Nathan S. Lewis. Powering the planet. *MRS Bulletin*, 32:808–820, 2007.

[8] Martin I. Hoffert. Advanced technology paths to global climate stability: Energy for a greenhouse planet. *Science*, 298:981–987, 2002.

[9] M. Hoel and S. Kverndokk. Depletion of fossil fuels and the impacts of global warming. *Resource and Energy Economics*, 18(2).

[10] D. Newbery. Oil shortage, climate change and collective action. *Philosophical Transactions of the Royal Society A: Mathematical, Physical and Engineering Sciences*, 369(1942):1748–1761, 2011.

[11] M.R. Raupach, G. Marland, P. Ciais, C.L. Quere, J.G. Canadell, G. Klepper, and C.B. Field. Global and regional drivers of accelerating co2 emissions. *Proceedings of the National Academy of Sciences*, 104(24):10288–10293, 2007.

[12] J. Barber. Photosynthesis in relation to model systems, vol. 3. *Elsevier Scientific Publishing Company:Amsterdam*, 1979.

[13] A.E. Becquerel. Memoire sur les effets electiques produits sous i'influence des rayons solaris. *Comptes Rendes*, 9:561–567, 1839.

[14] R. Ohl. *U.S. Patent 2402662*, 1946.

[15] Meng Tao. Inorganic photovoltaic solar cells: Silicon and beyond. *The Electrochemical Society*, Interface, 2008.

[16] J. Zhao, A. Wang, and M.A. Green. 19.8 percent efficient honeycomb textured multicrystalline and 24.4 percent monocrystalline silicon solar cells. *Applied Physics Letters*, 73(14), 1998.

[17] Stephen R. Forrest. The path to ubiquitous and low-cost organic electronic appliances on plastic. *Nature*, 428:911–918, 2004.

[18] C.A. Wolden, J. Kurtin, J.B. Baxter, I. Repins, S.E. Shaheen, J.T. Torvik, A.A. Rockett, V.M. Fthenakis, and E.S. Aydil. Photovoltaic manufacturing: Present status, future prospects, and research needs. *Journal of Vacuum Science and Technology*, 29(3):1–16, 2011.

[19] C. Goh and M. McGehee. Criteria for choosing transparent conductors. *MRS Bull*, 25:52–57, 2000.

[20] B. Minnaert and M. Burgelman. Efficiency potential of organic bulk heterojunction solar cells. *Progress in Photovoltaics: Research and Applications*, 15:741–748, 2007.

[21] C.W. Tang and A.C. Albrecht. Photovoltaic effects of metal-chlorophyll-a-metal sandwich cells. *Journal of Chemical Physics*, 62(6), 1974.

[22] C. W. Tang. Two-layer organic photovoltaic cell. *Applied Physics Letters*, 48(2):183–185, 1986.

[23] P. Peumans and S.R. Forrest. Very-high-efficiency double-heterostructure phthalocyanine/c60 photovoltaic cells. *Applied Physics Letters*, 79(1):126–128, 2001.

[24] J. Franck. Elementary processes of photochemical reactions. *Transactions of the Faraday Society*, 21:536–542, 1926.

[25] M. Kasha. Characterization of electronic transitions in complex molecules. *Discussions of the Faraday Society*, 9:14–19, 1950.

[26] C.M. Marian. Spin-orbit coupling and intersystem crossing in molecules. *WIREs Comput Mol Sci*, 2:187–203, 2012.

[27] E. Rabinowitch. Spectra of porphyrins and chlorophyll*. *Journal of Physical Chemistry B*, 16(3-4):226–235, 1944.

[28] H.P. Longuet-Higgins, C.W. Rector, and J.R. Platt. Molecular orbital calculations on porphine and tetrahydroporphine. *Journal of Chemical Physics*, 18(9):1174–1181, 1950.

[29] W.T. Simpson. On the theory of the π-electron system in porphines. *Journal of Chemical Physics*, 17(12).

[30] J.R. Platt. *Radiation Biology*, volume III. McGraw Hill, 1956.

[31] M. Gouterman, G.H. Wagniere, and L.C. Snyder. Spectra of porphyrins part ii. four orbital model. *Journal of Molecular Spectroscopy*, 11:108–127, 1963.

[32] A. Ceulemans, W. Oldenhof, C. Gorller-Walrand, and L. G. Vanquickenborne. Gouterman's four-orbital model and the mcd spectra of high-symmetry metalloporphyrins. *Journal of the American Chemical Society*, 108(6):1155–1163, 1986.

[33] D. Dolphin, editor. *The Porphyrins*, volume Vol. 3. Academic Press, New York, 1978-1979.

[34] M. Zerner and M. Gouterman. *Theoretica Chimica Acta*, 4(44), 1960.

[35] M. Zerner and M. Gouterman. *Theoretica Chimica Acta*, 8(26), 1967.

[36] M. Zerner and M. Gouterman. *Inorganic Chemistry*, 5, 1966.

[37] T. Fórster. Transfer mechanisms on electronic excitations. *10th Spieres Memorial Lecture*, pages 7–17, 1959.

[38] T. Förster. *Ann. Phys.*, 457:55–75, 1948.

[39] S.H. Lin, W.Z. Xiao, and W. Dietz. Molecular memories that survive silicon device processing and real-world operation. *Physical Review E*, 47(5):3698–3706, 1993.

[40] M.Z. Maksimov and I.M. Rozman. Energy transfer in solid solutions. *Optics and Spectroscopy*, 12:606–609, 1962.

[41] D.L. Dexter. A theory of sensitized luminescence in solids. *Journal of Chemical Physics*, 21(5):836–850, 1953.

[42] B.A. Gregg and M.C. Hanna. Comparing organic to inorganic photovoltaic cells: Theory, experiment, and simulation. *Journal of Applied Physics*, 93(6):3605–3614, 2003.

[43] W. Shockley and H.J. Queisser. Detailed balance limit of efficiency of p-n junction solar cells. *Journal of Applied Physics*, 32(3):510–519, 1961.

[44] P.K. Nayak, G. Garcia-Belmonte, A. Kahn, J. Bisquert, and D. Cahen. Photovoltaic efficiency limits and material disorder. *Energy and Environmental Science*, 5:6022, 2012.

[45] C.S. Solanki and C. Beaucarne. Advanced solar cell concepts. *Energy for Sustainable Development*, XI(3):17–23, 2007.

[46] D. Wöhrle and D. Meissner. Organic solar cells. *Advanced Materials*, 3(3):129–138, 1991.

[47] S. Forrest P. Peumans, A. Yakimov. Small molecular weight organic thin-film photodetectors and solar cells. *Journal of Applied Physics*, 93(7):3693–3723, 2003.

[48] Anna A. Belak Jay B. Benziger Richard R. Lunt, Noel C. Giebink and Stephen R. Forrest. Exciton diffusion lengths of organic semiconductor thin films measured

by spectrally resolved photoluminescence quenching. *Journal of Applied Physics*, 105(1):053711, 2009.

[49] J. Kalowekamo and E. Baker. Estimating the manufacturing cost of purely organic solar cells. *Solar Energy*, 2009.

[50] W.A. Luhman and R.J. Holmes. Enhanced exciton diffusion in an organic photovoltaic cell by energy transfer using a phosphorescent sensitizer. *Applied Physics Letters*, 94(153304):1–3, 2009.

[51] P.F. Moulton. Spectroscopic and laser characterization of ti:al$_2o_3$. *Journal of Optical Society of America B*, 3(1):125–133, 1986.

[52] P. Albers, E. Stark, and G. Huber. Continuous-wave laser operation and quantum efficiency of titanium doped sapphire. *Journal of Optical Society of America B*, 3(1):134–139, 1986.

[53] H.A. Haus. Mode-locking of lasers. *IREE Journal on Selected Topics in Quantum Electronics*, 6(6).

[54] A.E. Siegman and D.J. Kuizenga. Modulator frequency detuning effects in the fm mode-locked laser. *IREE Journal of Quantum Electronics*, 6(12).

[55] G. Cerullo, S. De Silvestri, V. Magni, and L. Pallaro. Resonators for kerr-lens mode-locked femtosecond ti:sapphire lasers. *Optics Letters*, 19(11):807–809, 1994.

[56] G. Cerullo and S. De Silvestri. Ultrafast optical parametric amplifiers. *Review of Scientific Instruments*, 74(1):1–18, 2003.

[57] J. Piel, M. Beutter, and E. Riedle. 2050-fs pulses tunable across the near infrared from a blue-pumped noncollinear parametric amplifier. *Optics Letters*, 25(3):180–182, 2000.

[58] T. Wilhelm, J. Piel, and E. Riedle. Sub-20-fs pulses tunable across the visible from a blue-pumped single-pass noncollinear parametric converter. *Optics Letters*, 22(19):1494–1496, 1997.

[59] P.J.M. Johnson, V.I. Prokorhenko, and R.J.D. Miller. Enhanced bandwidth noncollinear optical parametric amplification with a narrowband anamorphic pump. *Optics Letters*, 36(11):2170–2172, 2011.

[60] F. Wilkinson, D.J. McGarvey, and A.F. Olea. Excited triplet state interactions with molecular oxygen: Influence of charge transfer on the bimolecular quenching rate constants and the yields of singlet oxygen (o_2^*,$^1\delta_g$) for substituted naphthalenes in various solvents. *The Journal of Physical Chemistry*, 98:3762–3769, 1994.

[61] E.I. Sagun, E.I. Zenkevich, V.N. Knyukshto, S.A. Tikhomirov, and A.M. Shulga. Picosecond dynamics of photoinduced electron transfer involving singlet and triplet states in nitroporphyrin molecules. *Molecular Spectroscopy*, 96(3):404–418, 2004.

[62] K. Kawaoka, A.U. Khan, and D.R. Kearns. Role of singlet excited states of molecular oxygen in the quenching of organic triplet states. *Journal of Chemical Physics*, 46(5):1842–1853, 1967.

[63] F. Wilkinson, W.P. Helman, and A.B. Ross. Rate constants for the decay and reactions of the lowest electronically excited singlet state of molecular oxygen in solution. an expanded and revised compilation. *The Journal of Physical and Chemical Reference Data*, 24(663), 1995.

[64] A.D. Joran, B.A. Leland, P.M. Felker, A.H. Zewail, and P.B. Dervan. Effect of exothermicity on electron transfer rates in photosynthetic molecular models. *Nature*, 327:508–511, 1987.

[65] L.R. Khundkar, J.W. Perry, J.E. Hanson, and P.B. Dervan. Weak temperature dependence on electron transfer rates in fixed-distance porphyrin-quinone model systems. *Journal of the American Chemical Society*, 116:9700–9709, 1994.

[66] D. P. Arnold, G. A. Heath, and D. A. James. Porphyrin dimers linked by conjugated butadiyne bridges: Preparations, spectra, voltammetry and reductive spectroelectrochemistry of [M(OEP)](m-C4)[M(OEP)] (m2=h4, co2, ni2, cu2, zn2, pd2, pt2, co/ni, ni/cu, ni/zn). *J. Porphyrins and Pthalocyanines*, 3:5–31, 1998.

[67] A. Endo, K. Sato, K. Yoshimura, T. Kai, A. Kawada, H. Miyazaki, and C. Adachi. Efficient up-conversion of triplet excitons into a singlet state and its application for organic light emitting diodes. *Applied Physics Letters*, 98(083302), 2011.

[68] K. Burda, A. Hrynkiewicz, H. Koloczek, J. Stanek, and K. Strzalka. Molecular dynamics and local electronic states of sn and fe in metallocytochrome and metalloporphyrin. *Hyperfine Interactions*, 91:891–897, 1994.

[69] J.H. Jang, H.J. Kim, H.J. Kim, C.H. Kim, T. Joo, D.W. Cho, and M. Yoon. Ultrafast time-resolved laser spectroscopic studies of trans-bis(ferrocene-carboxylato)(tetraphenyl-porphyrinato)tin(iv): Intramolecular electron-transfer dynamics. *Bulletin on Korean Chemical Society*, 28(11):1967–1972, 2007.

[70] J.H. Kim and J.H. Kim. Encapsulated triplet-triplet annihilation-based upconversion in the aqueous phase for sub-band-gap semiconductor photocatalysis. *Journal of the American Chemical Society*, 134:17478–17481, 2012.

[71] V.S. Shetti, Y. Pareek, and M. Ravikanth. Sn(iv) porphyrin scaffold for multiporphyrin arrays. *Coordination Chemistry Reviews*, 256:2816–2842, 2012.

[72] A. Osuka, S. Nakajima, K. Maruyama, N. Mataga, T. Asahi, I. Yamazaki, Y. Nishimura, T. Ohno, and K. Nozaki. 1,2-phenylene-bridged diporphyrin linked with porphyrin monomer and pyromellitimide as a model for a photosynthetic reaction center: Synthesis and photoinduced charge separation. *Journal of the American Chemical Society*, 115:4577–4589, 1993.

[73] C.M. Drain, S. Gentemann, J.A. Roberts, N.Y. Nelson, C.J. Medforth, S. Jia, M.C. Simpson, M.S. Smith, J. Fajer, J.A. Shelnutt, and D. Holten. Picosecond to microsecond photodynamics of a nonplanar nickel porphyrin: Solvent dielectric

and temperature effects. *Journal of the American Chemical Society*, 120(15):3781–3791, 1998.

[74] Hyo Soon Eom, Sae Chae Jeoung, Dongho Kim, Jeong-Hyon Ha, and Yong-Rok Kim. Ultrafast vibrational relaxation and ligand photodissociation/photoassociation processes of nickel(ii) porphyrins in the condensed phase. *Journal of Physical Chemistry A*, 101:3661–3669, 1997.

[75] Dongho Kim and Dewey Holten. Picosecond measurements on the binding and release of basic ligands by excited states of ni(ii) porphyrins. *Journal of the American Chemical Society*, 106:4015–4017, 1984.

[76] A.V. Zamyatin, A.V. Gusev, and M.A.J. Rodgers. Two-pump-one-probe femtosecond studies of ni(ii) porphyrins excited states. *Journal of American Chemical Society*, 126, 2004.

[77] Juan Rodriguez and Dewey Holten. Ultrafast photodissociation of a metalloporphyrin in the condensed phase. *Journal of Chemical Physics*, 92(10):5944–5950, 1990.

[78] Juan Rodriguez and Dewey Holten. Ultrafast vibrational dynamics of a photoexcited metalloporphyrin. *Journal of Chemical Physics*, 91(6):3525–3521, 1989.

[79] DeLyle Eastwood and Martin Gouterman. Porphyrins : Xviii. luminescence of

(co), (ni), pd, pt complexes. *Journal of Molecular Spectroscopy*, 35(3):359 – 375, 1970.

[80] S. Tewari, R. Das, A. Chakroborty, and R. Bhattacharjee. Resonance raman study on distorted symmetry of porphyrin in nickel octaethyl porphyrin. *Pramana Journal of Physics*, 63(5), 2004.

[81] Dae Won Cho Sae Chae Jeoung Dae Hong Jeong, Dongho Kim. Picosecond transient resonancs raman study on the excited state conformational dynamics of a highly ruffled nickel porphyrin. *Journal of Raman Spectroscopy*, 32:487–493, 2001.

[82] R.L. Ake and M. Gouterman. Porphyrins xx. theory for the states of ni(d^8) complexes. *Theoretical Chemistry Accounts*, 17:408–416, 1970.

[83] C. Berrios, C.I. Cardenas-Jiron, J.F. Marco, C. Gutierrez, and M.S. Ureta-Zanartu. Spin-orbit coupling and intersystem crossing in conjugated polymers: A configuration interaction description. *Journal of Physical Chemistry A*, 111:2706–2714, 2007.

[84] A. Rosa, G. Ricciardi, E.J. Baerends, M. Zimin, M.A.J. Rodgers, S. Matsumoto, and N. Ono. Structural, optical, and photophysical properties of nickel(ii) alkylthioporphyrins: Insights from experimental and dft/tddft studies. *Inorganic Chemistry*, 44:6609–6622, 2005.

[85] Dongho Kim, Dewey Holten, and Martin Gouterman. Evidence from picosecond transient absorption and kinetic studies of charge-transfer states in copper(ii) porphyrins. *Journal of the American Chemical Society*, 106(10):2793–2798, 1984.

[86] Martin Gouterman Artemis Antipas. Porphyrins. 44. electronic states of cobalt, nickel, rhodium, and palladium complexes. *Journal of the American Chemical Society*, 105(15):4896–4901, 1983.

[87] T. Kobayashi and A. Baltuska. Sub-5 fs pulse generation from a noncollinear optical parametric amplifier. *Measurement Science and Technology*, 13:1671–1682, 2002.

[88] S.H. Courtney, T.M. Jedju, J.M. Friedman, L. Rothberg, R.G. Alden, S.M. Park, and M.R. Ondrias. Excited-state conformational dynamics of nickel (ii) porphyrins. *Journal of Optical Society of America*, 7(8):1610–1614, 1990.

[89] L.X. Chen, X. Zhang, E.C. Wasinger, K. Attenkofer, G. Jennings, A.Z. Muresan, and J.S. Lindsey. Tracking electrons and atoms in a photoexcited metalloporphyrin by x-ray transient absorption spectroscopy. *Journal of the American Chemical Society*, 129:9616–9618, 2007.

[90] A. Harriman. Luminescence of porphyrins and metalloporphyrins. part i. zinc(ii), nickel(ii), and manganese(ii) porphyrins. *Journal of the Chemical Society. Faraday Transactions I.*, 76:1978–1785, 1980.

[91] W.A. Luhman and R.J. Holmes. Investigation of energy transfer in organic photovoltaic cells and impact on exciton diffusion length measurements. *Advanced Functional Materials*, 21:764–771, 2011.

[92] F.J. Kampas and M. Gouterman. Porphyrin films. 3. photovoltaic properties of octaethylporphyrins and tetraphenylporphine. *Journal of Physical Chemistry*, 81(8):690–695, 1977.

[93] M.G. Walter, A.B. Rudine, and C.C. Wamser. Porphyrins and phthalocyanines in solar photovoltaic cells. *Journal of Porphyrins and Phthalocyanines*, 14, 2010.

[94] J. Xue, S. Uchida, B.P. Rand, and S.R. Forrest. 4.2% efficient organic photovoltaic cells with low series resistance. *Applied Physics Letters*, 84(16):3013–3015, 2004.

[95] P. Zabel, Th. Dittrich, M. Funes, E. N. Durantini, and L. Otero. Charge separation at pd-porphyrin/tio2 interfaces. *Journal of Physical Chemistry C*, 113(50):21090–21096, 2009.

[96] X.D. Xu, J. Zhang, L.J. Chen, R. Guo, D.X. Wang, and H.B. Yang. Design and synthesis of branched platinumacetylide complexes possessing a porphyrin core and their self-assembly behaviour. *Chemical Communications*, 48:1122311225, 2012.

[97] T. Milic, J.C. Garno, J.D. Batteas, G. Smeureanu, and C.M. Drain. Self-organization of self-assembled tetrameric porphyrin arrays on surfaces. *Langmuir*,

20:3974–3983, 2004.

[98] A. Ciammaichella, P.O. Dral, T. Clark, P. Tagliatesta, M. Sekita, and D.M. Guldi. A π-stacked porphyrinfullerene electron donoracceptor conjugate that features a surprising frozen geometry. *Chemistry European Journal*, 18:14008 14016, 2012.

[99] Jarrres B. Callis, Joan M. Knowles, and Martin Gouterman. Porphyrins. xxvi triplet excimer quenching of free base, zinc, palladium, and platinum complexes. *The Journal of Physical Chemistry*, 77(2):154–157, 1973.

[100] Y. Yang Y. Shao. Efficient organic heterojunction photovoltaic cells based on triplet materials. *Advanced Materials*, 17(23):2841–2844, 2005.

[101] Michael A. Bergkamp Thomas L. Netzel Glauco Ponterini, Nick Serpone. Comparison of radiationless decay processes in osmium and platinum porphyrins. *Journal of the American Chemical Society*, 105(14):4639–4645, 1983.

[102] S.T. Roberts, C.W. Schlenker, V. Barlier, R.E. McAnally, Y. Zhang, J.N. Mastron, M.E. Thompson, and S.E. Bradforth. Observation of triplet exciton formation in a platinum-sensitized organic photovoltaic device. *Journal of Physical Chemistry Letters*, 2:48–54, 2011.

[103] A. Penzkofer Taiju Tsuboi A.K. Bansal, W. Holzer. Absorption and emission spectroscopic characterization of platinum-octaethyl-porphyrin (ptoep). *Journal of Chemical Physics*, 330:118–129, 2006.

[104] J. Kalinowski, W. Stampor, J. Szmytkowski, M. Cocchi, D. Virgili, V. Fattori, and P. Di Marco. Photophysics of an electrophosphorescent platinum (ii) porphyrin in solid films. *The Journal of Chemical Physics*, 122(15):154710, 2005.

[105] J. Kalinowski, W. Stampor, M. Cocchi, D. Virgili, V. Fattori, and P. Di Marco. Triplet energy exchange between fluorescent and phosphorescent organic molecules in a solid state matrix. *Journal of Chemical Physics*, 297:39–48, 2004.

[106] Taiju Tsuboi and Masayuki Tanigawa. Optical characteristics of ptoep and ir(ppy)3 triplet-exciton materials for organic electroluminescence devices. *Thin Solid Films*, 438-439:301–307, 2001.

[107] Taiju Tsuboi, Yoko Wasai, and Nataliya Nabatova-Gabain. Optical constants of platinum octaethyl porphyrin in single-layer organic light emitting diode studied by spectroscopic ellipsometry. *Thin Solid Films*, 496(8):674–678, 2006.

[108] Taiju Tsuboi, Hideyuki Murayama, and Alfons Penzkofer. Photoluminescence characteristics of ir(ppy)3 and ptoep doped in tpd host material. *Thin Solid Films*, 499:306–312, 2006.

[109] V. N. Knyukshto, A. M. Shulga, E. I. Sagun, and . I. Zenkevich. Formation of intersystem crossing transitions in pd(ii) and pt(ii) porphyrins: Nonplaner distortions of the macrocycle and charge transfer states. *Optics and Spectroscopy*, 100(4):590–601, 2006.

[110] Y. Amao, K. Asai, and I. Okura. Oxygen sensing based on lifetime of photoexcited triplet state of platinum porphyrin-polystyrene film using time-resolved spectroscopy. *Journal of Porphyrins and Phthalocyanines*, 4(3):292–299, 2000.

[111] Y. Amao, K. Asai, T. Miyashita, and I. Okura. Novel optical oxygen sensing material: Platinum porphyrin-styrene-pentafluorostyrene copolymer film. *Analytical Communications*, 36:367–369, 1999.

[112] G. DiMarco and M. Lanza. Optical solid-state oxygen sensors using metalloporphyrin complexes immobilized in suitable polymeric matrices. *Sensors and Actuators B*, Perkin Trans.(63):42–48, 2000.

[113] S.M. Borisov, R. Saf, R. Fischer, and I. Klimant. Synthesis and properties of new phosphorescent red light-excitable platinum(ii) and palladium(ii) complexes with schiff bases for oxygen sensing and triplet-triplet annihilation-based upconversion. *Physica Scripta*, 52:1206–1216, 2012.

[114] Christopf Weder Felix N. Castellano Radiy R. Islangulov, Joseph Lott. Noncoherent low-power upconversion in solid polymer films. *Journal of the American Chemical Society*, 129(42):12652–12653, 2007.

[115] Y. Cheng, B. Fuckel, T. Khoury, R. Clady, M. Tayebjee, N. Ekins-Daukes, M. Crossley, and T. Schmidt. Kinetic analysis of photochemical upconversion by triplet-triplet annihilation: Beyond and spin statistical limit. *Journal of Physical Chemistry Letters*, 1:1795–1799, 2010.

[116] Y.Y. Cheng, T. Khoury, R.G.C.R Clady, M.J.Y Tayebjee, N.J. Ekins-Daukes, M.J. Crossley, and T.W. Schmidt. On the efficiency limit of triplet-triplet annihilation for photochemical upconversion. *Physical Chemistry Chemical Physics*, 12:66–71, 2010.

[117] J.E. Kroeze, T.J. Savenije, and J.M. Warman. Efficient charge separation in a smooth-tio2/palladium-porphyrin bilayer via long-distance triplet-state diffusion. *Advanced Materials*, 14(23):1760–1763, 2002.

[118] V. Jankus, E.W. Snedden, D.W. Bright, V.L. Whittle, J.A.G. Williams, and A. Monkman. Energy upconversion via triplet fusion in super yellow ppv films doped with palladium tetraphenyltetrabenzoporphyrin: a comprehensive investigation of exciton dynamics. *Advanced Functional Materials*, pages 1–10, 2012.

[119] D. Beljonne, Z. Shuai, G. Pourois, and J.L. Bredas. Spin-orbit coupling and intersystem crossing in conjugated polymers: A configuration interaction description. *Journal of Physical Chemistry A*, 105:3899–3907, 2001.

[120] E.A. Gastilovich, V.G. Klimenko, N.V. Korol'kova, and R.N. Nurmukhametov. Effect of a heavy atom in the $s_1(\pi\pi*) \rightarrow t_1(\pi\pi*)$ nonradiative transition. 9,10-dichlororanthracene. *Optics and Spectroscopy*, 105(4).

[121] S.P. McGlynn, T. Azumi, and M. Kasha. External heavy-atom spin-orbit coupling effect. v. absorption studies of triplet states. *Journal of Chemical Physics*, 40(2):507–515, 1964.

[122] P.J. Spellane, M. Gouterman, A. Antipas, S. Kim, and Y.C. Liu. Porphyrins. 40. electronic spectra and four orbital energies of free-base, zinc, copper, and palladium tetrakis(perfluorophenyl)porphyrins. *Inorganic Chemistry*, 19:386–391, 1980.

[123] A. Starukhin and M. Kruk. Photophysics of pt-porphyrin electrophosphorescent devices emitting in the near infrared. *Journal of Porphyrins and Phthalocyanines*, 13:958–963, 2009.

[124] Waldemar Stampor. Electroabsorption study of vacuum-evaporated films of pt(ii)octaethylporphyrin. *Journal of Chemical Physics*, 305(1-3):77–84, 2004.

[125] F. Nifiatis, W. Su, J.E. Haley, J.E. Slagle, and T.M. Cooper. Comparison of the photophysical properties of a planar, ptoep, and a nonplanar, ptoetpp, porphyrin in solution and doped films. *Journal of Physical Chemistry A*, 115:13764–13772, 2011.

[126] Kohei Hosomizu, Masaaki Oodoi, Tomokazu Umeyama, Yoshihiro Matano, Kaname Yoshida, Seiji Isoda, Marja Isosomppi, Nikolai V. Tkachenko, Helge Lemmetyinen, and Hiroshi Imahori. Substituent effects of porphyrins on structures and photophysical properties of amphiphilic porphyrin aggregates. *Journal of Physical Chemistry B*, 112(51):16517–16524, 2008.

[127] R.F. Khairutdinov and N. Serpone. Laser-induced light attenuation in solutions of porphyrin aggregates. *Journal of Physical Chemistry*, 99:11952–11958, 1995.

[128] B.P. Rand, J. Genoe, P. Heremans, and J. Poortmans. Solar cells utilizing small molecular weight organic semiconductors. *Progress in Photovoltaics: Research and Applications*, 15:659–676, 2007.

[129] Thomas Kietzke. Recent advances in organic solar cells. *Advances in OptoElectronics*, 2007.

[130] H. Katagiri, K. Saitoh, T. Washio, H. Shinohara, T. Kurumadani, and S. Miyajima. Development of thin film solar cell based on cu2znsns4 thin films. *Solar Energy Materials and Solar Cells*, 65:141–148, 2001.

[131] B.A. Gregg. Excitonic solar cells. *Journal of Physical Chemistry B*, 107(20):4688–4698, 2003.

[132] R.J. Holmes and S.R. Forrest. Exciton-photon coupling in organic materials with large intersystem crossing rates and strong excited state molecular relaxation. *Physical Review B*, 71:235203, 2005.

[133] Stefan C.J. Meskers Martien J.W. Vermeulen Laurens D.A. Siebbeles Annemarie Huijser, Tom J. Savenije. The mechanism of long-range exciton diffusion in a nematically organized porphyrin layer. *Journal of the American Chemical Society*, 130(17):12496–12500, 2008.

[134] M.A. Baldo, D.F. O'Brien, Y. You, A. Shoustikov, S. Sibley, M.E. Thompson, and

S.R. Forrest. Highly efficient phosphorescent emission from organic electroluminescent devices. *Nature*, 395:151–154, 1998.

[135] R.C. Kwong, S. Sibley, T. Dubuvoy, M. Baldo, S.R. Forrest, and M.E. Thompson. Efficient, saturated red organic light emitting devices based on phosphorescent platinum (ii) porphyrins. *Chemical Materials*, 11:3709–3713, 1999.

[136] T.N. Singh-Rachford and F.N. Castellano. Photon upconversion based on sensitized triplet-triplet annihilation. *Coordination Chemistry Reviews*, 254:2560–2573, 2010.

[137] G. Lieser P.E. Keivanidis, S. Baluschev and G. Wegner. Inherent photon energy recycling effects in the upconverted delayed luminescence dynamics of polyfluorene-pt(ii) octaethyl porphyrin blends. *ChemPhysChem*, 10:2316–2326, 2009.

[138] P.E. Keivanidis, F. Laquai, J.W.F. Robertson, S. Baluschev, J. Jacob, K. Mullen, and G. Wegner. Electron-exchange-assisted photon energy up-conversion in thin films of π-conjugated polymeric composites. *Journal of Physical Chemistry Letters*, 2:1893–1899, 2011.

[139] W. Staroske, M. Pfeiffer, K. Leo, and M. Hoffmann. Single-step triplet-triplet annihilation: An intrinsic limit for the high brightness efficiency of phosphorescent organic light emitting diodes. *Phys. Rev. Lett.*, 98(19):197402, May 2007.

[140] S. Forrest P. Peumans, S. Uchida. Efficient bulk heterojunction photovoltaic cells using small-molecular-weight organic thin films. *Nature*, 425:158–162, 2003.

[141] M. A. Baldo, C. Adachi, and S. R. Forrest. Transient analysis of organic electrophosphorescence. ii. transient analysis of triplet-triplet annihilation. *Phys. Rev. B*, 62(16):10967–10977, Oct 2000.

[142] C. Adachi, M.A. Baldo, S.R. Forrest, S. Lamansky, M.E. Thompson, and R.C. Kwong. High-efficiency red electrophosphorescent devices. *Journal of the American Chemical Society*, 78(11):1622–1624, 2001.

[143] Martin Gouterman, Frederick P. Schwarz, Paul D. Smith, and D. Dolphin. Porphyrins. xxvii. spin-orbit coupling and luminescence of group iv complexes. *The Journal of Chemical Physics*, 59(2):676–690, 1973.

[144] Mitio Inokuti and Fumio Hirayama. Influence of energy transfer by the exchange mechanism on donor luminescence. *The Journal of Physical Chemistry A*, 43(6):1978–1989, 1965.

[145] E. Engel, K. Leo, and M. Hoffmann. Ultrafast relaxation and exciton-exciton annihilation in ptcda thin films at high excitation densities. *Chemical Physics*, 325(1):170 – 177, 2006. Electronic Processes in Organic Solids.

[146] W.S. Chow. Towards artificial photosynthesis. *Photosynthesis: Plastid Biology,*

Energy Conversion, and Carbon Assimilation, Advances in Photosynthesis and Respiration, 34:607–622, 2012.

[147] D. P. Arnold and J. Blok. The coordination chemistry of tin porphyrin complexes. *Coordination Chemistry Reviews*, 248:299–319, 2004.

[148] S. Fukuzumi, T. Hasobe, K. Ohkubo, M.J. Crossley, P.V. Kamat, and H. Imahori. pi-complex formation in electron-transfer reactions of porphyrins. *Society of Porphyrins and Phthalocyanines*, 8:191–200, 2004.

[149] D. Gust, T.A. Moore, and A.L. Moore. Molecular mimicry of photosynthetic energy and electron transfer. *Accounts of Chemical Research*, 26:198–205, 1993.

[150] C. Bucher, C.H. Devillers, J.C. Moutet, G. Royal, and E. Saint-Aman. Ferrocene appended porphyrins: Synthesis and properties. *Chemistry Reviews*, 253:21–36, 2009.

[151] A.J. Bard. Electron transfer branches out. *Nature*, 374, 1995.

[152] Z. Liu, A.A. Yasseri, J.S. Lindsey, and D.F. Bocian. Molecular memories that survive silicon device processing and real-world operation. *Science*, 302:1543–1545, 2003.

[153] H.J. Kim, N. Bampos, and J.K.M Sanders. Assembly of dynaimc heterometallic oligoporphyrins using cooperative zinc-nitrogen, ruthenium-nitrogen, and tin-oxygen coordination. *Journal of the American Chemical Society*, 121:8120–8121,

1999.

[154] M.R. Wasielewski. Photoinduced electron transfer in supramolecular systems for artificial photosynthesis. *Chemical Reviews*, 92, 1992.

[155] T. Honda, T. Nakanishi, K. Ohkubo, T. Kojima, and S. Fukuzumi. Formation of a long-lived photoinduced electron transfer state in an electron acceptor-donor-acceptor porphyrin triad connected by coordination bonds. *Journal of Physical Chemistry C*, 114:14290–24299, 2010.

[156] M. Maiti, B.R. Danger, and R.P. Steer. Photophysics of soret-excited tetrapyrroles in solution. iv. radiationless decay and triplet-triplet annihilation investigated using tetraphenylporphinato sn(iv). *Journal of Physical Chemistry A*, 113:11318–11326, 2009.

[157] A. Yokoyama, T. Kojima, K. Ohkubo, M. Shiro, and S. Fukuzumi. Formation of a hybrid compound composed of a saddle-distorted tin(iv)-porphyrin and a keggin-type heteropolyoxometalate to undergo intramolecular photoinduced electron transfer. *Journal of Physical Chemistry A*, 115:986–997, 2011.

[158] P. Solntsev, J.R. Sabin, S.J. Dammer, N.N. Gerasimchuk, and V.N. Nemykin. Unexpected fluorescence properties in an axially sigma-bonded ferrocenyl-containing porphyrin. *Chemical Communications*, 46:6581–6583, 2010.

[159] A. Tabard, R. Guilard, and K.M. Kadish. Synthesis, characterization, and electrochemistry of indium(ii1) porphyrins that contain a stable indium-carbon σ bond. *Inorganic Chemistry*, 25(23):4277–4285, 1986.

[160] Y. Liu, Y. CHen, L. Cai, J. Wang, Y. Lin, J.J. Doyle, and W.J. Blau. Optical limiting properties of axially substituted indium phthalocyanines in the solid pmma composite films. *Materials Chemistry and Physics*, 107:189–192, 2008.

[161] M. Yuksek, A. Elmali, M. Durmus, H.G. Yaglioglu, H. Unver, and T. Nyokong. Good optical limiting performance of indium and gallium phthalocyanines in a solution and co-polymer host. *Journal of Optics*, 12(015208):1–9, 2010.

[162] D. Dini, M.J.F. Calvete, M. Hanack, and M. Meneghetti. Indium phthalocyanines with different axial ligands: A study of the influence of the structure on the photophysics and optical limiting properties. *Journal of Physical Chemistry A*, 112:8515–8522, 2008.

[163] M. Durmus and T. Nyokong. Synthesis, photophysical and photochemical properties of tetraand octa-substituted gallium and indium phthalocyanines. *Polyhedron*, 26:3323–3335, 2007.

[164] S. Mammen, C.S. Menon, and N.V. Unnikrishnan. Electrical and optical studies on thin films of indium phthalocyanine chloride. *Materials Science-Poland*, 23(3):707–713, 2005.

[165] M.J. Crossley, P. Thordarson, and R.A.S. Wu. Efficient formation of lipophilic dihydroxotin(iv) porphyrins and bis-porphyrins. *Journal of Chemical Society*, Perkin Trans.(1):2294–2302, 2001.

[166] H.J. Kim, W.S. Jeon, J.H. Lim, C.S. Hong, and H.J. Kim. Synthesis, x-ray crystal structure, and electrochemistry of trans-bis(ferrocenecarboxylato)(tetraphenylporphyrinato)tin(iv). *Polyhedron*, 26:2517–2522, 2007.

[167] D. Magde, M.W. Windsor, D. Holten, and M. Gouterman. Picosecond flash photolysis: Transient absorption in sn(iv), pd(ii), and cu(ii) porphryins. *Chemical Physics Letters*, 29(2):183–185, 1974.

[168] D. Maeda, H. Shimakoshi, M. Abe, M. Fujitsuka, T. Majima, and Y. Hisaeda. Synthesis of a novel sn(iv) porphycene-ferrocene triad linked by axial coordination and solvent polarity effect in photoinduced charge separation process. *Inorganic Chemistry*, 49:2872–2880, 2012.

[169] T. Lazarades, S. Kuhri, G. Charalambidis, M.K. Panda, D.M. Guldi, and A.G. Coutsolelos. Electron vs. energy transfer in arrays featuring two bodipy chromophores axially bound to a sn(iv) porphyrin via a phenolate or benzoate bridge. *Inorganic Chemistry*, 51:4193–4204, 2012.

[170] E.J. Land, A.F. McDonagh, D.J. McGarvey, and T.G. Truscott. Photophysical studies of tin(iv)-protoporphyrin: Potential phototoxicity of a chemotherapeutic

agent proposed for the prevention of neonatal jaundice. *Procedings of the National Chemical Society*, 85:5249–5253, 1988.

[171] P.P. Kiran, D.R. Reddy, B.G. Maiya, A.K. Dharmadhikari, G.R. Kumar, and D.N. Rao. Nonlinear absorption properties of axial-bonding type tin(iv) tetratolylporphyrin based hybrid porphyrin arrays. *Optics Communications*, 252:150–161, 2005.

[172] R.F. Kubin and A.N. Fletcher. Fluorescence quantum yields of some rhodamine dyes. *Journal of Luminescence*, 27:455–462, 1982.

[173] Jarrres B. Callis, Martin Gouterman, Y.M. Jones, and B.H. Henderson. Porphyrins. xxii fast fluorescence, delayed fluorescence, and quasiline structure in palladium and platinum complexes. *The Journal of Molecular Spectroscopy*, 39:410–420, 1971.

[174] J. Mezyk, J. Kalinowski, F. Meinardi, and R. Tubino. Triplet exciton interactions in solid films of an electrophosphorescent pt (ii) porphyrin. *Applied Physics Letters*, 86(11):111916, 2005.

Appendix A

Appendix

A.1 NiTMP NMR data

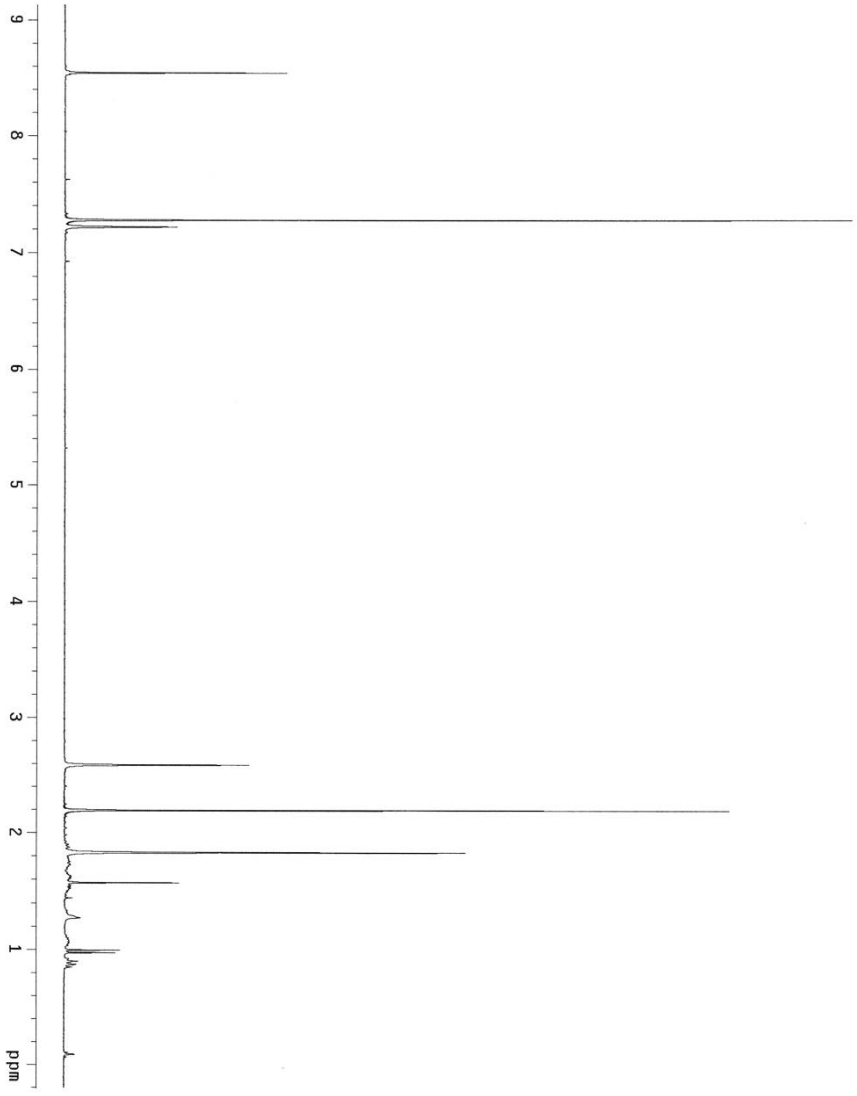

Figure A.1: NMR data of the synthesized NiTMP

A.2 NiOEP Weight Parameters Plots

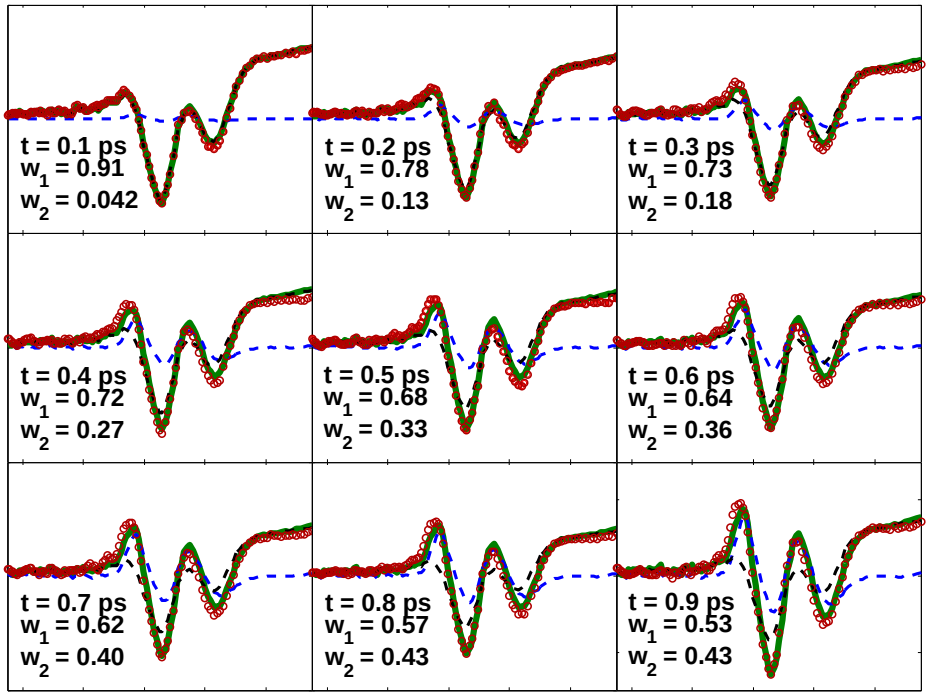

Figure A.2: NiOEP weight parameters plots for early pump probe time delays.

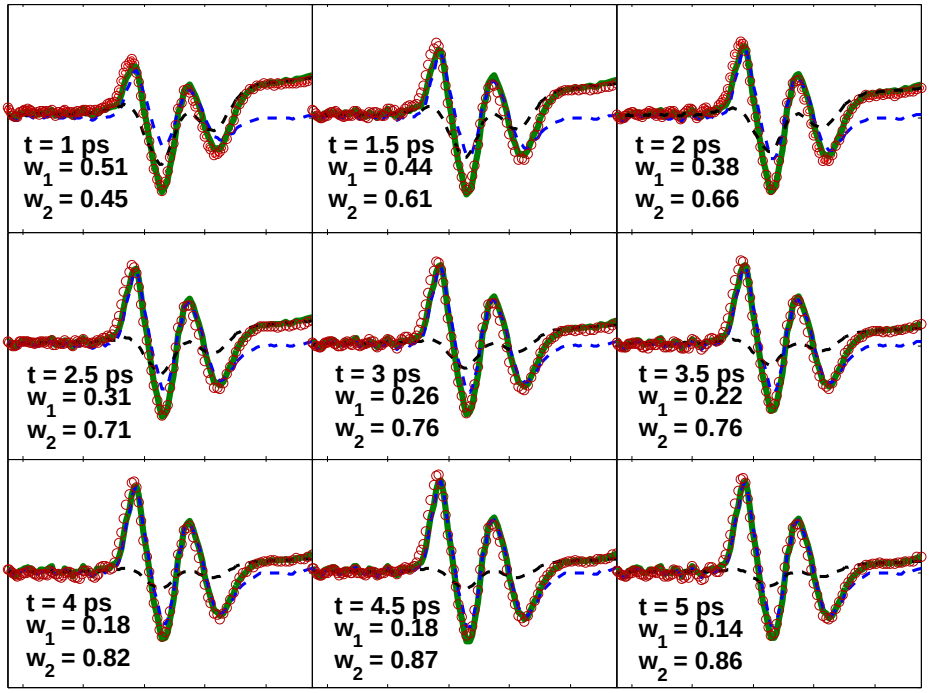

Figure A.3: NiOEP weight parameters plots for middle pump probe time delays.

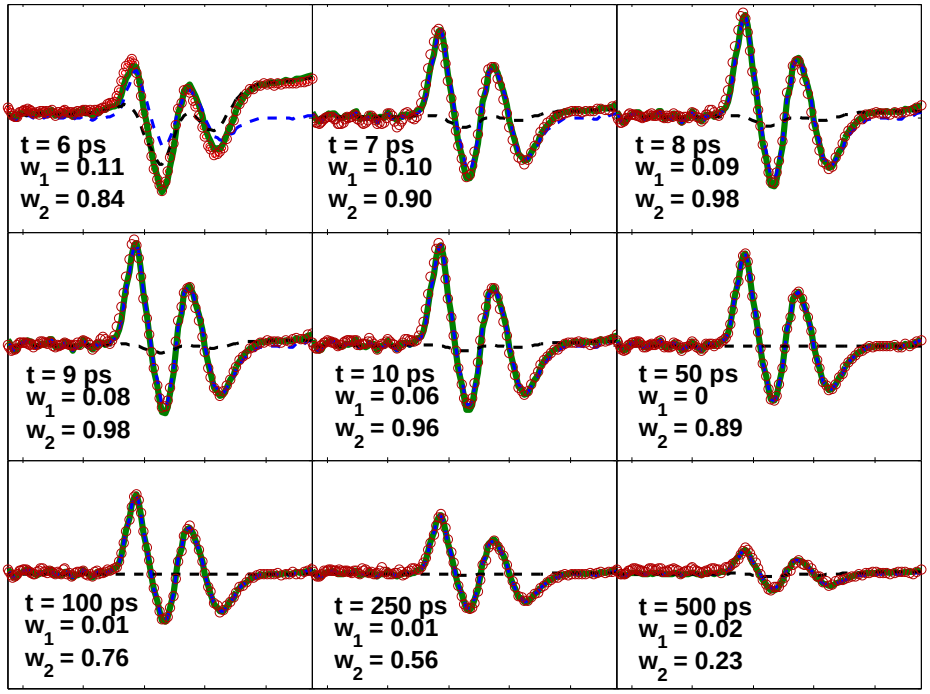

Figure A.4: NiOEP weight parameters plots for late pump probe time delays.

A.3 Second Order Kinetics of Triplet Fusion

Time and power dependent fits were done as a collaboration between Tom Pundsack and Jon Hinke.

The T_1 triplet fusion process was previously determined to populate the $d_{(x^2-y^2)}$ orbital, shown as D^*, with no intermediate states.

$$T_1 + T_1 \xrightarrow{k_{TTF}} D^* + S_0 \tag{A.1}$$

If we consider the long triplet lifetime of PtOEP,[110;173] the unimolecular decay of T_1 is negligible. It should also be noted that S_0 does not contribute to the ΔO.D. spectra. The loss of T_1 on our timescale only occurs through triplet fusion with a time independent rate k_{TTF}.

$$-\frac{1}{2}\frac{\partial[T_1]}{dt} = \frac{\partial[D^*]}{dt} = k_{TTF}[T_1]^2 \tag{A.2}$$

The differential equation can be solved with the assumptions that $[T_1]_0$ is the exciton concentration determined experimentally and $[D^*]_0 = 0$.

$$[D^*] = \frac{[T_1]_0^2 k_{TTF} k}{1 + 2[T_1]_0 k_{TTF} k} \tag{A.3}$$

$$[T_1] = -\frac{[T_1]_0}{1 + 2[T_1]_0 k_{TTF} k} \tag{A.4}$$

$[D^*]$ and $[T_1]$ both contribute to the overall ΔO.D. at each energy, E, in eV.

$$\Delta O.D._E = \alpha_{T_1,E}[T_1] + \alpha_{D^*,E}[D^*] \tag{A.5}$$

α was treated as a weight parameter for each individual species and its respective contribution to the ΔO.D. spectra at energy, E. The contribution of $\alpha_{D^*,E=2.58} \sim 0$, given the ΔO.D. spectra of D^* in Figure A.5.

Figure A.6 shows the ΔO.D. as a function of laser fluence at 10 ps. A global fit of all three traces yields a $k_{TTF} = (5.4 \pm 0.4)$ x 10^{-10} cm^3 s^{-1} and other fit parameters in Table A.3. Accuracy of the fit supports the idea of a bimolecular process consistent with the triplet fusion mechanism. The k_{TTF} reported here is two orders of magnitude larger than the time-integrated value (8 ± 3) x 10^{-12}.[174] The disparity in the rate coefficients may be due to the time-dependence when not transport limited. Our measurement at 10 ps could be considered an initial value for a time-dependent rate coefficient.

Parameter	Weight
$\alpha_{T_1,E=2.21eV}$	-(8.9 ± 0.3) x 10^{-21}
$\alpha_{D^*,E=2.21eV}$	(2.9 ± 0.2) x 10^{-20}
$\alpha_{T_1,E=2.27eV}$	-(5.2 ± 0.2) x 10^{-21}
$\alpha_{D^*,E=2.27eV}$	-(7.2 ± 0.4) x 10^{-21}
$\alpha_{T_1,E=2.58eV}$	(9.3 ± 0.3) x 10^{-21}

Table A.1: Fitting parameters, α, for the power dependent traces in Figure A.6 at the 95% confidence interval

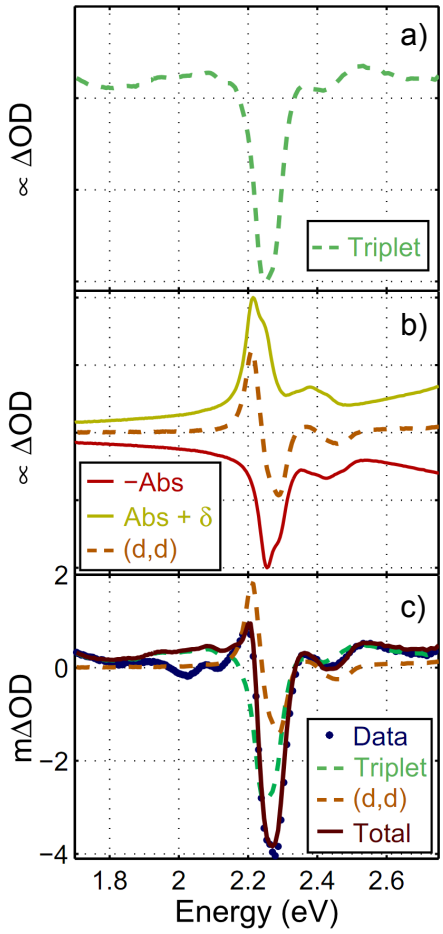

Figure A.5: Δ O.D. spectral components of a) T_1 and b) D* along with c) a fit of a 500 ps full frequency trace comprised of weighted T_1 and D* spectra.

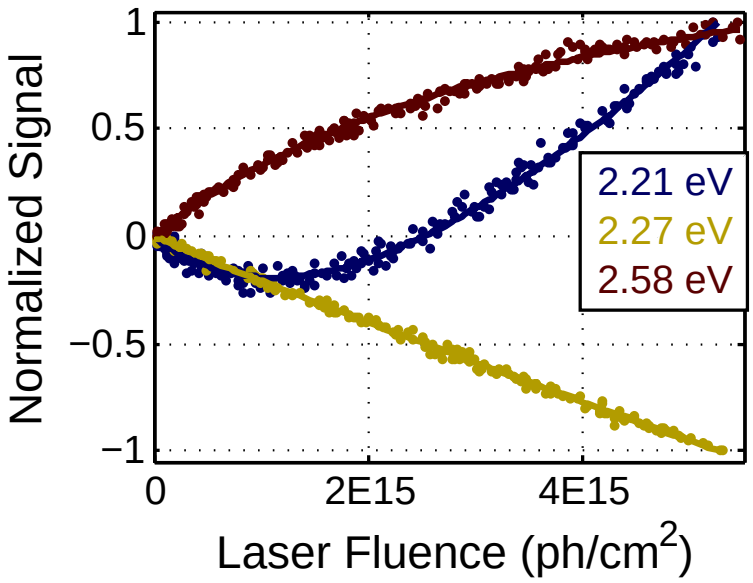

Figure A.6: Second order kinetic fits of the 2.58, 2.27, and 2.21 eV traces as a function of power at a 10 ps delay.

A.4 Second Order Kinetics Derivation

This derivation was performed by Tom Pundsack.

Consider the simplest case in which a 3-level system describes the annihilation process of two excited states in which two excitons annihilate to form a ground state (A) and a more energetic excited state (C).

$$2B^* \rightarrow A + C^* \tag{A.6}$$

In this case, loss of our initial excited states, B, is described as:

$$-\frac{\partial[B]}{\partial t} = k_1[B] + k_2[B]^2 \tag{A.7}$$

where $k_1[B]$ is the loss due to the intrinsic lifetime of the excited state and $k_2[B]^2$ is loss due to annihilation. However, if the rate of annihilation is much faster than the recombination rate (k_2 ¿¿ k_1), loss of the excited state under our experimental conditions becomes:

$$-\frac{\partial[B]}{\partial t} = k_2[B]^2 \tag{A.8}$$

Considering the stoichiometry of the reaction, it becomes:

$$-\frac{1}{2}\frac{\partial[B]}{\partial t} = k_{an}[B]^2 \tag{A.9}$$

$$\frac{\partial[B]}{\partial t} = -2k_{an}[B]^2 \tag{A.10}$$

By integrating the equation, we can solve for $[B]$:

$$-\frac{1}{[B]} = \frac{1}{[B]_0} + 2k_{an}[B]^2 \tag{A.11}$$

Solving for $[B]$ we find

$$[B] = \frac{[B]_0}{1 + 2k_{an}[B]} \tag{A.12}$$

We can relate the $[B]_0$ to the irradiance I_0 through Beers Law,

$$I = I_0 e^{\sigma nl} \rightarrow I_0 - I = I_0(1 - e^{\sigma nl}) \tag{A.13}$$

where I_0 is $\frac{power}{area}$, $\frac{N \cdot h\nu}{s \cdot cm^2}$, and N is the number of photons. We want $[B]_0$ per pulse,

$$N_0 - N\left(\frac{h\nu}{r \cdot s \cdot cm^2}\right) = \frac{N_0 \cdot h\nu}{r \cdot s \cdot cm^2}(1 - e^{\sigma nl}) \tag{A.14}$$

where r is the rep rate of the laser. We divide by the path length, l,

$$\frac{N_0 - N}{cm^3}\left(\frac{h\nu}{r \cdot s}\right) = \left(\frac{1}{l}\right)\frac{N_0 \cdot h\nu}{r \cdot s \cdot cm^2}(1 - e^{\sigma nl}) \tag{A.15}$$

reorganize the equation,

$$\frac{N_0 - N}{cm^3}\left(\frac{h\nu}{r \cdot s}\right) = \left(\frac{1}{r \cdot s \cdot l}\right)\frac{N_0 \cdot h\nu}{cm^2}(1 - e^{\sigma nl}) \tag{A.16}$$

where we can describe $\frac{N_0 \cdot h\nu}{cm^2}$ as our laser fluence, F_0 in $\frac{Joules}{pulse \cdot cm^2}$. The result is:

$$\frac{N_0 - N}{cm^3} = F_0 \left(\frac{1 - e^{\sigma nl}}{h\nu \cdot l} \right) = \frac{ExcitedStates}{cm^3} \tag{A.17}$$

We can describe the concentration of excitons as a function of the laser fluence,

$$[B]_0 = \alpha F_0 \tag{A.18}$$

where $\alpha = \frac{1-e^{\sigma nl}}{h\nu \cdot l}$, resulting in:

$$[B] = \frac{[B]_0}{1 + 2k_{an} t [B]_0} \tag{A.19}$$

$$[B] = \frac{\alpha F_0}{1 + 2k_{an} t \alpha F_0} \tag{A.20}$$

where $\alpha = \frac{1-e^{\sigma nl}}{h\nu \cdot l}$

If we consider the same process

$$2B^* \rightarrow A + C^* \tag{A.21}$$

but consider $[C]$, we find

$$\frac{\partial [C]}{\partial t} = k_{an} [B]^2 \tag{A.22}$$

$$\frac{\partial [C]}{\partial t} = (\frac{\alpha F_0}{1 + 2k_{an} t \alpha F_0})^2 \tag{A.23}$$

If we assume $[C]_0 = 0$, we solve the differential equation, resulting in

$$[C] = \left(\frac{\alpha F_0}{2}\right)(1 - \frac{1}{2\alpha F_0 k_{an} t + 1}) \tag{A.24}$$

where $\alpha = (\frac{1-e^{-\sigma n l}}{h\nu \cdot l})$.

Let us consider $[A]$, which includes 2 terms: Initial ground state hole and recovery due to annihilation. If $[A]_0$ = -$[B]_0$, then $[A]_0$ = -αF_0 under the same annihilation process.

$$\frac{\partial [A]}{\partial t} = k_{an}[B]^2 \tag{A.25}$$

Solving for $[A]$ as we did with $[C]$,

$$[A] = \left(\frac{\alpha F_0}{2}\right)(1 - \frac{1}{2\alpha F_0 k_{an} t + 1}) - \alpha F_0 \tag{A.26}$$

A.5 PtOEP Triplet Fusion Förster and Dexter Equation Derivation

This derivation was done by Tom Pundsack following steps outlined previously.[144]

We can describe the statistical average of finding a donor in an excited state, ϕ, as:

$$\phi(t) = e^{\frac{-t}{\tau}} \frac{lim}{N, V \to \infty} \left(\frac{4\pi}{V} \int_0^{R_V} e^{-tn(R)R^2} dR\right)^N \tag{A.27}$$

where *n(R)* is the rate constant from donor to acceptor as a function of distance, R, and N is the total number of traps or acceptors in a cylinder with volume $V = 4\pi R_V^3/3$ and

excited state concentration C = N/V. In this case, N represents the number of excited states since the excited states represent the acceptors in this fusion process. For Dexter energy transfer, the rate constant can be described as:

$$n(R) = K \exp \frac{-2R}{L} \tag{A.28}$$

The probability of finding the excited state with Dexter transfer is then defined as:

$$\phi(t) = e^{\frac{-t}{\tau}} \frac{lim}{N, V \to \infty} \left(\frac{4\pi}{V} \int_0^{R_V} e^{-tn(R)R^2} dR \right)^N \tag{A.29}$$

Integration has already been done in the literature[144] and results in:

$$\phi(t) = e^{\frac{-t}{\tau}} \frac{lim}{N, V \to \infty} \left(1 - \frac{L^3}{8R_V^3} g(k,t) \right)^N \tag{A.30}$$

where:

$$g(k,t) = -x \int_0^{R_V} ln(y)^3 dy \tag{A.31}$$

Taking the limit of:

$$\frac{lim}{N, V \to \infty} N ln \left(1 - \frac{L^3}{8R_V^3} \frac{N}{N} g(k,t) \right) \tag{A.32}$$

$$= \frac{lim}{N, V \to \infty} N ln \left(1 - \frac{L^3}{8} \frac{4\pi c}{3} \frac{1}{N} g(k,t) \right) \tag{A.33}$$

$$= \frac{lim}{N, V \to \infty} N ln \left(1 - \frac{\pi L^3 c}{6N} g(k,t)\right) \tag{A.34}$$

$$= \frac{lim}{N, V \to \infty} \frac{ln(1 - \sigma/N)}{1/N} \tag{A.35}$$

where:

$$\sigma = \frac{\pi L^3 c}{6} g(k,t) \tag{A.36}$$

and c is the trap concentration. Thus:

$$\phi(t) = e^{\frac{-t}{\tau}} e^{-\sigma g(k,t)} \tag{A.37}$$

The number of donors in the excited state, n, at any time, t, can be described as:

$$n = \phi(t) n_0 \tag{A.38}$$

$$\dot{n} = \dot{\phi(t)} n_0 \tag{A.39}$$

where:

$$\dot{\phi(t)} = e^{\frac{-t}{\tau} - \sigma g(k,t)} \frac{d}{dt} \left(\frac{-t}{\tau} - \sigma g(k,t)\right) \tag{A.40}$$

$$= \phi(t) \left(\frac{-t}{\tau} - \sigma h(k,t)\right) \tag{A.41}$$

where:

$$h(k,t) = \frac{d}{dt}g(k,t) \tag{A.42}$$

So:

$$\dot{n} = n_0\phi(t)\left(\frac{-1}{\tau} - \frac{\pi L^3 c}{6}h(k,t)\right) \tag{A.43}$$

$$\phi(t) = \frac{n}{n_0} \tag{A.44}$$

$$\dot{n} = \left(\frac{-n}{\tau} - \frac{\pi L^3}{6}h(k,t)n^2\right) \tag{A.45}$$

$c = n$ since the "traps" are the excited states. If we assume τ is large relative to annihilation (PtOEP lifetime ≈ 100 μs), $\acute{}n$ reduces to:

$$\dot{n} = -\frac{\pi L^3}{6}h(k,t)n^2 \tag{A.46}$$

Solving for dE:

$$\int_{n_0}^{n} = -\frac{\pi L^3}{6}\int_0^t h(k,t)dt' \tag{A.47}$$

$$\frac{1}{n_0} - \frac{1}{n} = -\frac{\pi L^3}{6}(g(kt) - g(0)) \tag{A.48}$$

$g(0) = 0$, so we can describe the number of excited states, n, as:

$$n = \frac{n_0}{1 + \frac{n_0 \pi L^3}{6} g(kt)} \tag{A.49}$$

The fusion event is shown as:

$$T* + T* \rightarrow G + D* \tag{A.50}$$

where T is the triplet excited state, G is the ground electronic state, and D is the high energy excited state localized on the $d_{x^2-y^2}$ orbital following triplet fusion. The contribution of each state to the pump probe spectra is dependent on the initial concentration of excited states, n. The excited states rapidly intersystem cross to the triplet state and contribute to the initial triplet absorption spectra such that $n_0 = T_0$.

$$T = \frac{T_0}{1 + \frac{T_0 \pi L^3}{6} g(kt)} \tag{A.51}$$

$$G = -\frac{T_0 + \frac{T_0^2 \pi L^3}{12} g(kt)}{1 + \frac{T_0 \pi L^3}{6} g(kt)} \tag{A.52}$$

$$D = \frac{\frac{T_0^2 \pi L^3}{12} g(kt)}{1 + \frac{T_0 \pi L^3}{6} g(kt)} \tag{A.53}$$

A.6 SnTPP TDDFT Calculations

Calculations were performed by Pavlo Solntsev and Victor Nemykin at the University of Minnesota-Duluth.

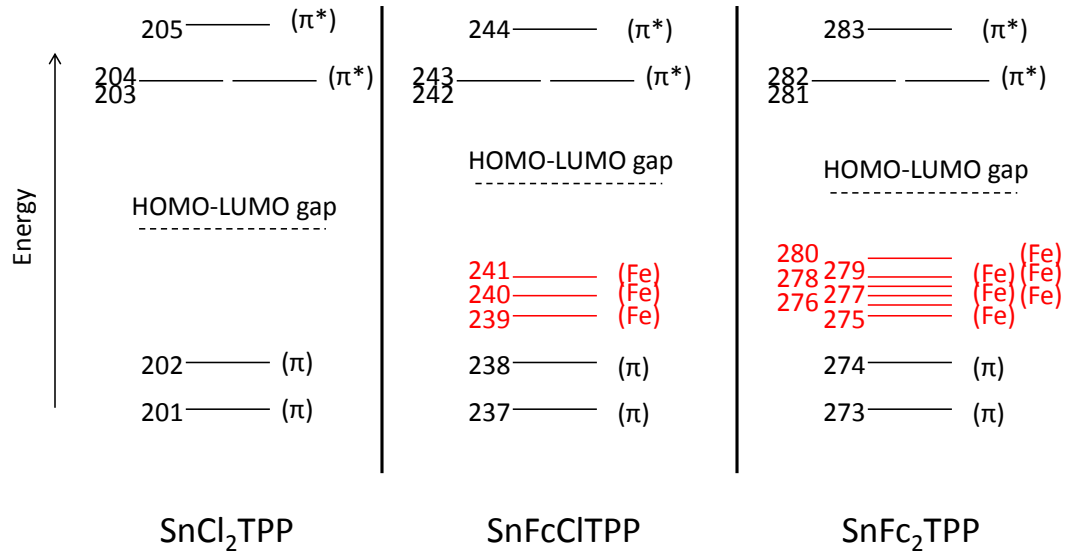

Figure A.7: Molecular orbital labels and positioning for $SnCl_2TPP$, SnFcClTPP, and $SnFc_2TPP$

MO	Energy (eV)	Sym.	Sn	Cl	Porphyrin	Phenyl
189	-6.339	A1	0.01	0.06	3.8	96.12
190	-6.305	E	0.2	3.49	6.12	90.2
191	-6.305	E	0.2	3.49	6.12	90.2
192	-6.268	B1	0	0	15.23	84.76
193	-6.192	E	0.04	0.84	23.8	75.31
194	-6.192	E	0.04	0.84	23.8	75.31
195	-6.175	A2	1.73	14.91	66.88	16.47
196	-6.157	B2	0	0	75.95	24.04
197	-5.886	E	2.99	89.42	7.55	0.04
198	-5.886	E	2.99	89.42	7.55	0.04
199	-5.683	E	0.28	72.03	27.41	0.29
200	-5.683	E	0.28	72.03	27.41	0.29
201	-5.348	A1	0	0	94.38	5.61
202	-4.935	A2	0.12	5.49	75.33	19.07
HOMO	LUMO	gap	—	1.704	eV	————
203	-3.231	E	0.19	0.63	87.29	11.89
204	-3.231	E	0.19	0.63	87.29	11.89
205	-1.938	B1	0	0	86.66	13.33
206	-1.247	B1	0.02	0	20.95	79.03
207	-1.227	E	0.04	0.01	14.47	85.48
208	-1.227	E	0.04	0.01	14.47	85.48
209	-1.17	A2	0.29	0.2	10.89	88.63
210	-1.15	B2	0	0	5.39	94.61
211	-1.141	A1	0.03	0.02	4.4	95.55
212	-1.122	E	0.41	0.04	5.03	94.52
213	-1.122	E	0.41	0.04	5.03	94.52
214	-0.664	A1	47.25	14.22	38.15	0.39
215	-0.251	B2	0	0	94.89	5.11
216	0.329	E	1.2	0.48	95.87	2.44
217	0.329	E	1.2	0.48	95.87	2.44
218	0.799	A1	0.04	0.02	92.5	7.44
219	1.163	A2	42.34	22.7	28.96	6
220	1.578	E	3.76	0.12	9.29	86.82
221	1.578	E	3.76	0.12	9.29	86.82
222	1.603	A1	0.14	0.07	7.97	91.83
223	1.681	B2	0	0	1.96	98.03
224	1.728	B1	0	0	61.39	38.61
225	1.969	E	0.69	0.09	63.06	36.15
226	1.969	E	0.69	0.09	63.06	36.15
227	2.033	E	21.01	1.57	67.82	9.6
228	2.033	E	21.01	1.57	67.82	9.6

Table A.2: TDDFT calculations of $SnCl_2TPP$ molecular orbitals (MO) with energies near the HOMO-LUMO bandgap and the contributions from tin (Sn), chlorine (Cl), porphyrin, and phenyl groups.

Order	Symm	f	Energy (eV)	λ (nm)	ν (cm^{-1})	Transition	Coef
11	Singlet-E	0.5282	2.837	437.03	22881.7		
=	=	=	=	=	=	187→203	0.21423
=	=	=	=	=	=	187→204	-0.17057
=	=	=	=	=	=	189→203	-0.10844
=	=	=	=	=	=	189→204	-0.1362
=	=	=	=	=	=	195→203	0.16565
=	=	=	=	=	=	195→204	-0.13188
=	=	=	=	=	=	201→203	0.27866
=	=	=	=	=	=	201→204	0.35001
=	=	=	=	=	=	202→203	-0.17493
=	=	=	=	=	=	202→204	0.1393
12	Singlet-E	0.5282	2.837	437.03	22881.7		
=	=	=	=	=	=	187→203	0.17057
=	=	=	=	=	=	187→204	0.21423
=	=	=	=	=	=	189→203	0.1362
=	=	=	=	=	=	189→204	-0.10844
=	=	=	=	=	=	195→203	0.13188
=	=	=	=	=	=	195→204	0.16565
=	=	=	=	=	=	201→203	-0.35001
=	=	=	=	=	=	201→204	0.27866
=	=	=	=	=	=	202→203	-0.1393
=	=	=	=	=	=	202→204	-0.17493
34	Singlet-E	0.5233	3.3818	366.62	27276.2		
=	=	=	=	=	=	187→203	0.39888
=	=	=	=	=	=	187→204	0.3226
=	=	=	=	=	=	189→203	0.1017
=	=	=	=	=	=	189→204	-0.12572
=	=	=	=	=	=	195→203	0.14047
=	=	=	=	=	=	195→204	0.11363
=	=	=	=	=	=	199→205	0.11783
=	=	=	=	=	=	201→203	0.13359
=	=	=	=	=	=	201→204	-0.16514
=	=	=	=	=	=	202→203	0.10437
35	Singlet-E	0.5233	3.3818	366.62	27276.2		
=	=	=	=	=	=	187→203	0.3226
=	=	=	=	=	=	187→204	-0.39888
=	=	=	=	=	=	189→203	-0.12572
=	=	=	=	=	=	189→204	-0.1017
=	=	=	=	=	=	195→203	0.11363
=	=	=	=	=	=	195→204	-0.14047
=	=	=	=	=	=	200→205	-0.11783
=	=	=	=	=	=	201→203	-0.16514
=	=	=	=	=	=	201→204	-0.13359
=	=	=	=	=	=	202→204	-0.10437

Table A.3: TDDFT calculations of $SnCl_2TPP$ excited states. The doubly degenerate Q band is transitions 1 and 2 while the doubly degenerate B band is transitions 34 and 35.

MO	Energy(eV)	Sym.	Sn	Fe	Cl	CP	Porphyrin
230	-6.042	A’	0.48	0.78	2.12	2.35	94.26
231	-5.967	A’	5.84	0.42	23.71	4.05	65.98
232	-5.767	A’	11.54	6.29	13.43	52	16.75
233	-5.61	A”	0.17	5.3	0.08	92.68	1.76
234	-5.519	A’	5.15	6.16	9.22	70.83	8.63
235	-5.328	A”	2.9	0.18	81.08	0.8	15.04
236	-5.3	A’	2.48	0.91	77.23	3.01	16.37
237	-5.25	A”	0.02	0.05	0.01	0.65	99.27
238	-4.767	A’	0.55	1.06	3.6	3.38	91.41
239	-3.943	A’	3.16	78.48	0.02	15.48	2.87
240	-3.798	A”	0.14	58.86	0	40.38	0.62
241	-3.742	A’	0.45	59.71	0.01	38.76	1.07
HOMO	LUMO	gap	—	0.606	eV	———————-	
242	-3.136	A”	0.19	0.07	0.45	0.44	98.85
243	-3.133	A’	0.2	0.26	0.49	0.34	98.72
244	-1.879	A”	0.01	0.02	0	0.18	99.79
245	-1.213	A’	0.11	0.28	0.01	0.37	99.22
246	-1.158	A’	0.26	0.59	0.11	0.41	98.62
247	-1.157	A”	0.04	0.08	0	0.17	99.7
248	-1.142	A”	0.02	0.27	0	0.63	99.07
249	-1.113	A’	0.56	0.84	0.01	1.19	97.4
250	-1.113	A”	0.43	0.06	0.02	0.54	98.95
251	-1.077	A’	0.52	1.4	0.04	0.25	97.79
252	-1.073	A”	0.15	0.02	0	0.15	99.67
253	-0.949	A’	4.8	41.94	0.16	47.07	6.03
254	-0.849	A”	0.7	43.43	0.02	53.46	2.39
255	-0.147	A’	2.97	26.84	0.64	3.65	65.91
256	-0.07	A’	3.51	76.55	0.82	5.59	13.54
257	0.088	A’	34.53	24.65	6.13	7.52	27.17
258	0.4	A”	1.76	0.12	0.15	1.8	96.17
259	0.419	A’	5	2.04	0.92	4.41	87.63
260	0.869	A”	0.01	0.03	0	0.39	99.57
261	1.17	A’	12.68	2.87	0.66	58.11	25.68
262	1.271	A”	7.41	3.98	0.21	64.94	23.46
263	1.322	A”	2.04	12.03	0.04	35.02	50.88
264	1.329	A’	12.45	29.29	0.51	46.14	11.61
265	1.416	A”	0.82	14.75	0.02	44.89	39.53
266	1.52	A’	3.84	17.17	0.37	11.64	66.98
267	1.572	A’	8.42	10.49	0.9	4.91	75.27
268	1.685	A”	0.97	0.64	0	0.94	97.45

Table A.4: TDDFT calculations of SnFcClTPP molecular orbitals (MO) with energies near the HOMO-LUMO bandgap and the contributions from tin (Sn), iron (Fe), chlorine (Cl), cyclopentane (CP), and porphyrin.

Order	Symm	f	Energy (eV)	λ (nm)	ν (cm^{-1})	Transition	Coef
9	Singlet-A"	0.0599	1.9463	637.03	15697.8		
=	=	=	=	=	=	237→243	-0.33898
=	=	=	=	=	=	238→242	0.5656
10	Singlet-A'	0.0548	1.9521	635.13	15744.8		
=	=	=	=	=	=	237→242	0.33698
=	=	=	=	=	=	238→243	0.55405
=	=	=	=	=	=	240→244	-0.14265
39	Singlet-A'	0.2906	2.7573	449.67	22238.5		
=	=	=	=	=	=	218→243	-0.1271
=	=	=	=	=	=	222→242	0.1034
=	=	=	=	=	=	231→243	0.40019
=	=	=	=	=	=	232→243	0.11687
=	=	=	=	=	=	237→242	0.4199
=	=	=	=	=	=	238→243	-0.17779
40	Singlet-A"	0.2798	2.759	449.38	22252.9		
=	=	=	=	=	=	218→242	0.12023
=	=	=	=	=	=	231→242	-0.41962
=	=	=	=	=	=	237→243	0.41887
=	=	=	=	=	=	238→242	0.17417

Table A.5: TDDFT calculations of SnFcClTPP excited states. Transitions 39 and 40, corresponding to the B band, reveal only (π,π*) excitations. Q band transitions in 9 and 10 show some MLCT contribution from orbital 240 on the ferrocene ligand to π* orbital 244.

MO	Energy(eV)	Sym.	Sn	Fe	CP	Porphyrin	Phenyl
260	-6.118	Ag	1.02	4.41	12.51	25.59	56.48
261	-6.052	Au	1.43	5.72	14.62	67.6	10.63
262	-6.033	Ag	0.74	1.46	6.62	59.18	32
263	-6.015	Ag	2.3	9.5	34.24	43.32	10.63
264	-5.968	Au	2.18	7.51	19.84	63.01	7.46
265	-5.947	Au	0.17	22.34	69.84	6.82	0.82
266	-5.943	Ag	0.07	22.99	72.19	2.91	1.83
267	-5.719	Au	13.24	11.33	54.55	17.66	3.22
268	-5.433	Ag	0.12	5.46	91.79	2.16	0.48
269	-5.424	Au	0.29	5.71	91.94	1.49	0.57
270	-5.397	Ag	9.25	5.19	65.79	19.63	0.14
271	-5.318	Au	4.13	8.49	80.24	6.4	0.74
272	-5.235	Au	0.02	0.12	1.61	92.33	5.9
273	-5.121	Ag	13.09	5.09	60.6	20.98	0.25
274	-4.664	Au	1.54	3.17	8.89	69.07	17.34
275	-3.758	Au	3.25	78.69	15.81	1.93	0.32
276	-3.748	Ag	4.69	74.86	16	4.4	0.05
277	-3.631	Ag	0.09	58.29	40.56	0.9	0.17
278	-3.628	Au	0.27	59.07	40.22	0.36	0.07
279	-3.556	Au	0.31	60.8	38.04	0.76	0.09
280	-3.554	Ag	0.61	58.89	37.97	2.36	0.17
HOMO	LUMO	gap	—	0.435	eV	——————-	
281	-3.119	Ag	0.19	0.66	0.93	85.31	12.92
282	-3.117	Ag	0.17	0.57	0.85	85.39	13.02
283	-1.887	Au	0.02	0.05	0.39	84.37	15.17
284	-1.194	Ag	0.11	0.33	0.71	15.11	83.74
285	-1.148	Au	0.09	0.5	0.74	17.79	80.87
286	-1.134	Au	0.08	0.57	0.57	16.75	82.03
287	-1.128	Ag	0.01	0.31	0.57	9.5	89.61
288	-1.106	Au	0.59	0.8	1.39	5.15	92.07
289	-1.093	Au	0.46	1.05	1.13	4.85	92.51
290	-1.082	Ag	0.94	2.13	1.19	6.01	89.73
291	-1.071	Ag	0.13	0.4	1.01	7.97	90.49
292	-0.767	Ag	4.44	41.51	47.45	5.89	0.72
293	-0.754	Au	4.06	45.4	47.29	2.62	0.63
294	-0.665	Au	1.91	42.97	52.68	1.4	1.04
295	-0.661	Ag	0.07	43.11	53.93	1.79	1.11
296	-0.079	Au	0.48	4.55	2.51	86.06	6.39
297	-0.023	Ag	0.66	86.72	5.97	2.03	4.62
298	0.093	Au	0.63	91.97	5.07	0.93	1.4
299	0.409	Ag	1.23	0.44	3.47	91.58	3.28
300	0.428	Ag	1.42	3.59	3.62	87.26	4.11

Table A.6: TDDFT calculations of $SnFc_2TPP$ molecular orbitals (MO) with energies near the HOMO-LUMO bandgap and the contributions from tin (Sn), iron (Fe), cyclopentane (CP), porphyrin, and phenyl groups.

Order	Symm	f	Energy (eV)	λ (nm)	ν (cm^{-1})	Transition	Coef
17	Singlet-AU	0.0268	1.8549	668.41	14960.9		
=	=	=	=	=	=	272→281	0.1399
=	=	=	=	=	=	272→282	-0.15229
=	=	=	=	=	=	274→281	0.29973
=	=	=	=	=	=	274→282	0.27343
=	=	=	=	=	=	276→283	0.50534
18	Singlet-AU	0.031	1.8668	664.16	15056.6		
=	=	=	=	=	=	272→281	0.17653
=	=	=	=	=	=	272→282	-0.13484
=	=	=	=	=	=	274→281	0.24764
=	=	=	=	=	=	274→282	0.32741
=	=	=	=	=	=	276→283	-0.49015
83	Singlet-AU	0.211	2.8093	441.34	22658.3		
=	=	=	=	=	=	252→282	0.13877
=	=	=	=	=	=	261→282	0.22448
=	=	=	=	=	=	264→282	-0.35174
=	=	=	=	=	=	265→281	-0.14965
=	=	=	=	=	=	267→282	-0.24033
=	=	=	=	=	=	272→281	0.32055
=	=	=	=	=	=	274→282	-0.12457
84	Singlet-AU	0.2037	2.8106	441.13	22669.1		
=	=	=	=	=	=	252→281	-0.1385
=	=	=	=	=	=	261→281	-0.22553
=	=	=	=	=	=	264→281	0.37398
=	=	=	=	=	=	265→282	-0.15885
=	=	=	=	=	=	267→281	0.23371
=	=	=	=	=	=	272→282	0.31946
=	=	=	=	=	=	274→281	0.12358

Table A.7: TDDFT calculations of $SnFc_2TPP$ excited states. The B band transitions 83 and 84 show no MLCT contribution from the iron and are solely (π,π*). The Q bands at 17 and 18 show some MLCT character originating from state 276 in the ferrocene ligand to the LUMO+3.